Hybrid systems at finite temperatures

Dissertation
der Mathematisch-Naturwissenschaftlichen Fakultät
der Eberhard Karls Universität Tübingen
zur Erlangung des Grades eines
Doktors der Naturwissenschaften
(Dr. rer. nat.)

vorgelegt von
Johannes Märkle
aus Tübingen

Tübingen
2014

Tag der mündlichen Qualifikation:	16. 12. 2014
Dekan:	Prof. Dr. Wolfgang Rosenstiel
1. Berichterstatter	Prof. Dr. Thomas E. Judd
2. Berichterstatter	Prof. Dr. Claus Zimmermann
3. Berichterstatter	Prof. Dr. Reinhold Walser

Für meinen Sohn
Finn Willem Blazer

"There is a theory which states that if ever anyone discovers exactly what the Universe is for and why it is here, it will instantly disappear and be replaced by something even more bizarre and inexplicable. There is another theory which states that this has already happened"

Douglas Adams

Contents

Abstract

A growing number of hybrid experiments consisting of cold atoms combined with nano devices or single trapped ions, has created the need for a theoretical tool to describe these systems. Because heating or cooling of the cloud has been frequently observed in this context, finite temperatures therefore play an important role. Although there are many models describing finite temperatures in cold gases in isolation, none of them has been applied to hybrid systems so far.

This thesis outlines how the Zaremba-Nikuni-Griffin (ZNG) model can be used to numerically simulate different hybrid systems. ZNG is a method, which in addition to a mean-field description of a Bose condensate, also gives a full dynamical description of thermal excitations. The thesis presents a parallel implementation of this method, which uses adaptive square collision cells to calculate collision integrals. It therefore allows for the simulation of arbitrary trap geometries on high-performance computers. With the help of this implementation a cloud in front of a solid surface is simulated and atom-loss as well as condensate-growth curves are presented. Furthermore, simulation results of a single trapped ion in a thermal gas, modeled by a quantum Boltzmann equation, are shown. Where possible the simulation results are compared with experimental data for both systems to confirm the applicability of the models. In addition, effects of an oscillating nanotube on the coherence of a cold cloud are examined. Beside simulations with the ZNG model, a system with a pure condensate, which is modeled using the Gross-Pitaevskii equation, is also investigated. The remaining condensate fraction is determined by the Penrose-Onsager criterion. Both methods reveal resonance frequencies that are much smaller than the typical thermal oscillation frequencies of a nanotube. Such oscillations are therefore unlikely to alter the coherence of a condensate.

Zusammenfassung

Ein wachsendes Interesse an Experimenten mit hybriden Systemen, die aus kalten Atomen und Nanostrukturen oder einzelnen, gefangenen Ionen bestehen, hat die Nachfrage nach theoretischen Werkzeugen geschaffen, um diese Systeme zu beschreiben. Da in diesem Zusammenhang oft ein Kühlen oder Aufheizen der Wolke beobachtet wurde, spielen endliche Temperaturen dabei eine gesonderte Rolle. Obwohl es viele Modelle gibt, mit denen man endliche Temperaturen in kalten Gasen beschreiben kann, wurde bisher keines auf hybride Systeme angewandt.

Diese Arbeit zeigt auf, wie das Zaremba-Nikuni-Griffin Modell (ZNG) verwendet werden kann um unterschiedliche hybride Systeme numerisch zu simulieren. ZNG ist eine Methode, die neben der Beschreibung eines Bose-Kondensats in Molekularfeldnäherung, außerdem eine voll dynamische Beschreibung von hochenergetischen, thermischen Anregungen in kondensierten Bose-Gasen liefert. Die Arbeit stellt eine parallele Implementation der Methode vor, die adaptive, rechteckige Kollisionszellen verwendet um Kollisionsintegrale zu berechnen. Dadurch wird eine Simulation von beliebigen Fallengeometrien auf Hochleistungsrechnern möglich. Mithilfe dieser Implementierung wird eine bosonische, kalte Wolke vor einer Oberfläche simuliert und Atomverlust- sowie Kondensatwachstumskurven präsentiert. Darüber hinaus werden Simulationsergebnisse eines einzelnen, gefangenen Ions in einer thermischen Wolke, die durch eine Quantenboltzmanngleichung beschrieben wird, vorgestellt. Für beide Systeme werden nach Möglichkeit die Simulationsergebnisse mit experimentellen Daten verglichen, um die Anwendbarkeit der genutzten Modelle zu zeigen. Zusätzlich werden die Effekte eines oszillierenden Kohlenstoffnanoröhrchens auf die Kohärenz einer kalten Wolke untersucht. Neben Simulationen mit dem ZNG Modell wird außerdem ein System mit einem reinen Kondensat, das mithilfe der Gross-Pitaevskii Gleichung beschrieben wird, betrachtet. Der Kondensatanteil wird dabei durch das Penrose-Onsager Kriterium bestimmt. Beide Methoden offenbaren eine Resonanzfrequenz, die weit unter der thermischer Anregungen liegt, was einen Kohärenzverlust durch thermische Oszillationen des Röhrchens unwahrscheinlich macht.

Introduction

Exploring the “small”

In 1959, one of the leading theoretical physicists, Richard P. Feynman, held a talk in front of the American Physical Society at the California Institute of Technology [1]. In this visionary lecture with the title “There’s plenty of room at the bottom” he explained the enormous potential of “manipulating and controlling things on a small scale” for new technologies and science in general. When talking of a “small scale” he dreamed of the smallest scale possible, without defying any fundamental physical laws, down to manipulating single atoms or molecules.

In his lecture Feynman had foreseen the great opportunities that lie in miniaturization and control of the “small”, and it is often referred to as the date of birth of nanotechnology.[1] Now, some fifty years later, we may estimate how much “plenty” in that context really is. Simple, artificial biological components can be used as little swimming machines on the micro scale [3, 4] and there have been serious considerations to use microrobots in future medicine [5]. On an even smaller scale, scanning tunneling microscopes are used to address single molecules, which are adsorbed on a surface [6, 7], with the hope of using them as small molecular nano-machines [8, 9]. Feynman’s wish to store a piece of information in a cube of 125 atoms was recently even surpassed by reality, when IBM research scientists used antiferromagnetic nanostructures, composed of just 12 Fe atoms, to form a bit [10].

A new definition of cold

However nanotechnology is not the only field that is devoted to the investigation of the “small”. Just in the same year as Feynman gave his famous lecture, the physicist Gould presented ideas about a coherent light source [11]. His

---

[1] However, this is only justified retrospectively because the published article was only cited seven times in twenty years after publication [2].

"LASER" (Light Amplification by Stimulated Emission of Radiation) used ideas of Schawlow and Townes [12], who filed a patent application the year before, and included an open resonator, which was proposed independently by Prokhorov [13]. The first functioning Laser was built by Maiman in 1960 [14] and Townes, Prokhorov and Basov shared the Noble prize in 1964 for their pioneering work on Lasers and Masers (Microwave Amplification by Stimulated Emission of Radiation). The fact that this Nobel prize was well deserved is now more evident than ever. The laser revolutionized atomic spectroscopy, found its way into almost every technological sector and opened the gates for two completely new fields in physics investigating the "small": quantum optics and cold atoms [15, 16]. In 1970 an ensemble of atoms was successfully trapped using laser light [17] and in the following decades lasers were used to store and cool neutral atoms [18, 19]. This work was honored by a Nobel prize in 1997 for Chu, Cohen-Tannoudji and Philips [20] and it would not be the last in the field.

Laser cooling techniques combined with evaporative cooling of atomic clouds enabled the achievement of Bose-Einstein condensation (BEC) in 1995 [21, 22], a long term goal in experimental physics. The BEC, which arises due to a many-body quantum mechanical effect, was theoretically predicted by Bose and Einstein for an ideal Bose gas in 1924. In his work Bose predicted that the ground state of a homogeneous gas of particles with integer spin is macroscopically occupied below a critical temperature T_c.

A BEC reveals the quantum nature of particles on a scale that is visible to the naked eye. Particles residing in the ground state act as one single super sized atom, which exhibits the wave-like nature of quantum objects. A BEC is therefore an ideal probe of single-particle quantum effects, which govern the physics on the "small" scale. In addition, there is hope to study so far unexplored quantum mechanical many-body effects in solid-state physics or to model Bose-Hubbard-like Hamiltonians [23, 24] by placing a BEC in an optical lattice and thereby simulating a simplified, periodic potential of a solid. The BEC is a great example for Feynman's statement that research on a small scale "might tell us much of great interest about the strange phenomena that occur in complex situations" and it came as no surprise that the first realization of BECs was awarded with the Nobel prize in 2001, which was shared between Cornell, Ketterle and Wieman [25].

Following this, research in quantum optics continued with great success and in the last decade it may be said that it has finally broken through to fundamental physical laws at the "bottom". Haroche and Wineland both independently developed ground-breaking experiments, in which measurements with single quantum particles in a well defined state could be performed [26, 27]. They also shared a Nobel prize in 2012 for their work [28].

Hybrid Systems

Despite the progress in nanotechnology and in the manipulation of cold atoms, both fields stayed separated for a long time. Yet, without knowing, it was Feynman again who greatly motivated a link between the two research fields at “the bottom”. In 1982 he proposed how computers should be used in the context of simulating quantum systems [29]. He showed that the complexity of a many-body quantum system scales exponentially with the particle number on a classical computer and hence calculations for larger systems become simply impossible. He therefore suggested replacing the classical by a quantum mechanical computer. A classical computer is based on a register of bits, which either take the value 1 or 0. However, a quantum computer works with qubits $|x\rangle$, which are in an arbitrary superposition between the two states $|0\rangle$ and $|1\rangle$,

$$|x\rangle = a\,|0\rangle + b\,|1\rangle\,, \quad a{,}b \in \mathbb{C}, \quad |a|^2 + |b|^2 = 1. \tag{1}$$

In a quantum computer qubits are generally not addressed one by one, as in the case of a classical computer, but algorithms work on a wavefunction representing the whole system or a well-defined subsystem. By entangling N qubits this wavefunction becomes a vector in a 2^N dimensional Hilbert space; this means a single state of N qubits is given by 2^N complex numbers instead of N numbers which are either 0 or 1, as in the classical case. By performing a measurement on a subsystem of qubits, the entanglement between qubits may additionally provide information about the whole system.

Although a quantum computer is a powerful tool, its realization poses many challenges, which were summarized by DiVincenzo [30]. Single ions confined in Paul traps are the most successful approach to meet all these criteria so far [31–33]. However, there are also other promising systems. Small solid-state devices such as superconducting circuits [34–37] have indisputable advantages. They can be well controlled, addressed and are scalable, making them a strong candidate for quantum computation. However, their main problem is the comparably small coherence time, which is on the timescale of tens of microseconds [38]. To use all the advantages of a quantum register, the single qubits have to stay in a coherent, entangled superposition state throughout the calculation. Even the highest coherence times observed in Josephson junctions so far (about 0.2 ms [39]) are not sufficient to store quantum information during a calculation.

To solve the problem of decoherence, the field of cold atoms may come in handy. Trapped atoms only weakly interact with their environment and coherent states in atomic clocks can be preserved over tens of seconds [40]. Developing quantum hybrid systems, consisting of small solid-state devices and cold atoms may therefore yield the opportunity to combine the respective advantages of both fields. A quantum computer may be built by ultra-cold atoms storing the quantum information, which are coupled to solid-state devices used for processing and addressing [41–44]. So, when Feynman discussed how computers should be used to simulate physics, he may have brought together two fields that explore the “small” down to fundamental physical laws.

However, despite all the things he foresaw in 1959, he might have been even too pessimistic about a subtle issue. He mentioned that the research field, which explores things on a small scale, is a bit different from other physical fields in a sense, “that it will not tell us much of fundamental physics”. When it comes to hybrid systems of cold atoms and nanotechnology this might not be the case. These systems are already used as precision measurement tools [45] for fundamental forces between atoms and solid objects. This includes the determination of Casimir-Polder forces [46, 47], and even beyond that there is hope to measure gravitational forces in the sub-micron limit [48, 49]. For the latter, experimentalists look for deviations from the expected inverse square law on a short range [50] in order to measure forces which are not compatible with the standard model. In addition, the exact mechanisms of decoherence and the transition between classical and quantum behavior can be studied using these systems [51], an issue which is still not well understood (for a detailed discussion of the problem see, for example, [52]).

Another hybrid system allowing one to explore new physical effects is a single ion coupled to a cold atom cloud. An ion can be confined in a Paul trap, laser cooled and immersed in a neutral atom cloud. Because of the large scattering cross section between the ion and the neutral atoms, collisions at very low temperatures, where only a few partial waves contribute, can be efficiently investigated [53–55]. Additionally, the high controllability of the ion may be used to study polaron physics because the ion represents a small impurity in the cloud [56]. Polarons are quasi particles, consisting of an impurity and the coupling to its surrounding environment. Because of the strong interactions between the ion and a neutral atom, this polaron might even be in the strong coupling regime (Fröhlich Polaron) [57], which has not been detected in experiments so far.

Despite the richness of hybrid systems their realization remained inaccessible for a long time due to the high complexity of the experimental set up. This changed dramatically after the advent of microchip traps in the 90s, which greatly simplified the manipulation of cold atomic clouds [58–63]. With their help, the position of a cold atomic cloud, and therefore the coupling between the cloud and a macroscopic object or a single trapped ion, can be well controlled. Thus, over the last decade microchip traps have led to an ongoing increase in the number of experiments in the field.

Finite temperature

The growing number of hybrid experiments has raised the need for theoretical descriptions. However, there is a current lack of suitable finite temperature methods to describe a cold gas coupled to a solid structure or a single trapped ion. Finite temperatures are of special interest in these systems, because energy transfer between the two components and losses in the atom cloud have been observed, resulting in heating or cooling of the cloud.

The dynamics of a BEC are often described by a time-dependent Gross-Pitaevskii equation (GPE). However, this equation is only adequate for a dilute condensed gas in the s-wave regime, neglecting quantum as well as thermal fluctuations. The GPE assumes that all particles are in the ground state and it is therefore, strictly speaking, a zero-temperature model. Several models have been developed, which are used to describe finite temperatures for condensed Bose gases in isolation (for a detailed overview see [64]). Each of these models is based on certain approximations and they therefore neglect physical effects to some extent. Whether these effects are actually negligible depends on the specific problem one wants to describe. For example, a class of finite temperature models can be summarized as so-called classical field methods [65–68]. These are based on the fact that beside the ground state, higher lying modes are also macroscopically occupied at low temperatures. Within the classical field methods, the evolution of these modes is described by a GPE, and hence these modes are treated as classical fields just like the condensate. The models introduce a projection operator projecting the wavefunction into the coherent region, consisting of the highly occupied modes. This is often referred to as the projected GPE. A big advantage of this approach is, that it describes thermal fluctuations within the coherent region. Thermal as well as quantum fluctuations are strongly present in the region of the BEC phase transition. However, the projected GPE neglects quantum fluctuations and all higher lying modes, which may, in total, contain lots of particles despite relatively low occupation numbers.

It is possible to implement higher-lying, non-coherent modes into this approach by coupling a thermal heat bath to the coherent region. The resulting equation, the so-called stochastic GPE [69–71], contains additional source and noise terms. The source term considers particle exchange between the thermal region and the BEC, and the noise term provides the description of fluctuations, which are crucial for the phase transition. However, it should be noted that this method does not describe dynamics in the higher energy thermal cloud, which may be important in certain setups and can also affect the lower-lying modes.

Another approach, which is based on the pioneering work of Kirkpatrick and Dorfman [72], was developed by Zaremba, Nikuni and Griffin [73–75] (ZNG). This method relies on the Hartree-Fock and Popov approximation. It treats thermal excitations semi-classically, leading to a Boltzmann equation coupled to a generalized GPE for the condensate. In this scheme binary collisions are considered by means of collision integrals and a source term in the generalized GPE allows for particle exchange between the two regions. In addition ZNG yields a full dynamical description of the thermal cloud. However, fluctuations are neglected within this model, because it only considers expectation values of the Bose field operator.

The presented finite-temperature models have been used to study Bose gases in isolation, but none have been used in the context of hybrid systems so far. This thesis is a first attempt to apply a sophisticated finite-temperature model for cold bosonic gases to hybrid systems. The focus of the presented studies is on the cold Bose gas and the second component of the hybrid systems (solid state structure or single ion) is described in a rather simplified way. However, the numerical description of the whole system contains the dominant physical effects and where possible the discussion is supported by experimental data, to confirm the applicability of the models.

Outline

This thesis begins by providing the mathematical background for the description of a condensed Bose gas. This is done by exploring the effect of condensation in an ideal gas. The work then proceeds by describing a weakly interacting, dilute gas at zero temperature, leading to the GPE. Afterwards the Thomas-Fermi approximation and the Bogolioubov spectrum are presented. Finite temperatures are introduced within the symmetry breaking approach. A generalized GPE is derived, which allows for particle exchange and a mean-field coupling between the thermal cloud and the condensate. When treating thermal excitations semi-classically, the thermal cloud can be described by a quantum Boltzmann equation. The coupling between the two equations within the ZNG model via collision integrals and mean-field terms is discussed.

Chapter 2 shows how the derived equations can be solved numerically. First this is done for the equilibrium case, for which an example is presented and discussed, followed by the time-dependent, collisionless motion. Afterwards, a detailed discussion of the calculation of the collision integrals is given and a procedure for parallelization of the ZNG model is examined. To test the written algorithms, simple physical problems are investigated at the end of chapter 2.

In the subsequent chapters the acquired tools are applied to three different hybrid systems. The first and most common system is a cold cloud in front of a solid surface. Atom losses as well as condensate growth due to the surface are considered and compared with experiments in chapter 3. In chapter 4 a hot ion is immersed in a cold thermal cloud. With the help of semi-classical cross sections for collisions between the ion and a neutral atom, the effects of excess micromotion on atom losses are analyzed and a non-equilibrium density depletion is observed and quantified. The third and final system consists of an oscillating carbon nanotube, which is coupled to a BEC. In a first attempt the coherence loss of a pure BEC depending on the oscillation frequency and amplitude is estimated by calculating and diagonalizing the one-particle density matrix. Afterwards the system is studied using the ZNG method and condensate fractions as well as density plots are shown. All results are summarized in chapter 6 and the thesis ends with a discussion about possible future work.

Chapter 1

Theory of Bose gases

This chapter provides the theoretical basis for further considerations and it is mainly based on common literature in the field [64, 76–79]. First the phenomenon of Bose-Einstein condensation is explored in the context of an ideal gas, followed by a discussion of the fundamental system Hamiltonian of an interacting Bose gas in a trapping potential. With the help of this Hamiltonian the Gross-Pitaevskii equation (GPE), a working model for temperature $T = 0$, is derived using the concept of symmetry-breaking. Further approximations lead to formulas for the density and width of the ground state in a trap, where a spatially slowly varying wavefunction is assumed. By analyzing small fluctuations around the solution of the static GPE, a first expansion towards a finite temperature model can be found. This leads to expressions for the dispersion relation of quasi-particle excitations, the so-called Bogoliubov spectrum.

A description beyond mean-field for a Bose-Einstein condensate (BEC) at finite temperatures is then presented in the form of a generalized GPE. This equation contains a source term, which gives rise to particle exchange between the thermal cloud and the condensate. Based on the work of Kirkpatrick and Dorfman [72] it can be shown that the time evolution of the distribution function for the thermal excitations can be described by a quantum Boltzmann equation. This equation consists of a free-streaming term, describing the time evolution in a mean-field potential, and collision integrals. These integrals describe scattering events between two thermal atoms and between a thermal atom and the condensate. In the ZNG formalism the two equations are coupled by the mean-field and by the collision integrals of the quantum Boltzmann equation [79], which also define the source term appearing in the generalized GPE. In thermal equilibrium this yields an analytical expression for the thermal density as well as a description for the condensate density. These expressions can be used in order to calculate equilibrium states, which are the starting point of every dynamical simulation in this work.

1.1 Bose-Einstein condensation

A classical gas of identical particles at room temperature can be described by a Boltzmann distribution function, which neglects the statistics and therefore the nature of the described particles. However, when going to lower temperatures, the neglected statistics become more and more important and in the case of a bosonic gas they may even lead to a phase transition, the so-called Bose-Einstein condensation. In a condensed Bose gas the majority of particles gather in the state with lowest energy, building a macroscopic object with quantum-mechanical properties. This phase transition can be understood when calculating the distribution function $f(\epsilon_\nu)$ for a non-interacting Bose gas in the grand canonical ensemble [80]

$$f(\epsilon_\nu) = \frac{1}{e^{\beta(\epsilon_\nu - \mu)} - 1}, \tag{1.1}$$

where $\beta = 1/k_B T$, with k_B being the Boltzmann constant and T the temperature of the gas. The chemical potential μ is the energy needed to add a particle to the system and ϵ_ν is the energy of the single-particle state $|\nu\rangle$. At high temperatures the chemical potential is much smaller than ϵ_ν, and therefore the mean occupation numbers are small. In general the chemical potential has to be smaller than ϵ_ν for all ν, because otherwise the occupation numbers in Eq. (1.1) could become negative, which is unphysical. Hence μ must fulfill the constraint

$$\mu \leq \epsilon_0 \tag{1.2}$$

where ϵ_0 is the lowest Eigenvalue of the single-particle Hamiltonian. When the gas becomes colder, the chemical potential increases and eventually reaches the extreme case where $\mu = \epsilon_0$. As a consequence the mean occupation number of the ground state $f(\epsilon_0)$ diverges and the ground state becomes macroscopically occupied. In the case of a harmonic oscillator one may calculate an expression for the transition temperature T_c, at which condensation takes place, by evaluating the number of excited particles N_{ex} in the system

$$N_{\mathrm{ex}}(T{,}\mu) = \int_{0^+}^{\infty} d\epsilon\, g(\epsilon) f(\epsilon). \tag{1.3}$$

Here $g(\epsilon)$ is the density of states, i.e. $g(\epsilon)d\epsilon$ gives the number of states with energy between ϵ and $\epsilon + d\epsilon$. The lower bound 0^+ of the integral in Eq. (1.3) emphasizes the fact that the ground state is explicitly excluded from the calculation. When the particle number N is very high, the zero-point energy ϵ_0 may be neglected and as a consequence the integral in Eq. (1.3) achieves its highest value for $\mu = 0$. In addition, all particles N of the system are distributed over the excited states at T_c, so that

$$N = N_{\mathrm{ex}}(T_c,\mu = 0) = \int_{0^+}^{\infty} d\epsilon g(\epsilon) \frac{1}{e^{\epsilon/k_B T_c} - 1}. \tag{1.4}$$

For a gas in a three dimensional harmonic oscillator potential this integral leads to an equation for T_c

$$T_c \approx 0.94 \frac{\hbar}{k_B} \bar{\omega} N^{1/3} \tag{1.5}$$

where $\bar{\omega} = (\omega_x \omega_y \omega_z)^{1/3}$, with trapping frequencies $\omega_{i=x,y,z}$ in the x, y and z directions.

The discussion so far was based on the assumption of a non-interacting gas. This chapter now proceeds with a description of a weakly interacting, dilute Bose gas, for which it is possible to derive equations, which govern the time evolution of the condensate and of the excited atoms.

1.2 System Hamiltonian

The starting point for all further theoretical considerations about Bose gases in this work is a Hamiltonian, which describes thermal and quantum fluctuations as well as two-body interactions. Using Bose field operators in second quantization this Hamiltonian takes the general form

$$\begin{aligned} \hat{H} = &\int d\mathbf{r} \hat{\Psi}^\dagger(\mathbf{r},t) \hat{h}_0(\mathbf{r}) \hat{\Psi}(\mathbf{r},t) \\ &+ \frac{1}{2} \int \int d\mathbf{r} d\mathbf{r'} \hat{\Psi}^\dagger(\mathbf{r},t) \hat{\Psi}^\dagger(\mathbf{r}',t) V(\mathbf{r} - \mathbf{r'}) \hat{\Psi}(\mathbf{r},t) \hat{\Psi}(\mathbf{r}',t), \end{aligned} \tag{1.6}$$

where $V(\mathbf{r} - \mathbf{r}')$ denotes the two-body interaction potential. The Bose field operators

$$\hat{\Psi}(\mathbf{r},t) = \sum \hat{a}_i(t) \varphi_i(\mathbf{r},t) \tag{1.7}$$

$$\hat{\Psi}^\dagger(\mathbf{r},t) = \sum \hat{a}_i^\dagger(t) \varphi_i^*(\mathbf{r},t) \tag{1.8}$$

are defined as a linear combination over a basis of single-particle states $|i\rangle$ with single-particle wavefunctions $\varphi_i(\mathbf{r},t) = \langle \mathbf{r} \,|\, i \rangle$, complex conjugated wavefunctions $\varphi_i^*(\mathbf{r},t)$ and corresponding annihilation $\hat{a}_i(t)$ and creation $\hat{a}_i^\dagger(t)$ operators. These operators obey the bosonic commutation relations

$$[\hat{a}_i,\hat{a}_j^\dagger] = \delta_{ij} \tag{1.9}$$

$$[\hat{a}_i,\hat{a}_j] = [\hat{a}_i^\dagger,\hat{a}_j^\dagger] = 0 \tag{1.10}$$

and therefore give rise to Bose statistics. Thus $\hat{\Psi}(\mathbf{r},t)$ ($\hat{\Psi}^\dagger(\mathbf{r},t)$) annihilates (creates) a boson at point $\mathbf{r}$ and time t when applied to a Fock state. The term $\hat{h}_0 = -\hbar^2\nabla^2/(2m) + V_{\text{ext}}(\mathbf{r},t)$ in Eq. (1.6) is the Hamiltonian of a single particle with mass m in an external potential $V_{\text{ext}}(\mathbf{r},t)$. For a gas in a harmonic trap the potential reads

$$V_{\text{ext}}(\mathbf{r}) = \frac{1}{2}m\omega_x^2x^2 + \frac{1}{2}m\omega_y^2y^2 + \frac{1}{2}m\omega_z^2z^2, \tag{1.11}$$

where x,y and z denote position variables in the three different dimensions and $\omega_{i=x,y,z}$ are the corresponding trap frequencies. In the case of a dilute gas at low temperatures only s-wave scattering is relevant for the atomic interactions and the term $V(\mathbf{r}-\mathbf{r}')$ in Eq. (1.6) can be replaced by a contact potential

$$V(\mathbf{r}-\mathbf{r}') = g\delta(\mathbf{r}-\mathbf{r}'), \tag{1.12}$$

with the interaction strength $g = 4\pi\hbar^2a/m$, where a is the s-wave scattering length.

For further considerations it is useful to analyze the system in the Heisenberg picture, where only the operators are time dependent. The equations of motion, which describe the time evolution of the system, are then given by a commutator of an operator $\hat{O}(t)$ in the Heisenberg picture and the system Hamiltonian $\hat{H}$

$$i\hbar\frac{\partial\hat{O}(t)}{\partial t} = \left[\hat{O}(t),\hat{H}\right]. \tag{1.13}$$

Taking the two-body contact interactions of Eq. (1.12) into account, the equation of motion for the field operator takes the form

$$\begin{aligned} i\hbar\frac{\partial\hat{\Psi}(\mathbf{r},t)}{\partial t} &= [\hat{\Psi}(\mathbf{r},t),\hat{H}] \\ &= \hat{h}_0\hat{\Psi}(\mathbf{r},t) + g\hat{\Psi}(\mathbf{r},t)^\dagger\hat{\Psi}(\mathbf{r},t)\hat{\Psi}(\mathbf{r},t). \end{aligned} \tag{1.14}$$

Replacing the atomic interactions by a contact interaction potential is the only approximation made so far, i.e. Eq. (1.14) is an analytical description for a cold, dilute Bose gas. A range of different approaches start from this general description and simplify the equation of motion using further approximations. One common approximation is the so-called concept of symmetry-breaking which was first introduced by Bogolioubov [81].

1.2.1 Symmetry breaking

In the case of a condensed Bose gas, the ground state of the system is macroscopically occupied and plays a special role in the theoretical description. It is therefore convenient to split the field operator into a condensed

$$\hat{\Phi}(\mathbf{r},t) = \hat{a}_0(t)\varphi_0(\mathbf{r},t) \tag{1.15}$$

and a non-condensed part

$$\hat{\delta}(\mathbf{r},t) = \sum_{i\neq 0} \hat{a}_i(t)\varphi_i(\mathbf{r},t) \tag{1.16}$$

in a given basis set $\{\varphi_0,\varphi_{i=1,2,\dots}\}$, where φ_0 is the single-particle wavefunction of the macroscopically occupied state. The field operator can then be written in the form [77]

$$\hat{\Psi}(\mathbf{r},t) = \hat{\Phi}(\mathbf{r},t) + \hat{\delta}(\mathbf{r},t). \tag{1.17}$$

As $\hat{\Phi}(\mathbf{r},t)$ annihilates an atom in a macroscopically occupied state one can make the Bogolioubov replacement, i.e. replacing the operator $\hat{a}_0$ by $\sqrt{N_0}$ where N_0 is the number of ground state atoms. As a result the field operator for the ground state is replaced by a complex number

$$\Phi(\mathbf{r},t) = \sqrt{N_0}\varphi_0(\mathbf{r},t), \tag{1.18}$$

which is equivalent to a non-vanishing expectation value of the total field operator

$$\langle\hat{\Psi}(\mathbf{r},t)\rangle = \Phi(\mathbf{r},t). \tag{1.19}$$

The so-called order parameter $\Phi(\mathbf{r},t)$ of the condensate now describes a classical field. Therefore quantum fluctuations are completely neglected for the ground state and only appear in the operator $\hat{\delta}(\mathbf{r},t)$. This replacement is a good approximation if the addition or removal of a particle has no major effect on the Fock-state itself, i.e. for a given Fock-state $|N_0\rangle$ containing N_0 particles

$$\hat{a}_0\,|N_0\rangle \sim |N_0-1\rangle \approx |N_0\rangle \tag{1.20}$$

$$\hat{a}_0^\dagger\,|N_0\rangle \sim |N_0+1\rangle \approx |N_0\rangle\,, \tag{1.21}$$

which is valid for large occupation numbers as in the case of a BEC.

Nevertheless, this step has extensive consequences for the underlying Hamiltonian. The original Hamiltonian in Eq. (1.6) is invariant under a gauge transformation in the phase of the Bose field operator, that means changing the phase does not change the physics of a system. This no longer holds true for the order parameter $\Phi(\mathbf{r},t)$ with a fixed but arbitrary phase. Therefore the approximation is referred to as "symmetry-breaking". Combining this with Eq. (1.14) leads directly to a useful model for temperatures far below T_c as outlined in the next section.

1.3 Zero-temperature theory

In the case of zero temperature $T = 0$, all the particles are in the ground state and the operators $\hat{\delta}$, $\hat{\delta}^\dagger$ can be neglected. The equation of motion for the field operator (1.14) together with Eq. (1.17) then takes the form of a non-linear Schrödinger equation

$$i\hbar\frac{\partial\Phi(\mathbf{r},t)}{\partial t} = \left[-\frac{\hbar^2}{2m}\nabla^2 + V_{\text{ext}}(\mathbf{r},t) + g|\Phi(\mathbf{r},t)|^2\right]\Phi(\mathbf{r},t), \tag{1.22}$$

the so-called GPE. In this form the wavefunction is normalized to the total condensate atom number $\int d\mathbf{r}|\Phi(\mathbf{r},t)|^2 = N_c$. Although it was derived for the $T = 0$ case, the GPE provides a good description for temperatures up to $T \approx T_c/2$ and it was initially used to study vortices in Bose superfluids [82, 83].

In order to calculate equilibrium properties of a Bose gas at $T = 0$ the equilibrium solution of Eq. (1.22), which takes the form [79]

$$\langle\hat{\Psi}(\mathbf{r},t)\rangle = \Phi(\mathbf{r},t) = \Phi_0(\mathbf{r})e^{-i\mu_{c0}t/\hbar}, \tag{1.23}$$

can be substituted in Eq. (1.22). Here μ_{c0} is the equilibrium chemical potential of the condensate, which describes the change in energy when a particle is added to the system. Using Eq. (1.23) in the GPE (1.22) leads to a static equation

$$\mu_{c0}(\mathbf{r})\Phi_0(\mathbf{r}) = \left[-\frac{\hbar^2}{2m}\nabla^2 + V_{\text{ext}}(\mathbf{r}) + g|\Phi_0(\mathbf{r})|^2\right]\Phi_0(\mathbf{r}). \tag{1.24}$$

This is the so-called time-independent GPE and it results in a chemical potential of the form

$$\mu_{c0}(\mathbf{r}) = -\frac{\hbar^2\nabla^2\sqrt{n_{c0}(\mathbf{r})}}{2m\sqrt{n_{c0}(\mathbf{r})}} + V_{\text{ext}}(\mathbf{r}) + gn_{c0}(\mathbf{r}), \tag{1.25}$$

where $n_{c0}(\mathbf{r}) = |\Phi_0(\mathbf{r})|^2$ is the equilibrium density of the condensate.

1.3.1 Thomas-Fermi limit

A first approximation to solve Eq. (1.24) is to neglect the kinetic energy of the condensate, i.e. to neglect the $-\hbar^2\nabla^2/2m$ term. This is convenient in cases where the interaction potential dominates, and hence when the particle number is high. Neglecting the kinetic energy leads to a static GPE of the form [84]

$$V_{\text{ext}}(\mathbf{r}) + g|\Phi_0(\mathbf{r})|^2 = \mu_{c0}. \tag{1.26}$$

This equation can be used to calculate the shape and size of the condensate

$$n_{c0}(\mathbf{r}) = \frac{1}{g}\left[\mu_{c0} - V_{\text{ext}}(\mathbf{r})\right] \geq 0. \tag{1.27}$$

The boundary of the cloud, $\mathbf{R}$, can therefore be inferred from

$$V_{\text{ext}}(\mathbf{R}) = \mu_{c0} \tag{1.28}$$

and in the case of a harmonic oscillator with frequencies $\omega_{i=x,y,z}$ this becomes

$$R_i^2 = \frac{2\mu_{c0}}{m\omega_i^2}. \tag{1.29}$$

R_i is often referred to as the Thomas-Fermi radius. Combined with the condition for the total particle number in a BEC, $N_c = \int d\mathbf{r} n_{c0}(\mathbf{r})$, one finds for an isotropic trap $\omega_x = \omega_y = \omega_z = \omega_0$

$$\mu_{c0} = \frac{\hbar\omega_0}{2}\left(\frac{15N_c a}{a_{ho}}\right)^{2/5}, \tag{1.30}$$

where $a_{\text{ho}} = \sqrt{\hbar/m\omega_0}$ is the oscillator length. Eq. (1.29) and Eq. (1.30) lead to an expression for the Thomas-Fermi radius, which depends only on the mass, scattering length, particle number and trap frequencies

$$R_{\text{TF}} = a_{\text{ho}}\left(\frac{15N_c a}{a_{\text{ho}}}\right)^{1/5}. \tag{1.31}$$

It can be seen from Eq. (1.27) that the condensate density profile takes the form of the negative trapping potential, which in case of a harmonic oscillator is a three-dimensional paraboloid. Although this is a very good approximation for large condensate atom numbers, the edge of the condensate density differs significantly from a realistic distribution. In the Thomas-Fermi approximation the density abruptly vanishes at $r = R_{\text{TF}}$. This would lead to an infinitely high kinetic energy and is therefore unphysical. In fact the operator for the kinetic energy $-\hbar^2\nabla^2/2m$ leads to a more gradual decrease.

1.3.2 Bogoliubov excitation spectrum

Although derived for $T = 0$, it is possible to describe quasi-particle excitations, which arise due to mean-field coupling, with the help of the GPE (Eq. (1.22)). In order to do so, the wavefunction can be written in the form

$$\Phi(\mathbf{r},t) = e^{-i\mu t/\hbar}\left[\Phi_0(\mathbf{r}) + \delta\Phi(\mathbf{r},t)\right], \tag{1.32}$$

where $\delta\Phi(\mathbf{r},t)$ represents a perturbation of the static condensate wavefunction. If this perturbation is small ($\delta\Phi(\mathbf{r},t) \ll \Phi_0(\mathbf{r},t)$), powers of $\delta\Phi(\mathbf{r},t)$ greater than 1 can be neglected, which is often referred to as linearization. In the case of a uniform gas ($V_{\text{ext}} = 0$) this leads to an analytical expression for the collective oscillations in the system. This can be seen by substituting Eq. (1.32) into Eq. (1.22) and subtracting Eq. (1.24)

$$\begin{aligned} i\hbar\frac{\partial}{\partial t}\delta\Phi(\mathbf{r},t) = &\left[-\frac{\hbar^2}{2m}\nabla^2 + 2g|\Phi_0(\mathbf{r})|^2 - \mu_{c0}\right]\delta\Phi(\mathbf{r},t) \\ &+ g\Phi_0(\mathbf{r})^2\delta\Phi^*(\mathbf{r},t). \end{aligned} \tag{1.33}$$

In order to find collective modes for this system, it is convenient to make the ansatz [64]

$$\delta\Phi(\mathbf{r},t) = \sum_l \left[u_l(\mathbf{r})e^{-i\omega_l t} + v_l^*(\mathbf{r})e^{i\omega_l t}\right] \tag{1.34}$$

for the perturbation. This gives a description of quasi-particle amplitudes $u_l(\mathbf{r})$ and $v_l(\mathbf{r})$ for corresponding excitation frequencies ω_l. Substituting Eq. (1.34) together with its complex conjugate into Eq. (1.33) yields two coupled equations for each frequency ω_l

$$\begin{aligned} \left[\hat{T}(\mathbf{r}) + 2gn_{c0}(\mathbf{r})\right]u_l(\mathbf{r}) - 2g|\Phi_0(\mathbf{r})|^2 v_l(\mathbf{r}) &= \epsilon_l u_l(\mathbf{r}) \\ \left[\hat{T}(\mathbf{r}) + 2gn_{c0}(\mathbf{r})\right]v_l(\mathbf{r}) - 2g|\Phi_0(\mathbf{r})|^2 u_l(\mathbf{r}) &= \epsilon_l v_l(\mathbf{r}), \end{aligned} \tag{1.35}$$

where $\epsilon_l = \hbar\omega_l$ and $\hat{T} = -\hbar^2\nabla^2/2m - \mu_{c0}$. Solutions of these equations take the form of plane waves

$$u_l(\mathbf{r}) = u_{\mathbf{p}}e^{i\mathbf{p}\cdot\mathbf{r}/\hbar} \tag{1.36}$$

$$v_l(\mathbf{r}) = v_{\mathbf{p}}e^{i\mathbf{p}\cdot\mathbf{r}/\hbar}, \tag{1.37}$$

where $\mathbf{p}$ is the momentum of the excitation. By substituting these solutions into Eq. (1.35), one finds a dispersion relation for the quasi-particle excitations [76]

$$\epsilon(\mathbf{p}) = \sqrt{\varepsilon_p^2 + 2gn_{c0}\varepsilon_p}, \tag{1.38}$$

with $\varepsilon_p = p^2/2m$, where p is the magnitude of the momentum vector. For small wavelengths ($p \ll mc$ with $c = \sqrt{gn_{c0}/m}$) this spectrum is phonon like

$$\epsilon(\mathbf{p}) \backsimeq cp \tag{1.39}$$

and describes sound waves propagating through the gas with velocity c. For higher momenta ($p \gg mc$) the excitation energy converges to that of a free particle

$$\epsilon(p) \backsimeq \varepsilon_p + gn_{c0}. \tag{1.40}$$

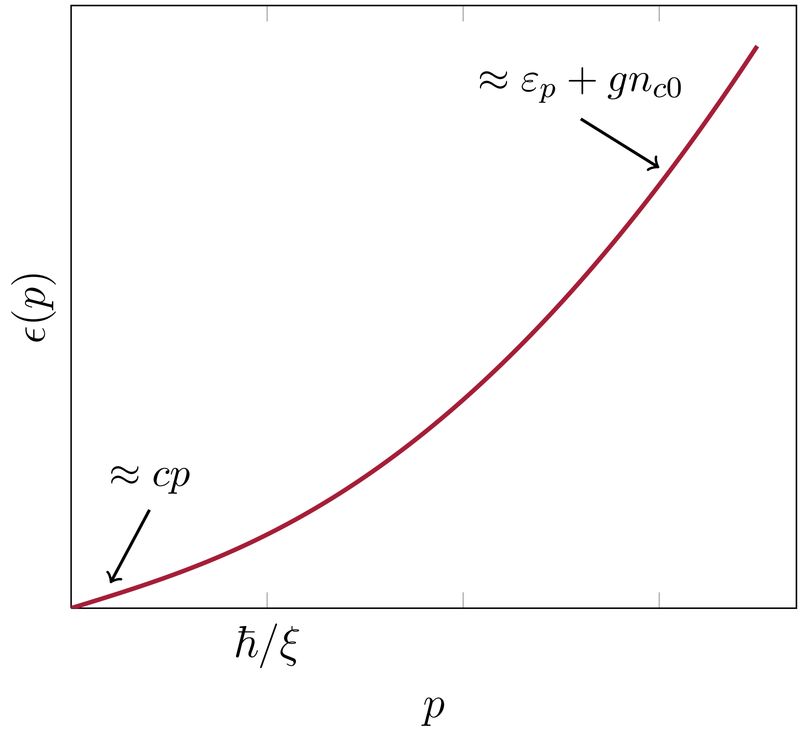

Figure 1.1 – A sketch of the Bogoliubov excitation spectrum for small and large p. For excitations with a small momentum ($p \ll mc$) the dispersion relation is phonon like ($\epsilon(p) = cp$), whereas at large momenta ($p \gg mc$) the dispersion law approaches that of a free particle ($\epsilon(p) = \varepsilon_p + gn_{c0}$). The transition takes place at $p \backsimeq \hbar/\xi$.

The behavior of the dispersion relation $\epsilon(p)$ in the two regimes is sketched in Fig. 1.1. The transition between these regimes takes place at $p \backsimeq \hbar/\xi$, where

ξ is the healing length defined by

$$\xi = \sqrt{\frac{\hbar^2}{2mgn_{c0}}} = \frac{1}{\sqrt{2}}\frac{\hbar}{mc}. \tag{1.41}$$

The healing length describes the distance over which the wavefunction tends to its unperturbed value when subjected to a perturbation.

Although a uniform Bose gas was considered for deriving the behavior in the two different regimes, the dispersion law in Eq. (1.38) also gives information about a condensate in a harmonic trap. If the wavelength of an excitation is smaller than the length scale of the variation of the condensate density, the gas can be thought of as locally homogeneous, and sound waves may propagate through the gas [85]. In addition to this quasi-continuous excitation spectrum of sound waves, there exist bulk oscillations of a BEC in a trap [86, 87], whose excitation spectrum is discrete. This can be seen by solving Eq. (1.35) numerically [88]. Examples for bulk oscillations are dipole modes, which correspond to center of mass oscillations, where the oscillation frequencies are given by the trap frequencies. Other oscillations involve a change of the condensate shape such as the so-called breathing or quadrupole modes.

1.4 Finite temperature

In this section the described theory is expanded in order to describe finite temperatures in a condensed Bose gas. This is done using the so-called Zaremba-Nikuni-Griffin model (ZNG), which consists of a generalized GPE describing the condensate and a quantum Boltzmann equation describing high-energetic thermal excitations.

In order to derive this model the thermal operator $\hat{\delta}$ in Eq. (1.17) is taken into account. In the symmetry-breaking approach the expectation value of the Heisenberg equation of motion (Eq. (1.14)) then becomes

$$\begin{aligned} i\hbar\frac{\partial\Phi(\mathbf{r},t)}{\partial t} = & \left[-\frac{\hbar^2}{2m}\nabla^2 + V_{\mathrm{ext}}(\mathbf{r},t)\right]\Phi(\mathbf{r},t) \\ & + g\langle\hat{\Psi}^\dagger(\mathbf{r},t)\hat{\Psi}(\mathbf{r},t)\hat{\Psi}(\mathbf{r},t)\rangle. \end{aligned} \tag{1.42}$$

By substituting

$$\hat{\Psi}(\mathbf{r},t) = \Phi(\mathbf{r},t) + \hat{\delta}(\mathbf{r},t) \tag{1.43}$$

into the last term, it follows that

$$\begin{aligned}\hat{\Psi}^\dagger\hat{\Psi}\hat{\Psi} =&|\Phi|^2\Phi + \Phi^2\hat{\delta}^\dagger + 2|\Phi|^2\hat{\delta} + \Phi^*\hat{\delta}\hat{\delta}\\ &2\Phi\hat{\delta}^\dagger\hat{\delta} + \hat{\delta}^\dagger\hat{\delta}\hat{\delta}.\end{aligned} \tag{1.44}$$

For clarity reasons dependencies are omitted in this equation. As $\langle\hat{\Psi}(\mathbf{r},t)\rangle = \Phi(\mathbf{r},t)$ it is obvious that $\langle\hat{\delta}(\mathbf{r},t)\rangle = 0$ and therefore the expectation value $\langle\hat{\Psi}^\dagger\hat{\Psi}\hat{\Psi}\rangle$ becomes

$$\langle\hat{\Psi}^\dagger\hat{\Psi}\hat{\Psi}\rangle = n_c\Phi + \tilde{m}\Phi^* + 2\tilde{n}\Phi + \langle\hat{\delta}^\dagger\hat{\delta}\hat{\delta}\rangle, \tag{1.45}$$

with quantities defined as

$$n_c(\mathbf{r},t) = |\Phi(\mathbf{r},t)|^2 \tag{1.46}$$

$$\tilde{n}(\mathbf{r},t) = \langle\hat{\delta}^\dagger(\mathbf{r},t)\hat{\delta}(\mathbf{r},t)\rangle \tag{1.47}$$

$$\tilde{m}(\mathbf{r},t) = \langle\hat{\delta}(\mathbf{r},t)\hat{\delta}(\mathbf{r},t)\rangle, \tag{1.48}$$

where n_c is the local condensate density, $\tilde{n}(\mathbf{r},t)$ is the thermal density and $\tilde{m}(\mathbf{r},t)$ is the so-called anomalous density, because it contains an unequal number of creation and annihilation operators. Expectation values of an unequal number of creation and annihilation operators are supposed to vanish, yet this does not hold true any more when symmetry breaking is assumed. Therefore the anomalous density as well as the term $\hat{\delta}^\dagger\hat{\delta}\hat{\delta}$ in Eq. (1.45) may have a non-zero expectation value [79].

Using Eq. (1.45) in the Heisenberg equation of motion (Eq. (1.42)), it becomes

$$\begin{aligned}i\hbar\frac{\partial\Phi(\mathbf{r},t)}{\partial t} =& \left[-\frac{\hbar^2}{2m}\nabla^2 + V_{\text{ext}}(\mathbf{r},t) + g|\Phi(\mathbf{r},t)|^2 + 2g\tilde{n}(\mathbf{r},t)\right]\Phi(\mathbf{r},t)\\ &+ g\tilde{m}(\mathbf{r},t)\Phi^* + g\langle\hat{\delta}^\dagger(\mathbf{r},t)\hat{\delta}(\mathbf{r},t)\hat{\delta}(\mathbf{r},t)\rangle.\end{aligned} \tag{1.49}$$

1.4.1 Hydrodynamic formulation

By reformulating the problem in the hydrodynamic formulation, Eq. (1.49) can then be used to derive a generalized GPE, giving raise to a mean-field potential of thermal excitations and a source term allowing particle exchange between the thermal and the condensate region.

This is done by expressing the wavefunction $\Phi(\mathbf{r},t)$ in terms of its amplitude $\sqrt{n_c(\mathbf{r},t)}$ and phase θ

$$\Phi(\mathbf{r},t) = \sqrt{n_c(\mathbf{r},t)}e^{i\theta}. \tag{1.50}$$

Substituting Eq. (1.50) into Eq. (1.49) and separating imaginary and real parts leads to [79]

$$\frac{\partial n_c}{\partial t} + \nabla \cdot (n_c \mathbf{v}_c) = \frac{2g}{\hbar} \operatorname{Im} \left[(\Phi^*)^2 \tilde{m} + \Phi^* \langle \hat{\delta}^\dagger(\mathbf{r},t) \hat{\delta}(\mathbf{r},t) \hat{\delta}(\mathbf{r},t) \rangle \right] \tag{1.51}$$

$$\hbar \frac{\partial \theta}{\partial t} = -(\mu_c + \frac{1}{2} m \mathbf{v}_c^2) \equiv -\epsilon_c \tag{1.52}$$

with the condensate velocity $\mathbf{v}_c$

$$\mathbf{v}_c(\mathbf{r},t) = \frac{\hbar}{m} \nabla \theta(\mathbf{r},t) \tag{1.53}$$

and the local time-dependent condensate chemical potential defined by

$$\begin{aligned} \mu_c \equiv & - \frac{\hbar^2 \nabla^2 \sqrt{n_c}}{2m\sqrt{n_c}} + V_{\text{ext}}(\mathbf{r},t) + g n_c(\mathbf{r},t) + 2g\tilde{n}(\mathbf{r},t) \\ & + \frac{g}{\hbar n_c} \operatorname{Re} \left[(\Phi^*)^2 \tilde{m} + \Phi^* \langle \hat{\delta}^\dagger(\mathbf{r},t) \hat{\delta}(\mathbf{r},t) \hat{\delta}(\mathbf{r},t) \rangle \right] . \end{aligned} \tag{1.54}$$

One can show that both $\tilde{m}$ and $\langle \hat{\delta}(\mathbf{r},t)^\dagger \hat{\delta}(\mathbf{r},t) \hat{\delta}(\mathbf{r},t) \rangle$ are of order g [79]. Because the functions involving these terms in Eq. 1.51 and Eq. 1.52 contain another factor of g, their total order is g^2 and they are small if the interaction strength is weak. However, if one wants to describe particle exchange between a thermal cloud and the condensate, the imaginary terms of order of g^2 are important. Therefore the real part of these terms in Eq. 1.51 and Eq. 1.52 is neglected in the following discussion, while keeping the imaginary part [79].

1.4.2 Generalized Gross-Pitaevskii equation

Neglecting the real part of terms of order of g^2 leads to hydrodynamic equations of the form

$$\frac{\partial n_c}{\partial t} + \nabla \cdot (n_c \mathbf{v}_c) = -\Gamma_{12}[f,\Phi] \tag{1.55}$$

$$m(\frac{\partial \mathbf{v}_c}{\partial t} + \frac{1}{2} \nabla v_c^2) = -\nabla \mu_c \tag{1.56}$$

with

$$\mu_c(\mathbf{r},t) = -\frac{\hbar^2 \nabla^2 \sqrt{n_c}}{2m\sqrt{n_c}} + V_{\text{ext}}(\mathbf{r},t) + g n_c(\mathbf{r},t) + 2g\tilde{n}(\mathbf{r},t). \tag{1.57}$$

$\Gamma_{12}[f,\Phi]$ denotes a source term in Eq. (1.55). It is a functional of the condensate wavefunction $\Phi(\mathbf{r},t)$ and the single-particle distribution function $f(\mathbf{r},\mathbf{p},t)$ and is defined as

$$\Gamma_{12}[f,\phi] = -\frac{2g}{\hbar}\,\mathrm{Im}\left[\phi^*(\mathbf{r},t)\langle\hat{\delta}^\dagger(\mathbf{r},t)\hat{\delta}(\mathbf{r},t)\hat{\delta}(\mathbf{r},t)\rangle\right]. \tag{1.58}$$

One can show that Eq. (1.55) and Eq. (1.56) are equivalent to a generalized GPE [70, 89, 90]

$$i\hbar\frac{\partial\Phi}{\partial t} = \left[-\frac{\hbar^2}{2m}\nabla^2 + V_{\mathrm{ext}}(\mathbf{r},t) + gn_c(\mathbf{r},t) + 2g\tilde{n}(\mathbf{r},t) - iR(\mathbf{r},t)\right]\Phi. \tag{1.59}$$

Collisions of thermal atoms with the condensate are then described by $-iR(\mathbf{r},t)$, with

$$R(\mathbf{r},t) = \frac{\hbar\Gamma_{12}[f,\Phi]}{2n_c(\mathbf{r},t)}. \tag{1.60}$$

Because this term is non-hermitian it changes the normalization of the wavefunction and it therefore describes depletion or growth of the condensate due to scattering events.

1.4.3 Quantum-Boltzmann equation

Following the work of Kirkpatrick and Dorfman [72], one can show that the time evolution of the thermal excitations can be approximated by a quantum Boltzmann equation. In order to see that it is useful to look at the time evolution of the thermal field operator $\hat{\delta}$ taking symmetry breaking into account. From Eq. (1.43) it follows that

$$i\hbar\frac{\partial\hat{\delta}(\mathbf{r},t)}{\partial t} = i\hbar\frac{\partial}{\partial t}\left(\hat{\Psi}(\mathbf{r},t) - \Phi(\mathbf{r},t)\right). \tag{1.61}$$

Substituting Eq. (1.14) and Eq. (1.49) into this expression and using Eq. (1.43) yields

$$\begin{aligned} i\hbar\frac{\partial\hat{\delta}(\mathbf{r},t)}{\partial t} &= \left[-\frac{\hbar^2}{2m}\nabla^2 + V_{\mathrm{ext}}(\mathbf{r},t) + 2g(n_c(\mathbf{r},t) + \tilde{n}(\mathbf{r},t))\right]\hat{\delta}(\mathbf{r},t) \\ &\quad - 2g\tilde{n}(\mathbf{r},t)\hat{\delta}(\mathbf{r},t) + g\Phi^2\hat{\delta}^\dagger(\mathbf{r},t) \\ &\quad + g\Phi^*(\mathbf{r},t)\left(\hat{\delta}(\mathbf{r},t)\hat{\delta}(\mathbf{r},t) - \tilde{m}(\mathbf{r},t)\right) \\ &\quad + 2g\Phi(\mathbf{r},t)\left(\hat{\delta}^\dagger(\mathbf{r},t)\hat{\delta}(\mathbf{r},t) - \tilde{n}(\mathbf{r},t)\right) \\ &\quad + g\left(\hat{\delta}^\dagger(\mathbf{r},t)\hat{\delta}(\mathbf{r},t)\hat{\delta}(\mathbf{r},t) - \langle\hat{\delta}^\dagger(\mathbf{r},t)\hat{\delta}(\mathbf{r},t)\hat{\delta}(\mathbf{r},t)\rangle\right). \end{aligned} \tag{1.62}$$

From this equation an effective Hamiltonian H_{eff} can be extracted which satisfies the Heisenberg equation of motion for the thermal field operator

$$i\hbar \frac{\partial \hat{\delta}(\mathbf{r},t)}{\partial t} = \left[\hat{\delta}(\mathbf{r},t), \hat{H}_{\text{eff}}(t)\right] . \tag{1.63}$$

The main contributor to this Hamiltonian is the Hartree-Fock (HF) term

$$\hat{H}_{\text{HF}}(t) = \int d\mathbf{r} \hat{\delta}^\dagger(\mathbf{r},t) \left[-\frac{\hbar^2}{2m}\nabla^2 + V_{\text{ext}}(\mathbf{r},t) + 2gn(\mathbf{r},t) \right] \hat{\delta}(\mathbf{r},t) \tag{1.64}$$

where $n = n_c + \tilde{n}$ is the total density. When written in the form

$$\hat{H}_{\text{eff}}(t) = \hat{H}_{\text{HF}}(t) + \hat{H}'(t) \tag{1.65}$$

the remaining term $\hat{H}'(t)$ can be treated as a perturbation. With the help of this effective Hamiltonian it is possible to calculate the expectation value of any given operator $\hat{O}$ in the system using

$$\langle \hat{O}(t) \rangle = \text{Tr}\left(\hat{\rho}(t_0)\hat{O}(t) \right) \tag{1.66}$$

$$= \text{Tr}\left(\hat{\rho}(t,t_0)\hat{O}(t_0) \right) \tag{1.67}$$

where $\text{Tr}(\hat{\rho}(t,t_0)\hat{O}(t_0))$ denotes the trace over the operator $\hat{\rho}(t,t_0)\hat{O}(t_0)$ and $\hat{\rho}(t,t_0)$ is the density matrix at time t. The time evolution of the density matrix is given by

$$i\hbar \frac{\partial \hat{\rho}(t,t_0)}{\partial t} = \left[\hat{H}_{\text{eff}}(t), \hat{\rho}(t,t_0)\right] . \tag{1.68}$$

In order to derive an equation of motion for the distribution function $f(\mathbf{r},\mathbf{p},t)$ of the thermal cloud, the expectation value of the Wigner operator defined as

$$\hat{f}(\mathbf{r},\mathbf{p},t_0) = \int d\mathbf{r}' e^{i\mathbf{p}\cdot\mathbf{r}'/\hbar} \hat{\delta}^\dagger(\mathbf{r} + \frac{1}{2}\mathbf{r}', t_0)\hat{\delta}(\mathbf{r} - \frac{1}{2}\mathbf{r}', t_0) \tag{1.69}$$

can then be calculated with the help of Eq. (1.66)

$$f(\mathbf{r},\mathbf{p},t) = \langle \hat{f}(\mathbf{r},\mathbf{p},t_0) \rangle = \text{Tr}\left(\hat{\rho}(t,t_0)\hat{f}(\mathbf{r},\mathbf{p},t_0) \right) . \tag{1.70}$$

This distribution function allows one to calculate expectation values of the system like the thermal density $\tilde{n}(\mathbf{r},t)$

$$\tilde{n}(\mathbf{r},t) = \int \frac{d\mathbf{p}}{(2\pi\hbar)^3} f(\mathbf{r},\mathbf{p},t). \tag{1.71}$$

The time derivative of $f(\mathbf{r},\mathbf{p},t)$ then gives the time evolution of the thermal cloud distribution and it describes how significant properties of the cloud change over time. Using Eq. (1.68) one finds

$$\begin{aligned}\frac{\partial f(\mathbf{r},\mathbf{p},t)}{\partial t} =& \frac{1}{i\hbar}\mathrm{Tr}\,\left(\hat{\rho}(t,t_0)\left[\hat{f}(\mathbf{p},\mathbf{r},t_0),\hat{H}_{\mathrm{eff}}\right]\right)\\ =& \frac{1}{i\hbar}\mathrm{Tr}\,\left(\hat{\rho}(t,t_0)\left[\hat{f}(\mathbf{p},\mathbf{r},t_0),\hat{H}_{\mathrm{HF}}\right]\right)\\ &+\frac{1}{i\hbar}\mathrm{Tr}\,\left(\hat{\rho}(t,t_0)\left[\hat{f}(\mathbf{p},\mathbf{r},t_0),\hat{H}'\right]\right).\end{aligned} \tag{1.72}$$

The first term on the right-hand side describes thermal excitations moving around in a Hartree-Fock mean-field potential

$$U = 2g(n_c + \tilde{n}), \tag{1.73}$$

with a particle-like local energy $\epsilon_p = p^2/2m + U(\mathbf{r},t)$. The second term containing the perturbative Hamiltonian $\hat{H}'$, describes inter-atomic collisions. As Kirkpatrick and Dorfman showed, this term can be reduced to binary collision integrals [72]. The final expression for the time evolution of the thermal distribution function then becomes

$$\frac{\partial f(\mathbf{r},\mathbf{p},t)}{\partial t} + \frac{\mathbf{p}}{m}\cdot\nabla_{\mathbf{r}} f(\mathbf{r},\mathbf{p},t) - \nabla U\cdot\nabla_{\mathbf{p}} f(\mathbf{r},\mathbf{p},t) = C_{12}[f,\Phi] + C_{22}[f]. \tag{1.74}$$

with $\nabla_{\mathbf{r}}$, $\nabla_{\mathbf{p}}$ representing the three-dimensional derivatives with respect to space and momentum. This is the so-called quantum Boltzmann equation, where $C_{12}[f,\Phi]$ describes collisions involving a condensate atom. This results either in an atom leaving the condensate or an atom scattering into the condensate. Both events change the number of condensate and thermal atoms. $C_{22}[f]$ on the other hand describes collisions between thermal atoms only. $C_{22}[f]$ and $C_{12}[f,\Phi]$ take the form

$$\begin{aligned}C_{22}[f] =& \frac{2g^2}{(2\pi)^5\hbar^7}\int d\mathbf{p}_2\int d\mathbf{p}_3\int d\mathbf{p}_4\,\delta(\mathbf{p}+\mathbf{p}_2-\mathbf{p}_3-\mathbf{p}_4)\\ &\cdot\delta(\tilde{\epsilon}_p+\tilde{\epsilon}_{p2}-\tilde{\epsilon}_{p3}-\tilde{\epsilon}_{p4})\\ &\cdot[(1+f)(1+f_2)f_3f_4 - ff_2(1+f_3)(1+f_4)]\end{aligned} \tag{1.75}$$

and

$$\begin{aligned}C_{12}[f,\Phi] =& \frac{2g^2 n_c}{(2\pi)^2\hbar^4}\int d\mathbf{p}_1\int d\mathbf{p}_2\int d\mathbf{p}_3\,\delta(m\mathbf{v}_c+\mathbf{p}_1-\mathbf{p}_2-\mathbf{p}_3)\\ &\cdot\delta(\epsilon_c+\tilde{\epsilon}_{p1}-\tilde{\epsilon}_{p2}-\tilde{\epsilon}_{p3})\\ &\cdot[\delta(\mathbf{p}-\mathbf{p}_2)-\delta(\mathbf{p}-\mathbf{p}_3)-\delta(\mathbf{p}-\mathbf{p}_4)]\\ &\cdot[(1+f_1)f_2f_3 - f_1(1+f_2)(1+f_3)],\end{aligned} \tag{1.76}$$

with $f \equiv f(\mathbf{p},\mathbf{r},t)$ and $f_i \equiv f(\mathbf{p}_i,\mathbf{r},t)$. Delta functions appearing in these integrals ensure energy and momentum conservation for the scattering events, where the energy of the thermal atoms is given by the Hartree-Fock energy $\tilde{\epsilon}_p = p^2/2m + 2g(n_c + \tilde{n})$ and the energy of the condensate is $\epsilon_c = \mu_c + mv_c^2/2$. The terms $(f_i + 1)$ and f_i take quantum statistics into account for the creation and annihilation of a boson with momentum $\mathbf{p}_i$. In the classical limit where occupation numbers are small (i.e. $f(\mathbf{p},\mathbf{r},t) \ll 1$) the term $[(1+f)(1+f_2)f_3f_4 - ff_2(1+f_3)(1+f_4)]$ in Eq. (1.75) reduces to $f_3f_4 - ff_2$ which yields an expression for the collision integral of a classical Boltzmann gas.

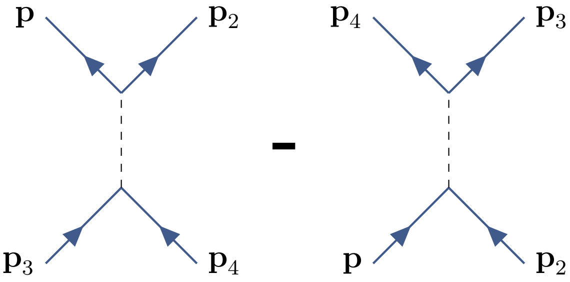

Figure 1.2 – Illustration of scattering events described by the C_{22} collision integral. Blue arrows stand for thermal particles and dashed lines for binary collisions. The C_{22} term consists of an integral over all possible scattering processes, which create an atom with momentum $\mathbf{p}$ minus an integral over all possible scattering events which annihilate an atom with momentum $\mathbf{p}$. Therefore $d\mathbf{p}d\mathbf{r}/(2\pi\hbar)^3 \cdot C_{22}[f(\mathbf{p},\mathbf{r},t)]$ gives the net-transfer of particles in an infinitesimal phase-space volume $d\mathbf{p}d\mathbf{r}/(2\pi\hbar)^3$ at $\mathbf{r}$ and $\mathbf{p}$.

The collision term $C_{22}[f(\mathbf{p},\mathbf{r},t)]$ describes a change in the distribution $f(\mathbf{p},\mathbf{r},t)$ due to scattering events between two thermal atoms. It therefore consists of an integral over all possible, binary scattering events, which create an atom with momentum $\mathbf{p}$ at position $\mathbf{r}$, minus an integral over all possible, binary scattering events which annihilate an atom with momentum $\mathbf{p}$ at position $\mathbf{r}$. This is illustrated in Fig. 1.2. It follows from Eq. (1.71) that $d\mathbf{p}d\mathbf{r}/(2\pi\hbar)^3 \cdot C_{22}[f(\mathbf{r},\mathbf{p},t)]$ describes the net-transfer of thermal particles into or out of an infinitesimal phase-space volume at momentum $\mathbf{p}$ and position $\mathbf{r}$. Similar considerations for the C_{12} collision integral show that $d\mathbf{p}d\mathbf{r}/(2\pi\hbar)^3 \cdot C_{12}$ describes the particle net-transfer between the condensate and the thermal cloud, illustrated in Fig. 1.3.

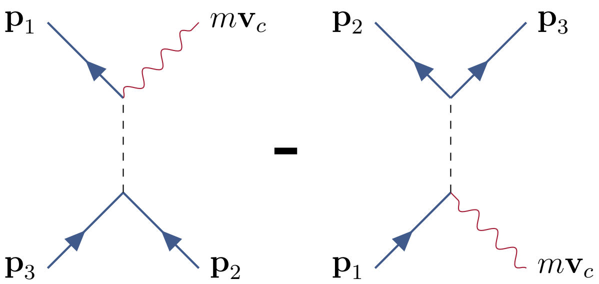

Figure 1.3 – Illustration of scattering events described by the C_{12} collision integral. Blue arrows stand for thermal particles, dashed lines for binary collisions and red wiggly lines are condensate atoms. The C_{12} term consists of an integral over all possible scattering processes, which create a condensate atom minus an integral over all possible scattering events which annihilate a condensate atom. Therefore $d\mathbf{p}d\mathbf{r}/(2\pi\hbar)^3 \cdot C_{12}$ gives the net-transfer of particles into or out of the condensate in an infinitesimal phase-space volume $d\mathbf{p}d\mathbf{r}/(2\pi\hbar)^3$ at $\mathbf{r}$ and $\mathbf{p}$.

1.5 The ZNG formalism

In the ZNG formalism the generalized GPE (1.59) and the quantum Boltzmann equation (1.74) are combined to form a coupled set of equations, which describe the condensate and thermal cloud time evolution

$$i\hbar\frac{\partial\Phi}{\partial t} = \left[-\frac{\hbar^2}{2m}\nabla^2 + V_{\text{ext}}(\mathbf{r},t) + gn_c(\mathbf{r},t) + 2g\tilde{n}(\mathbf{r},t) - iR(\mathbf{r},t)\right]\Phi \quad (1.77)$$

$$\frac{\partial f(\mathbf{r},\mathbf{p},t)}{\partial t} + \frac{\mathbf{p}}{m}\cdot\nabla_{\mathbf{r}} f(\mathbf{r},\mathbf{p},t) - \nabla U \cdot \nabla_{\mathbf{p}} f(\mathbf{r},\mathbf{p},t) = C_{12}[f,\Phi] + C_{22}[f]. \quad (1.78)$$

The coupling arises due to the mean-field potential containing the thermal and condensate density and the source term $-iR(\mathbf{r},t)$, which is consistently connected to the $C_{12}[f,\Phi]$ collision integral

$$R(\mathbf{r},t) = \frac{\hbar\Gamma_{12}[f,\Phi]}{2n_c(\mathbf{r},t)}, \quad (1.79)$$

with

$$\Gamma_{12}[f,\Phi] = \int \frac{d\mathbf{p}}{(2\pi\hbar)^3} C_{12}[f,\Phi]. \quad (1.80)$$

These equations may be solved numerically and with their help various physical phenomena, which arise due to the interaction between a thermal cloud and a condensate, can be described. Examples for these phenomena are the damping of collective modes [91–93], dark soliton dynamics at finite temperature [94, 95] and the decay of vortices [96–98].

How these coupled equations can be solved for the time-dependent case is thoroughly discussed in chapter 2. However, for a static distribution function $f(\mathbf{p},\mathbf{r})$, i.e. in thermal equilibrium, Eq. (1.77) and Eq. (1.78) may be further simplified, making it possible to derive an analytical expression for the thermal and condensate density. This is of special interest because an equilibrium state is the starting point of every dynamical simulation in this work.

1.5.1 Thermal equilibrium

In thermal equilibrium the source term $-iR(\mathbf{r},t)$ vanishes. Otherwise, there would be a net-transfer of particles into or out of the condensate, which is obviously a contradiction to the assumption of a gas in equilibrium. Therefore the equation describing the condensate becomes

$$\left[-\frac{\hbar^2}{2m}\nabla^2 + V_{\text{ext}}(\mathbf{r}) + g n_{c0}(\mathbf{r}) + 2g\tilde{n}_0(\mathbf{r})\right]\Phi_0(\mathbf{r}) = \epsilon_{c0}\Phi_0(\mathbf{r}), \tag{1.81}$$

where the index 0 denotes quantities in thermal equilibrium. The time evolution of the condensate wavefunction is now given by

$$\Phi_0(\mathbf{r},t) = \Phi_0(\mathbf{r})e^{-i\epsilon_{c0}t/\hbar} = \sqrt{n_{c0}(\mathbf{r})}e^{-i\epsilon_{c0}t/\hbar}. \tag{1.82}$$

Substituting Eq. (1.82) into Eq. (1.81) gives an expression for the energy of the condensate

$$\epsilon_{c0} = -\frac{\hbar^2\nabla^2\sqrt{n_{c0}(\mathbf{r})}}{2m\sqrt{n_{c0}(\mathbf{r})}} + V_{\text{ext}}(\mathbf{r}) + g n_{c0}(\mathbf{r}) + 2g\tilde{n}_0(\mathbf{r}). \tag{1.83}$$

In equilibrium the distribution function for the thermal particles is given by the Bose-Einstein distribution function $f^0(\mathbf{p},\mathbf{r})$. Describing the thermal particle energy by a single-particle Hartee-Fock spectrum leads to

$$f^0(\mathbf{p},\mathbf{r}) = \frac{1}{e^{\beta_0[p^2/2m+U_0(\mathbf{r})-\tilde{\mu}_0]} - 1}, \tag{1.84}$$

where $\tilde{\mu}_0$ is the chemical potential of the thermal cloud and $\beta_0 = 1/k_{\text{B}}T_0$ for an equilibrium gas at temperature T_0. The potential $U_0(\mathbf{r})$ consists of the Hartree-Fock mean-field and the trapping potential

$$U_0(\mathbf{r}) = V_{\text{ext}}(\mathbf{r}) + 2g[n_{c0}(\mathbf{r}) + \tilde{n}_0(\mathbf{r})]. \tag{1.85}$$

By inserting the distribution function from Eq. (1.84) into the C_{22} collision integral, one may show that [79]

$$C_{22}[f^0] = 0. \tag{1.86}$$

Therefore C_{22} collisions have no effect on the distribution function, which is convenient for a gas in equilibrium. However, if the Bose-Einstein distribution in Eq. (1.84) is inserted into Eq. (1.76) in order to calculate C_{12} collisions in equilibrium, one finds

$$\begin{aligned} C_{12}[f^0,\Phi] = \frac{2g^2 n_c}{(2\pi)^2\hbar^4} &\int d\mathbf{p}_1 \int d\mathbf{p}_2 \int d\mathbf{p}_3\, \delta(m\mathbf{v}_c + \mathbf{p}_1 - \mathbf{p}_2 - \mathbf{p}_3) \\ &\cdot \delta(\epsilon_c + \tilde{\epsilon}_{p1} - \tilde{\epsilon}_{p2} - \tilde{\epsilon}_{p3})(1 + f_1^0) f_2^0 f_3^0 \\ &\cdot [e^{\beta(\epsilon_{c0} - \tilde{\mu})} - 1]. \end{aligned} \tag{1.87}$$

This expression is not necessarily zero. The initial assumption that the source term $-iR(\mathbf{r},t)$ vanishes, i.e. that the C_{12} collision integral is equal to zero, holds only true for every equilibrium configuration if

$$\epsilon_{c0} = \tilde{\mu}_0. \tag{1.88}$$

That means that the chemical potential of the thermal cloud must be the same as the chemical potential of the condensate, to prevent a particle transfer between the two regions.

Using assumption Eq. (1.88) and integrating Eq. (1.84) over momentum space, an expression for the thermal cloud density can be obtained

$$\tilde{n}_0(\mathbf{r}) = \int \frac{d\mathbf{p}}{(2\pi\hbar)^3} f^0(\mathbf{p},\mathbf{r}) = \frac{1}{\Lambda^3} g_{3/2}(z_0(\mathbf{r})), \tag{1.89}$$

with the thermal de Broglie wavelength $\Lambda = (2\pi\hbar^2\beta_0/m)^{1/2}$, the Bose-Einstein function $g_{3/2}(z)$ and the fugacity $z_0(\mathbf{r})$ defined as

$$z_0(\mathbf{r}) = e^{\beta_0[\epsilon_{c0} - U_0(\mathbf{r})]}. \tag{1.90}$$

In the Thomas-Fermi approximation it is also possible to derive an analytical expression for the condensate density, which takes the form

$$n_{c0} = \frac{1}{g}[\epsilon_{c0} - V_{\text{ext}}(\mathbf{r}) - 2g\tilde{n}_0(\mathbf{r})] \geq 0. \tag{1.91}$$

Equations (1.89) and (1.81) will be subsequently used to create starting states for the dynamical simulations of a Bose gas. These starting states will be iterated in time using Eq. (1.77) and Eq. (1.78).

Chapter 2

Implementation

As outlined in the previous chapter the condensate and the thermal region are treated very differently in the ZNG approximation. The generalized GPE which describes the condensate time evolution has the form of a non-linear Schrödinger equation, whereas the evolution of the distribution function for the thermal excitations is a six-dimensional partial integro-differential equation. Therefore the mathematical methods used to solve these equations differ significantly, and the self-consistent coupling between both regions is a numerical challenge. The method presented in this chapter uses adaptive Cartesian collision bins, which allows for simulations in arbitrary trap geometries (previous implementations employed radial symmetry [98]). In addition a possible way to parallelize the implementation is shown and an analysis of the run time for a single time step of the algorithm is presented.

This chapter starts by discussing equilibrium solutions which are obtained by solving time-independent coupled equations (Eq. (1.81) and Eq. (1.89)). It proceeds by looking at the collisionless motion of the condensate, which is evolved in time using a split-step method. The quantum Boltzmann equation is solved using a Direct Simulation Monte Carlo (DSMC) approach [99–103], where test particles in phase-space model the evolution of the distribution function in time. The thermal cloud density, which is needed for the thermal cloud and the condensate time evolution is calculated with the help of a cloud-in-cell method, combined with a convolution of the resulting particle histogram with a sampling function. This results in a smooth density function which minimizes the effects of single test particle fluctuations.

To calculate the full dynamics of the system the collision integrals are solved in a stochastic manner by assigning collision probabilities to every test particle. To achieve this, the test particles have to be binned in position and momentum space. An adaptive-binning scheme for regions with a high number of test particles is presented and parallelization of the code is discussed. The chapter ends by showing test simulations for the ZNG implementation for an equilibrium and non-equilibrium initial state, to check the basic functionality of the code.

2.1 Equilibrium solutions

Although the main interest of this work is the study of dynamical systems far from equilibrium, it is also worth looking at time-independent solutions. On the one hand this shows the effect of the mean-field terms appearing in Eq. (1.77) and on the other hand the equilibrium solution can be used as an initial state for a dynamical simulation, in which the initial state is driven away from equilibrium by the simulated potential. To achieve thermal equilibrium, Eq. (1.81) and Eq. (1.89)

$$\left[-\frac{\hbar^2}{2m}\nabla^2 + V_{\text{ext}}(\mathbf{r}) + gn_{c0}(\mathbf{r}) + 2g\tilde{n}_0(\mathbf{r})\right]\Phi_0(\mathbf{r}) = \epsilon_{c0}\Phi_0(\mathbf{r}) \tag{2.1}$$

$$\tilde{n}_0(\mathbf{r}) = \int \frac{d\mathbf{p}}{(2\pi\hbar)^3} f^0(\mathbf{p},\mathbf{r}) = \frac{1}{\Lambda^3} g_{3/2}(z_0(\mathbf{r})) \tag{2.2}$$

have to be solved in a self-consistent manner. Therefore one has to explicitly set the chemical potential of the ground state ϵ_{c0} equal to the chemical potential of the thermal cloud $\tilde{\mu}_0$ (which appears in the local fugacity $z_0(\mathbf{r}) = e^{\beta_0[\tilde{\mu}_0 - U_0(\mathbf{r})]}$)

$$\mu_0 \equiv \tilde{\mu}_0 = \epsilon_{c0}, \tag{2.3}$$

as discussed in section 1.5.1.

The approach to numerically calculate the equilibrium state of a system with a given temperature T, total particle number N, scattering length a and trap frequencies $\omega_{i=x,y,z}$ proceeds as follows [104]: the starting point is a Gaussian wavefunction, that is normalized to an estimated number of condensate atoms N_{c0}, defining a condensate density via $n_{c0}(\mathbf{r}) = |\Phi_0(\mathbf{r})|^2$. The thermal density is set to zero $\tilde{n}_0 = 0$. The wavefunction (2.1) is then iterated for one small time step Δt in imaginary time, as described in section 2.1.1. Using the calculated values for the chemical potential μ_0 and the condensate density $n_{c0}(\mathbf{r}) = |\Phi_0(\mathbf{r})|^2$, a thermal cloud density $\tilde{n}_0$ can be calculated with Eq. (2.2). With the help of the thermal density the atom number in the thermal cloud can be calculated $\tilde{N}_0 = \int d\mathbf{r}\tilde{n}_0(\mathbf{r})$ and a new condensate atom number is obtained by $N_{c0} = N_0 - \tilde{N}_0$. The wavefunction is then renormalized to the new condensate atom number N_{c0}. With new values for $\Phi_0(\mathbf{r})$, $n_{c0}(\mathbf{r}) = |\Phi_0(\mathbf{r})|^2$ and $\tilde{n}_0(\mathbf{r})$, the wavefunction is again iterated in imaginary time and the algorithm repeats, until the chemical potential μ_0 remains constant between two time steps, up to a chosen precision. Algorithm 1 in Appendix B gives a pseudo-code version of this equilibrium solver.

The presented algorithm assumes that the chemical potential always lies below the effective potential U_0 of the thermal cloud. Otherwise the Bose-Einstein function $g_{3/2}(z_0(\mathbf{r}))$ in Eq. (2.2) would diverge. However, there is no reason why this should be the case in a simulation. Especially for relatively warm clouds close to T_c or highly anisotropic traps it is possible that $U_0(\mathbf{r}) < \mu_0$. In that cases μ_0 has to be set artificially to the minimum of $U_0(\mathbf{r})$ in regions where $U_0(\mathbf{r})$ is below μ_0.

2.1.1 Solving the time-independent GPE

In order to solve the time-independent equation (2.1) it is useful to look at the time-dependent equation (1.77) in imaginary time [105]. In this case, the time t is substituted using a so-called Wick rotation of the form [106]

$$t \longrightarrow t' = it. \tag{2.4}$$

With that transformation Eq. (1.22) becomes a diffusion equation

$$-\hbar\frac{\partial\Phi(\mathbf{r},t')}{\partial t'} = \left[-\frac{\hbar^2}{2m}\nabla^2 + V_{\text{ext}}(\mathbf{r}) + gn_c(\mathbf{r},t')\right]\Phi(\mathbf{r},t') \tag{2.5}$$

and the time evolution of a given wavefunction $\Phi(\mathbf{r})$ takes the form

$$\Phi(\mathbf{r},t') = \sum_{n=0}^{\infty} c_n e^{-E_n t'/\hbar}\varphi_n(x,0). \tag{2.6}$$

Here φ_n are the sorted energy eigenstates of the system with the corresponding eigenvalues E_n, which fulfill the relation $E_n < E_{n+1}\ \forall n \in \mathbb{N}$. Hence φ_0 is the ground state with energy E_0.

From Eq. (2.6) one can see that the Eigenfunctions φ_n for a given state are damped out when evolved in time. The higher the eigenenergy of the state the higher the damping rate. Hence states with higher energy are damped out more rapidly compared with states with lower energy. The implemented algorithm to compute the ground state of the system takes advantage of this effect by iterating the wavefunction in imaginary time using Eq. (2.5) and renormalizing the wavefunction after each time step. With every time step the contribution of the ground state to the wavefunction gets more pronounced, while the contributions of higher states diminish. For an infinite number of small time steps this leads to the ground state of the system.

The procedure for finding the ground-state solution at $T = 0$ starts with an arbitrary wavefunction and iterates this wavefunction in imaginary time using Eq. (2.5). This can be done using the Crank-Nicholson or a split-step method. It is common to take the analytical ground state for the case of vanishing interactions as an initial state. The time evolution does not conserve the norm of the wavefunction and it is renormalized to the particle number after each step. As described previously the algorithm remains the same for the finite temperature case, but it takes the additional mean-field potential of the thermal cloud into account, which is updated after each time step, and the particle number of the condensate changes during the simulation.

2.1.2 Example for an isotropic trap

A solution of the equilibrium solver for an isotropic trap ($\omega = \omega_x = \omega_y = \omega_z$) is presented in Fig. 2.1. The left picture shows the condensate density and the right picture shows the thermal cloud density in the x-z-plane. The trap frequency is $\omega = 2\pi \times 120\,\mathrm{rad\,s^{-1}}$ with a total number of $N = 5 \times 10^4$ ^{87}Rb atoms at a temperature $T = 150\,\mathrm{nK}$. This leads to a final state with 16735 atoms in the condensate and 33265 thermal atoms.

The resulting shape of the condensate and thermal cloud density is typical for self-consistent Hartree-Fock calculations [107]. Thermal atoms are depleted from the trap center because of the very high condensate density, which appears in the mean-field potential term (Eq. (1.85)) and it is highest in the region where the condensate vanishes. Figure 2.2 shows the thermal cloud (golden curve), condensate (red curve) and total density (black curve) as a function of the distance r from the trap center after the algorithm has converged. The condensate density takes a nearly parabolic profile, with the kinetic term contributing to prevent a sudden drop to zero at the edges. Together with the thermal cloud, which is suppressed in the region of high condensate densities, it forms a smooth total density profile. The depletion of the thermal cloud can be understood by looking at the resulting potential of the condensate and thermal atoms in Fig. 2.3. Compared with the mean-field potential for the condensate the thermal atom effective potential $U(\mathbf{r})$, defined in Eq. (1.73), has an additional factor of gn_c. Therefore instead of a flat bottomed potential thermal atoms see a repulsive potential in the trap center, which has a minimum where the condensate density goes to zero. As mentioned in Sec. 2.1 if the chemical potential μ_{c0} is higher than $U(\mathbf{r})$, it has to be artificially set equal to the minimum of $U(\mathbf{r})$. As shown in Fig. 2.3 this is already the case for the considered configuration. For lower temperatures the minimum of $U(\mathbf{r})$ would lie above the chemical potential.

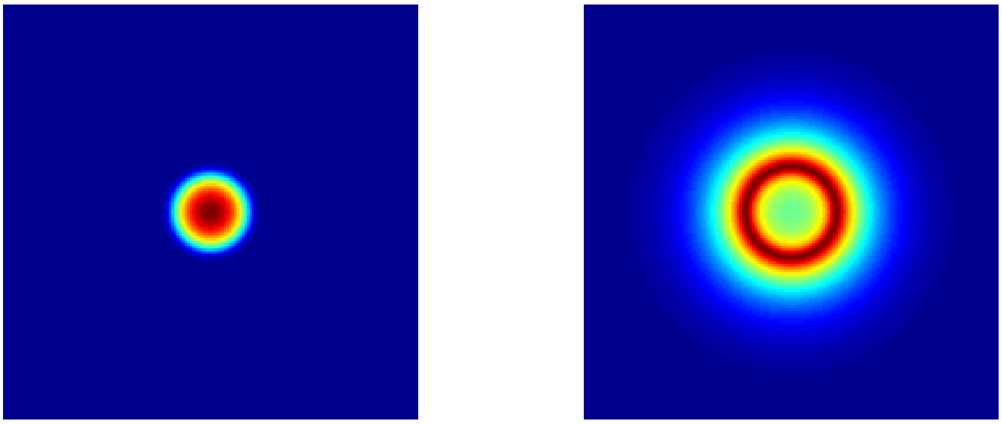

Figure 2.1 – Condensate (left) and thermal cloud density (right) in the x-z-plane for an equilibrium state of $N = 5 \times 10^4$ ^{87}Rb atoms at $T = 150\,\mathrm{nK}$ in a trap with angular frequency $\omega = 2\pi \times 120\,\mathrm{rad\,s}^{-1}$. Red color denotes regions of high, blue color regions of low densities. The scales for the two pictures are different, in order to show the curvature of the thermal cloud density, which is about an order of magnitude smaller then the condensate density.

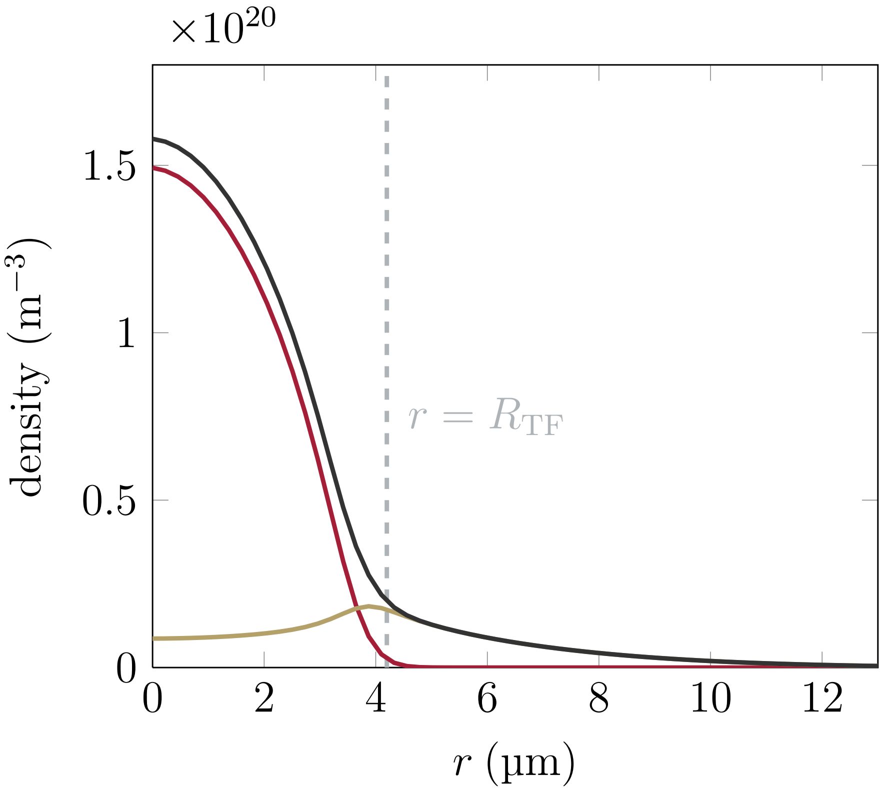

Figure 2.2 – Condensate (red curve), thermal cloud (golden curve) and total density (black curve) for the equilibrium state in Fig 2.1 for different distances r from the trap center. The gray dashed line shows the calculated Thomas-Fermi radius R_{TF} for 16735 ^{87}Rb atoms in the condensate at $T = 0$.

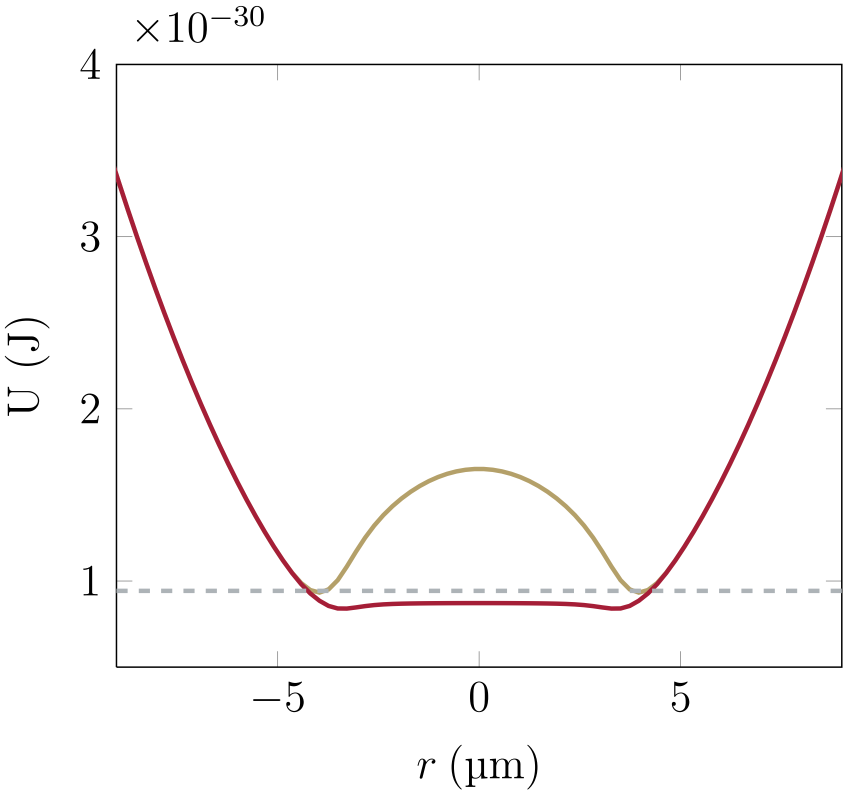

Figure 2.3 – Effective potential $U(r)$ seen by the thermal cloud (golden curve) and the condensate (red line) as a function of the distance r to the trap center. The gray dashed line shows the chemical potential μ_{c0}. The ground state density in the middle of the trap, which creates a flat-bottomed potential for the condensate, leads to a highly repulsive potential for the thermal atoms.

2.2 Collisionless time evolution

If the typical time scale τ for a collision to happen is much higher than the small time step Δt, with which the system is numerically iterated in time, collisions may be separated from the residual dynamics of the system. It is therefore convenient to first iterate the coupled ZNG equations in time with $C_{12} = C_{22} = 0$ and deal with collisions later. The numerical problem is then two-fold. First the generalized GPE (1.77) has to be iterated in time, followed by an iteration of the quantum Boltzmann equation (1.78) without collisions.

2.2.1 Solving the generalized GPE

In principal every numerical method which can be applied to the GPE can also be used to solve the generalized GPE. However, because of the additional mean-field potential coming from the thermal cloud and the source-term $R(\mathbf{r},t)$, a very stable numerical algorithm is needed. Therefore a split-step method [108, 109], that takes the potential of the previous time step into account, is used. This method can be derived using the formal time evolution of a state $|\Phi(\mathbf{r},t)\rangle$

$$|\Phi(t+\Delta t)\rangle = \hat{U}(t+\Delta t,t)\,|\Phi(t)\rangle\,. \tag{2.7}$$

In the general case, where the Hamiltonian is time-dependent, the time evolution operator depends on the time t as well as the time difference Δt and can be written in the form [110]

$$\hat{U}(t+\Delta t,t) = 1 + \frac{1}{i\hbar}\int_t^{t+\Delta t} dt'\hat{H}(t') - \frac{1}{\hbar^2}\int_t^{t+\Delta t} dt' \int_t^{t'} dt''\hat{H}(t')\hat{H}(t'') + \ldots. \tag{2.8}$$

Substituting $\hat{H}(t')$ by its Taylor expansion around time t

$$\hat{H}(t') = \hat{H}(t) + \frac{d\hat{H}(t)}{dt}\cdot(t'-t) + \frac{1}{2}\frac{d^2\hat{H}(t)}{dt^2}\cdot(t'-t)^2 + \ldots \tag{2.9}$$

$$\equiv \hat{\alpha} + \hat{\beta}(t'-t) + \frac{1}{2}\hat{\gamma}(t'-t)^2\ldots, \tag{2.10}$$

with $\hat{\alpha} = \hat{H}(t)$, $\hat{\beta} = \frac{d\hat{H}(t)}{dt}$ and $\hat{\gamma} = \frac{d^2\hat{H}(t)}{dt^2}$ gives

$$\hat{U}(t+\Delta t,t) = 1 + \frac{\hat{\alpha}}{i\hbar}\Delta t + \frac{\hat{\beta}}{2i\hbar}\Delta t^2 - \frac{\hat{\alpha}^2}{2\hbar^2}\Delta t^2 + \mathcal{O}(\Delta t^3). \tag{2.11}$$

Up to the first order this expression is identical to the exponential series

$$e^{-i\hat{H}(t)\Delta t/\hbar} = 1 + \frac{\hat{\alpha}}{i\hbar}\Delta t + \mathcal{O}(\Delta t^2), \tag{2.12}$$

which would be an exact description of the time evolution in the case of a non-time-dependent Hamilton operator.

In the time-dependent case approximating $\hat{U}(t+\Delta t,t)$ by this series yields an error of the order of $\mathcal{O}(\Delta t^2)$. To get a higher precision, one can use Eq. (2.11) to derive an exponential function, whose series is identical to $\hat{U}(t+\Delta t,t)$ up to the third order

$$\hat{U}(t+\Delta t,t) \simeq e^{-i(\hat{\alpha}+\frac{1}{2}\hat{\beta}\Delta t)\Delta t/\hbar} + \mathcal{O}(\Delta t^3). \tag{2.13}$$

In addition one may approximate $\hat{\beta}$ by a backward-difference method

$$\hat{\beta} \simeq \frac{\hat{H}(t) - \hat{H}(t-\Delta t)}{\Delta t} + \mathcal{O}(\Delta t). \tag{2.14}$$

Because this approximation yields an error of $\mathcal{O}(\Delta t)$ and $\hat{\beta}$ is multiplied by Δt^2 in Eq. (2.13), this replacement still has an error of order $\mathcal{O}(\Delta t^3)$. Substituting Eq. (2.14) into Eq. (2.13) and considering the fact that the kinetic operator $\hat{T}$ is not time dependent, one finds the final form for the evolution operator

$$U(t+\Delta t,t) \simeq e^{-i\tilde{H}(t)\Delta t/\hbar} + \mathcal{O}(\Delta t^3), \tag{2.15}$$

with $\tilde{H}(t)$ consisting of a kinetic operator $\hat{T}$ and a mixed potential operator $\tilde{V}(t) \equiv \frac{1}{2}\left[3\hat{V}(t) - \hat{V}(t-\Delta t)\right]$

$$\tilde{H} = \hat{T} + \tilde{V}(t) = \hat{T} + \frac{1}{2}\left[3\hat{V}(t) - \hat{V}(t-\Delta t)\right]. \tag{2.16}$$

This mixed potential can be thought of as a linear extrapolation of the potential to the mid-time point $t + \Delta t/2$. To calculate it one only needs to store the potential of the previous time step to win a higher accuracy for the time evolution.

Applying a so-called Strang-splitting approach [111–113], which can be derived using the formula of Baker-Campbell-Hausdorff [114, 115], to the operator defined in Eq. (2.15), leads to

$$e^{-i\tilde{H}(t)\Delta t/\hbar} = e^{-i\tilde{V}(t)\Delta t/2\hbar} e^{-i\hat{T}\Delta t/\hbar} e^{-i\tilde{V}(t)\Delta t/2\hbar} + \mathcal{O}(\Delta t^3), \tag{2.17}$$

so the numerical splitting procedure has the same error as the approximations made in Eq. (2.13).

The time evolution of a state $|\Psi(t)\rangle$ is then given by

$$|\Psi(t+\Delta t)\rangle = e^{-i\tilde{V}(t)\Delta t/2\hbar} e^{-i\hat{T}\Delta t/\hbar} e^{-i\tilde{V}(t)\Delta t/2\hbar} |\Psi(t)\rangle \,. \tag{2.18}$$

The advantage of this splitting method is that the action of the potential term $e^{-i\tilde{V}(t)\Delta t/2\hbar}$ is just a point-wise multiplication when applied to a wavefunction in position-space. On the other hand the action of the kinetic term $e^{-i\hat{T}\Delta t/\hbar}$ is a point-wise multiplication in k-space. After discretizing the wavefunction (i.e. calculating the wavefunction only at specific supporting points with separations Δx,Δy and Δz in the x-,y- and z-direction and iterating it only for small steps Δt) the pseudo-spectral method works as follows: first the product of the potential term and the wavefunction is calculated in position space and the result is transformed into momentum-space using a discrete Fourier transformation. Then the kinetic term is applied and the wavefunction is transformed back into position-space where the multiplication with the last potential term can be calculated. Because the discrete Fourier transformation, which scales with $\mathcal{O}(N\log(N))$, can be calculated with the so-called FFTW package [116] the discussed method is an efficient way to solve the generalized GPE.

2.2.2 Solving the quantum Boltzmann equation

The fact that the quantum Boltzmann equation (1.74) is a six-dimensional non-linear partial integro-differential equation makes a direct time integration difficult. Therefore it is often solved by a Direct-Simulation-Monte Carlo (DSMC) [103] method as first outlined by Bird [99]. In this approach the distribution function is sampled by a large number of phase-space points. The time evolution of these phase-space points, which are often referred to as "test particles" [117], then yields the time evolution of the distribution function.

The correspondence between the test particles and the physical properties of the system is given by the relation

$$f(\mathbf{p},\mathbf{r},t) \simeq \gamma(2\pi\hbar)^3 \sum_{i=1}^{\tilde{N}_{\mathrm{tp}}} \delta(\mathbf{r}-\mathbf{r}_i(t))\delta(\mathbf{p}-\mathbf{p}_i(t)), \tag{2.19}$$

where $\mathbf{r}_i(t)$ is the position and $\mathbf{p}_i(t)$ the momentum of test particle i. The weighting factor $\gamma = \tilde{N}/\tilde{N}_{\mathrm{tp}}$ is given by the relation between physical thermal particles $\tilde{N}$ and test particles $\tilde{N}_{\mathrm{tp}}$. The number of test particles is chosen so that the continuous distribution function $f(\mathbf{p},\mathbf{r},t)$ is represented in an appropriate way, i.e. that test particles, although they are discrete, form a quasi-continuous distribution. Hence the number of test particles is not necessarily equal to the number of thermal particles, and most of the time it will be much greater in a simulation of an ultra-cold atom cloud. The phase-space distribution is normalized to the number of thermal particles $\tilde{N}$, so that

$$\tilde{N}(t) = \int d\mathbf{r} d\mathbf{p} f(\mathbf{p},\mathbf{r},t)/(2\pi\hbar)^3. \tag{2.20}$$

The test particles evolve in time like classical particles in the Hartree-Fock potential $U(\mathbf{r},t)$

$$\frac{d\mathbf{r}}{dt} = \frac{\mathbf{p}_i(t)}{m} \tag{2.21}$$

$$\frac{d\mathbf{p}_i}{dt} = -\nabla U(\mathbf{r},t)\bigg|_{\mathbf{r}=\mathbf{r}_i}. \tag{2.22}$$

Together with Eq. (2.19) this gives the time evolution of the distribution function $f(\mathbf{p},\mathbf{r},t)$.

For the systems considered in this thesis it is necessary that the solver of Eq. (2.21) and Eq. (2.22) conserves energy. Failure to do so would, for example, result in a net transfer of particles between the condensate and the thermal region even for an equilibrium state, which is obviously unphysical. Hence classical Runge-Kutta methods are undesirable, whereas symplectic integrators [118–120], which are designed to solve Hamiltonian problems, conserve energy as well as phase-space volume. To derive an expression for a symplectic integrator it is useful to look at the evolution of the phase-space coordinate $\mathbf{z} = (\mathbf{p},\mathbf{r})$ for a classical particle with a system Hamiltonian $H = T + U$ in the Lie formalism

$$\frac{d\mathbf{z}}{dt} = \{\mathbf{z},H\} = -i\mathcal{L}\mathbf{z}, \tag{2.23}$$

where $\{\mathbf{z},H\}$ is the Poisson bracket of $\mathbf{z}$ and H defined as

$$\{f,g\} = \sum_i \left(\frac{\partial f}{\partial r_i}\frac{\partial g}{\partial p_i} - \frac{\partial f}{\partial p_i}\frac{\partial g}{\partial r_i} \right) \tag{2.24}$$

and $\mathcal{L}$ is referred to as the Liouville operator. The solution of Eq. (2.23) is given by

$$\mathbf{z}(t + \Delta t) = e^{-i\mathcal{L}\Delta t}\mathbf{z}(t). \tag{2.25}$$

Equivalent to the Strang-splitting approach made in Sec. 2.2.1, the Liouville operator can be split in a potential part $\mathcal{L}_U \equiv i\{\mathbf{z},U\}$ and a kinetic part $\mathcal{L}_T \equiv i\{\mathbf{z},T\}$. With the help of the Baker-Campbell-Hausdorff formula [114, 115] one may show that

$$e^{-i\mathcal{L}\Delta t} = e^{-i\mathcal{L}_T\Delta t/2} e^{-i\mathcal{L}_U\Delta t} e^{-i\mathcal{L}_T\Delta t/2} + \mathcal{O}(\Delta t^3). \tag{2.26}$$

This is the classical equivalent of Eq. (2.17). When used to solve Eq. (2.21) and Eq. (2.22) this method leads to a change in the test particles' positions and velocities. The kinetic term $\mathcal{L}_T$ is applied first, which results in

$$\tilde{\mathbf{r}}_i = \mathbf{r}_i(t) + \frac{1}{2}\mathbf{v}_i(t)\Delta t \tag{2.27}$$

then the potential term $\mathcal{L}_U$ updates the velocities

$$\mathbf{v}_i(t+\Delta t) = \mathbf{v}_i(t) - \frac{1}{m}\nabla U(\tilde{\mathbf{r}}_i)\Delta t \tag{2.28}$$

and the final position at $t + \Delta t$ can be calculated by applying $\mathcal{L}_U$ again with the updated values $\tilde{\mathbf{r}}_i$ and $\mathbf{v}_i(t + \Delta t)$

$$\mathbf{r}_i(t+\Delta t) = \tilde{\mathbf{r}}_i + \frac{1}{2}\mathbf{v}_i(t+\Delta t)\Delta t. \tag{2.29}$$

If the potential term U is explicitly time-dependent it is extrapolated to the midpoint $t + \Delta t/2$ of the interval, in analogue to Eq. (2.16)

$$\tilde{U} = \frac{1}{2}\left[3U(t) - U(t-\Delta t)\right]. \tag{2.30}$$

Algorithm 3 in Appendix B is a pseudo-code version of the time evolution of thermal particles.

2.2.3 Calculating the thermal cloud density

For calculating the mean-field potential of the thermal cloud and the condensate an expression for the thermal cloud density $\tilde{n}(\mathbf{r},t)$ is needed. However, from the discussion so far it is not obvious how this thermal density can be calculated. Using test particles to calculate the thermal density $\tilde{n}_{\mathrm{tp}}(\mathbf{r},t)$ would lead to

$$\tilde{n}_{\mathrm{tp}}(\mathbf{r},t) = \gamma \sum_{i=1}^{\tilde{N}_{\mathrm{tp}}} \delta\left[\mathbf{r} - \mathbf{r}_i(t)\right], \tag{2.31}$$

which cannot be used in a simulation. In order to calculate a force $F = -\nabla U(\mathbf{r},t)$ acting on the test particles in Eq. (2.28) the potential U in Eq. (1.73) has to be smooth and differentiable, which is clearly not the case for a sum over delta functions. A remedy for this problem is to take equation (2.31) and to broaden the delta functions, i.e. replacing them by a sampling function $S(\mathbf{r})$ with a small but finite width, which is still normalized to unity. This leads to a smoother thermal density $\tilde{n}$

$$\tilde{n}(\mathbf{r},t) = \gamma \sum_{i=1}^{\tilde{N}_{\mathrm{tp}}} S(\mathbf{r} - \mathbf{r}_i). \tag{2.32}$$

This can be calculated from Eq. (2.31) via a convolution

$$\tilde{n}(\mathbf{r},t) = (S * \tilde{n}_{\mathrm{tp}})(\mathbf{r}',t) \equiv \int d\mathbf{r}' S(\mathbf{r} - \mathbf{r}')\tilde{n}_{\mathrm{tp}}(\mathbf{r}',t). \tag{2.33}$$

A convenient choice for $S(\mathbf{r})$ is an isotropic Gaussian function of width η

$$S(\mathbf{r}) = (\pi\eta^2)^{-3/2} e^{-r^2/\eta^2}. \tag{2.34}$$

Although the replacement of the delta functions in Eq. (2.31) is a mathematical tool to get a smooth thermal density, it can be thought of as a replacement of the contact interaction by an interaction with a finite range. In addition simulation results are mostly insensitive to the actual width of $S(\mathbf{r})$, which was also outlined in former work [79].

A fast way to actually calculate the thermal density is to assign test particles to points on a 3D grid first. As the thermal density is also needed for the mean-field potential of the condensate, it is helpful to use the same discretization as for the pseudo-spectral method for the condensate wavefunction (see Sec. 2.2.1). To minimize sharp density fluctuations, a cloud-in-cell method is used [117]. In this method a particle, with position (x,y,z), is assigned to eight grid points instead of one, with weighting factors $\alpha_{x,y,z}$ and $\alpha^*_{x,y,z} = 1 - \alpha_{x,y,z}$ defined as

$$\alpha_x = (x - x_k)/(x_{k+1} - x_k) \tag{2.35}$$

$$\alpha_y = (y - y_l)/(y_{l+1} - y_l) \tag{2.36}$$

$$\alpha_z = (z - z_m)/(z_{m+1} - z_m), \tag{2.37}$$

with

$$x_k < x < x_{k+1} \tag{2.38}$$

$$y_l < y < y_{l+1} \tag{2.39}$$

$$z_m < z < z_{m+1}, \tag{2.40}$$

where x_k, y_l and z_m are grid points at position k, l and m in the x-,y- and z-direction. In order to assign test particles to multiple grid points, the two nearest grid points in each dimension ((x_k,x_{k+1}) in the x-, (y_l,y_{l+1}) in the y-, and (z_m,z_{m+1}) in the z-direction) have to be determined. The test particle contributes to each of them with the given weighting factors $\alpha_{x,y,z}$. This is illustrated in Fig. 2.4. Besides the fact that the calculated density is much smoother with this method, it also varies continuously in time when test particles move from one cell to another.

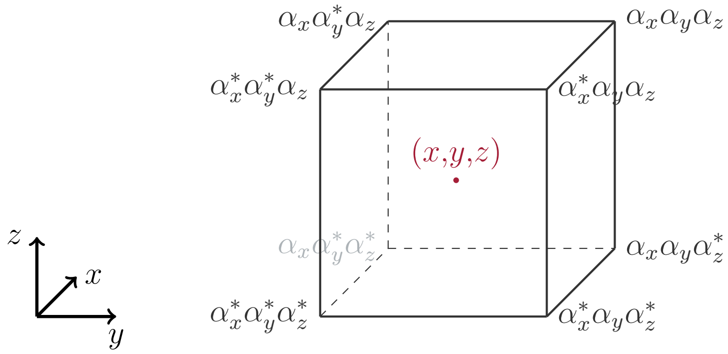

Figure 2.4 – Illustration of the cloud-in-cell method. A test particle with coordinates (x,y,z) is assigned to eight different grid points using the weighting factors α_i and $\alpha_i^* = 1 - \alpha_i$.

After calculating the distribution of test particles on the grid the smoothing operation can be applied. For that purpose the convolution theorem may be used

$$\mathcal{F}(f * g) = \mathcal{F}(f) \cdot \mathcal{F}(g), \tag{2.41}$$

which means that the Fourier transform of the convolution of two functions f and g (denoted by $\mathcal{F}(f * g)$) is equal to the product of each individual Fourier transform $\mathcal{F}(f)$ and $\mathcal{F}(g)$. Thus, one may again use a Fourier transform to calculate the thermal cloud density $\tilde{n}(\mathbf{r},t)$ in Eq. (2.33), which becomes

$$\tilde{n}(\mathbf{r},t) = \mathcal{F}^{-1}(\mathcal{F}(\tilde{n}_{\text{cc}}(\mathbf{r},t)) \cdot \mathcal{F}(S(\mathbf{r}))), \tag{2.42}$$

where $\tilde{n}_{\text{cc}}$ is the distribution obtained by the cloud-in-cell method and $\mathcal{F}^{-1}$ is the inverse Fourier transform. Because $S(\mathbf{r})$ is a Gaussian function, the Fourier transform $\mathcal{F}(S(\mathbf{r}))$ is also a Gaussian and can be calculated analytically. Therefore the only operations which are time consuming are the Fourier transform of the discrete function $\tilde{n}_{\text{cc}}$ and the inverse transform of the product

$\mathcal{F}(\tilde{n}_{cc}(\mathbf{r},t)) \cdot \mathcal{F}(S(\mathbf{r}))$. Again this was calculated using the FFTW package. A detailed description of the cloud-in-cell calculation and the smoothing operation is shown in algorithm 4 in Appendix B.

In Fig. 2.5 an example result for the cloud-in-cell method and the smoothing operation is shown. Although the cloud-in-cell method minimizes single test particle effects, the fluctuations in the resulting density are still large compared with the smoothed density, and would lead to high forces on test particles due to high potential gradients.

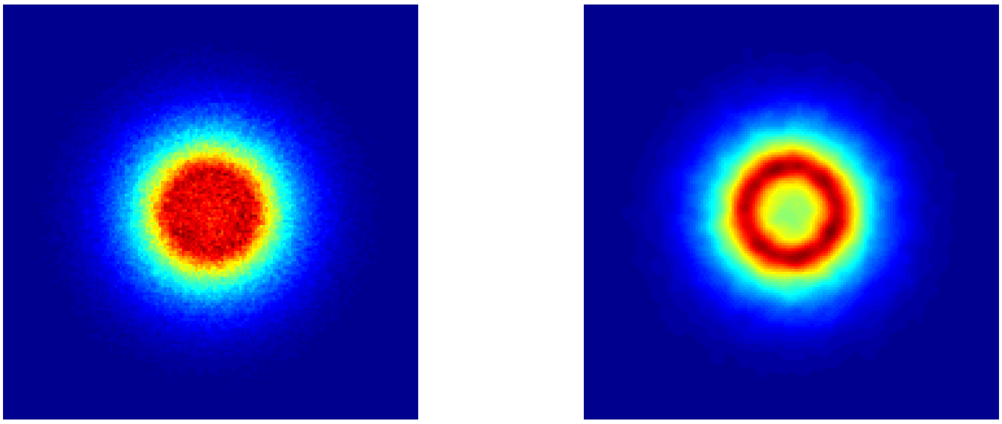

Figure 2.5 – Equilibrium thermal density for the state in Sec. 2.1.2, calculated using 10^6 test particles. Left picture shows the thermal density obtained by the cloud-in-cell method, right picture shows the thermal density after the smoothing operation. High density fluctuations in the non-smoothed case would lead to high forces on test particles.

2.2.4 Initial state

The starting point for a time-dependent simulation is often an equilibrium state. While the initial wavefunction can directly be calculated with the algorithm 1 outlined in Appendix B, one needs to assign initial velocities and positions to the test particles for the thermal cloud. In equilibrium the probability to find a particle with momentum $\mathbf{p}$ and position $\mathbf{r}$ is given by the Bose-Einstein distribution function $f(\mathbf{p},\mathbf{r})$. Thus, to set up an initial state, an algorithm to calculate random deviates following a given distribution function is required. An efficient mathematical tool to do so, is the so-called rejection method [121–123] which goes back to ideas of von Neumann in 1951 [124]. For a detailed discussion of the rejection method see Appendix A.1.

As the equilibrium distribution is a very smooth function, a rather simple form of the rejection method may be used, where the comparison function is a constant. First, particles are distributed in position-space following the density function $\tilde{n}(\mathbf{r})$, which is calculated with the Hartree-Fock equilibrium state code. To do so, three uniformly distributed, random numbers R_1,R_2 and R_3 with $R_1 \in [-x_{\max},x_{\max}]$, $R_2 \in [-y_{\max},y_{\max}]$ and $R_3 \in [-z_{\max},z_{\max}]$, are calculated, where $2x_{\max}$, $2y_{\max}$ and $2z_{\max}$ are the box sizes in the x-,y- and z- directions respectively. The three random values define the Cartesian coordinates of a uniformly distributed point $\mathbf{r}_{\text{rand}}$ in position-space

$$\mathbf{r}_{\text{rand}} = \begin{pmatrix} R_1 \\ R_2 \\ R_3 \end{pmatrix}. \tag{2.43}$$

As a constant comparison function the maximum of the thermal density $\tilde{n}_{\max}$ is chosen and another random deviate R_4 is selected so that $R_4 \in [0,\tilde{n}_{\max}]$. The random number R_4 is then compared with $\tilde{n}(\mathbf{r}_{\text{rand}})$. If $R_4 > \tilde{n}(\mathbf{r}_{\text{rand}})$ the position $\mathbf{r}_{\text{rand}}$ is rejected and a new set of random variables R_1, R_2, R_3 and R_4 is determined until $R_4 < \tilde{n}(\mathbf{r}_{\text{rand}})$. For $R_4 < \tilde{n}(\mathbf{r}_{\text{rand}})$ a test particles with position $\mathbf{r}_{\text{rand}}$ is created. The test particle's momentum is then determined in a similar way using the fact that the Bose-Einstein distribution is isotropic in momentum-space. The distribution function for the magnitude of the momentum, p, at position $\mathbf{r}_{\text{rand}}$ is obtained by integrating the distribution function $f(\mathbf{r}_{\text{rand}},\mathbf{p})$ over the azimuth and the elevation angle of the momentum vector

$$f(\mathbf{r}_{\text{rand}},p) = \int_0^{\pi} d\theta \int_0^{2\pi} d\phi\, p^2 \sin(\theta) f(\mathbf{r}_{\text{rand}},\mathbf{p}) = 4\pi p^2 f(\mathbf{r}_{\text{rand}},\mathbf{p}). \tag{2.44}$$

The magnitude of the momentum for a test particle at position $\mathbf{r}_{\text{rand}}$ is then determined in the following way: two random numbers $p_{\text{rand}} \in [0,p_{\max}]$, where $p_{\max}$ is the maximum momentum[1], and $R_5 \in [0,f_{\max}]$ are selected, where $f_{\max}$ denotes the maximum of the distribution function for the momentum magnitude. Using Eq. (2.44) $f_{\max}$ is calculated numerically for a given $\mathbf{r}_{\text{rand}}$. If $R_5 > f(\mathbf{r}_{\text{rand}},p_{\text{rand}})$ then p_{rand} is rejected and two new random variables are selected. However, if $R_5 < f(\mathbf{r}_{\text{rand}},p_{\text{rand}})$ two random angles $\phi \in [0,2\pi]$ and $\cos(\theta) \in [-1,1]$ are calculated, which together with p_{rand} define the test particle's momentum $\mathbf{p}_i$. Note that θ is determined using a uniformly random number in the interval $[-1,1]$, which represents $\cos(\theta)$, instead of using a uniformly distributed random angle $\theta \in [0,\pi]$. The latter would produce too many particles with a momentum vector around π and 0, instead of uniformly distributed momentum vectors.

---

[1] This was chosen to be three times the thermal velocity, $v_{\text{th}} = \sqrt{k_{\text{B}}T/m}$, of the initial state multiplied by the mass $p_{\max} = 3m\sqrt{k_{\text{B}}T/m}$. In a dynamical simulation $p_{\max}$ is adapted to the corresponding collision cell, see Sec. 2.3.

2.3 Collisions

The collisionless term of the quantum Boltzmann equation is solved by evolving the test particles' velocities and positions over time as described in the previous section. In this scheme collisions are separated from the residual motion consisting of the mean-field evolution of the condensate and the test particles. This is convenient as long as the Knudsen factor Kn, defined as the mean-free path of the particles divided by a characteristic length scale of the system [125], is higher or equal to approximately 0.1 (in harmonically trapped gases the characteristic length scale corresponds, for example, to the longest oscillator length). Although values of Kn ~ 0.01 have been observed in cold atom experiments, most experiments operate in a regime where Kn>1 [103]. Therefore the collision integrals can be solved after calculating the mean-field evolution of the test particles. This is done by a numerical Monte Carlo integration, which results in collision probabilities for each test particle. A test particle may then undergo a collision with another test particle or the condensate, leading to a sudden change in its momentum.

2.3.1 The C_{22} collision integral

The C_{22} collision integral describes collisions between thermal particles. Defining the "out"-collision rate C_{22}^{out} in this context as

$$\begin{aligned} C_{22}^{\text{out}}[f] = -\frac{2g^2}{(2\pi)^5\hbar^7} \int d\mathbf{p}_2 \int d\mathbf{p}_3 \int d\mathbf{p}_4 \, \delta(\mathbf{p} + \mathbf{p}_2 - \mathbf{p}_3 - \mathbf{p}_4) \\ \cdot \delta(\tilde{\epsilon}_p + \tilde{\epsilon}_{p2} - \tilde{\epsilon}_{p3} - \tilde{\epsilon}_{p4}) \\ \cdot [f f_2 (1 + f_3)(1 + f_4)] \, , \end{aligned} \tag{2.45}$$

the term $d\mathbf{r}d\mathbf{p}/(2\pi\hbar)^3 C_{22}^{\text{out}}$ represents the number of atoms leaving the infinitesimal phase-space volume element $d\mathbf{r}d\mathbf{p}/(2\pi\hbar)^3$ around $\mathbf{r}$ and $\mathbf{p}$. An integration over momenta in Eq. (2.45) then gives an expression for the mean number of atoms which undergo a collision per unit time and per unit volume at the point $\mathbf{r}$

$$\Gamma_{22}^{\text{out}}(\mathbf{r},t) = \int \frac{d\mathbf{p}}{(2\pi\hbar)^3} C_{22}^{\text{out}}(\mathbf{r},t). \tag{2.46}$$

Using Monte Carlo techniques it can be shown that the average number of collisions taking place in an infinitesimal volume element $\Delta\mathbf{r}$ in a time interval Δt can be expressed using collision probabilities, P_{ij}^{22}, between pairs of two test particles i and j (for a detailed discussion see Appendix A)

$$\frac{1}{2}\Gamma_{22}^{\mathrm{out}}\Delta\mathbf{r}\Delta t \simeq \gamma \sum_{(i,j)} P_{ij}^{22} \tag{2.47}$$

where the probability P_{ij}^{22} is given by

$$P_{ij}^{22} = \tilde{n}(\mathbf{r})\sigma|\mathbf{v}_i - \mathbf{v}_j| \int \frac{d\Omega}{4\pi}(1+f_3)(1+f_4)\Delta t. \tag{2.48}$$

The integral over Ω denotes an average over all possible scattering angles, where the outgoing states have a weighting factor $(1+f_3)$ and $(1+f_4)$ due to Bose enhancement. Momentum and energy conservation lead to outgoing velocities, which lie on a sphere with radius $\frac{1}{2}|\mathbf{v}_1 - \mathbf{v}_2|$ centered on $\frac{1}{2}(\mathbf{v}_1 + \mathbf{v}_2)$.

Although the collision probability is given by an integral over all possible scattering angles Ω, the test particles' velocities in a simulation must take specific values. This is achieved by selecting random numbers $\cos(\theta) \in [-1,1]$ and $\phi \in [0,2\pi]$ defining a random scattering angle Ω_R. Together with the incoming velocities $\mathbf{v}_1$ and $\mathbf{v}_2$ this defines the outgoing velocities $\mathbf{v}_3$ and $\mathbf{v}_4$. The collision probability then takes the form

$$P_{ij}^{22} = \tilde{n}(\mathbf{r})\sigma|\mathbf{v}_i - \mathbf{v}_j|(1+f_3^{\Omega_R})(1+f_4^{\Omega_R})\Delta t, \tag{2.49}$$

where the Bose-enhancement factors $(1+f_3^{\Omega_R})$ and $(1+f_4^{\Omega_R})$ are now determined by the specific outgoing velocities $\mathbf{v}_3$ and $\mathbf{v}_4$. The corresponding scattering event between particle i and j is sketched in Fig. 2.6. In a ZNG simulation the distribution function, needed to calculate the Bose-enhancement factors, is modeled by test particles. Hence, in order to calculate an expression for $f_3^{\Omega_R}$ and $f_4^{\Omega_R}$, test particles are binned into collision cells. This involves a binning in position- and in momentum-space, where a cloud-in-cell method (see section 2.2.3) is used to assign particles to the momentum grid points (for a detailed description of the binning method see Sec. 2.3.3). The weighting factor at each grid point of a momentum cell is additionally multiplied by a normalization factor $\gamma(2\pi\hbar)^3/(\Delta\mathbf{r}\Delta\mathbf{p})$, where $\Delta\mathbf{r}$ is the volume of the collision cell in position-space and $\Delta\mathbf{p}/(2\pi\hbar)^3$ is the volume of the collision cell in momentum-space. This normalization factor ensures that

$$\tilde{N}^{(n,k)} = \gamma\tilde{N}_{\mathrm{tp}}^{(n,k)} = f(\mathbf{r}_n,\mathbf{p}_k,t)\Delta\mathbf{r}_n\Delta\mathbf{p}_k/(2\pi\hbar)^3, \tag{2.50}$$

where $\tilde{N}_{\mathrm{tp}}^{(n,k)}$ is the test particle number in cell (n,k) (where n denotes the cell index in position-space and k denotes the index in momentum-space). This means that the integral of the sampled distribution function $f(\mathbf{r}_n,\mathbf{p}_k,t)$

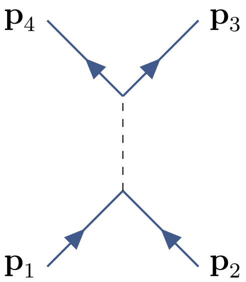

Figure 2.6 – Illustration of a scattering event between two incoming thermal particles 1 and 2 and two outgoing particles 3 and 4.

in collision cell (n,k) over the cell volume gives the particle number $N^{(n,k)}$ in that cell.

The actual calculation of C_{22} collisions proceeds as follows: test particles are first binned into collision cells in position-space. Then for each position cell the distribution function is calculated by assigning test particles to a momentum grid using a cloud-in-cell method. As the algorithm looks at one position cell n at a time, one only needs to store the momentum grid for that particular position cell. Without this the memory requirements of the system would render the calculation infeasible. In order to determine collision partners, the test particles are then grouped in pairs, where each test particle is only considered once, leading to $\tilde{N}_{\mathrm{tp}}^{(n)}/2$ pairs, with $\tilde{N}_{\mathrm{tp}}^{(n)}$ the test particle number in position cell n. For each pair (i,j) the collision probability P_{ij} can be calculated using Eq. (2.49) and is compared to a uniformly distributed random number X_{ij} between 0 and 1. If $X_{ij} < P_{ij}$ the collision takes place and the velocities of the involved particles are updated according to the randomly determined outgoing velocities $\mathbf{v}_3$ and $\mathbf{v}_4$. However, if $X_{ij} > P_{ij}$ the collision does not occur and the velocities of the involved particles stay the same. The algorithm proceeds by looking at the next pair until all $\tilde{N}_{\mathrm{tp}}^{(n)}/2$ have been processed. This procedure is repeated for every position cell.

As a final remark it should be noted that the factor γ only appears in the context of collisions, if one is interested in the physical collision rate. However, if probabilities are assigned to test particles in the simulation γ does not appear in the expression for the collision probabilities (2.49).

2.3.2 The C_{12} collision integral

Unlike the C_{22} collision integral the C_{12} collision integral involves scattering of a condensate atom. The rate of atoms leaving the condensate into the thermal cloud per unit volume and unit time is given by

$$\Gamma_{12}^{\text{out}} = \frac{\sigma n_c}{\pi m^2 (2\pi\hbar)^3} \int d\mathbf{p}_2 d\mathbf{p}_3 d\mathbf{p}_4 \delta(\mathbf{p}_c + \mathbf{p}_2 - \mathbf{p}_3 - \mathbf{p}_4)\delta(\epsilon_c + \epsilon_2 - \epsilon_3 - \epsilon_4) \times f_2(1+f_3)(1+f_4). \tag{2.51}$$

In the following discussion this will be referred to as the “out”-collision rate. In this notation atom 2 represents an atom which scatters with a condensate atom producing two outgoing thermal atoms 3 and 4.

The rate of atoms going into the condensate due to the scattering of two thermal atoms per unit volume and unit time can be written equivalently

$$\Gamma_{12}^{\text{in}} = \frac{\sigma n_c}{\pi m^2 (2\pi\hbar)^3} \int d\mathbf{p}_2 d\mathbf{p}_3 d\mathbf{p}_4 \delta(\mathbf{p}_c + \mathbf{p}_3 - \mathbf{p}_2 - \mathbf{p}_4)\delta(\epsilon_c + \epsilon_3 - \epsilon_4 - \epsilon_4) \times f_2(1+f_3)f_4.$$

Here the incoming atoms are labeled 2 and 4 and the outgoing thermal atom 3, to get the same weighting factor f_2 as in Eq. (2.51). This will be referred to as the “in”-collision rate.

In a similar way as for the Γ_{22} collision rate, the in- and outgoing rates, $\Gamma_{12}^{\text{out(in)}}$, in a time interval Δt and a small volume $\Delta\mathbf{r}$ can be approximated by collision probabilities (for details see Appendix A)

$$\Gamma_{12}^{\text{out(in)}} \Delta\mathbf{r}\Delta t \simeq \gamma \sum_{i=1}^{N_{\text{cell}}} P_i^{\text{out(in)}}. \tag{2.52}$$

The probability for a test particle to be involved in an “out”-collision takes the form

$$P_i^{\text{out}} = n_c \sigma v_r^{\text{out}} \int \frac{d\Omega}{4\pi}(1+f_3)(1+f_4)\Delta t, \tag{2.53}$$

where

$$v_r^{\text{out}} = \sqrt{|\mathbf{v}_c - \mathbf{v}_2|^2 - 4(U-\mu_c)/m} \tag{2.54}$$

plays the role of the relative velocities between the two incoming atoms with velocities $\mathbf{v}_2$ and $\mathbf{v}_c$, the former a thermal atom and the latter a condensate atom. U is the effective thermal cloud potential and μ_c the chemical potential of the condensate. As before the integral over Ω represents an average over all possible scattering angles.

Because the relative velocity, v_r^{out}, must take positive real values, expression (2.54) indicates that the constraint

$$|\mathbf{v}_c - \mathbf{v}_2|^2 > 4(U-\mu_c)/m \tag{2.55}$$

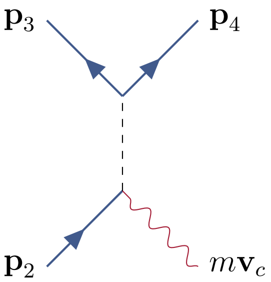

Figure 2.7 – Illustration of an "out"-scattering event for an incoming thermal particle 2 and a condensate atom. The scattering event results in two outgoing thermal particles 3 and 4.

must hold true. This represents a constraint for the incoming atom 2 and only test particles fulfilling the inequality (2.55) may be part of an "out"-type collision. The physical meaning of this constraint can be understood when looking at the different mean-field energies for condensate atoms $g(n_c + 2\tilde{n})$ and thermal atoms $2g(n_c + \tilde{n})$. If an atom leaves the condensate and goes into the thermal cloud there is an increase of gn_c in the potential energy. In order to conserve energy in a collision, this energy difference must come from the kinetic energy of the incoming thermal atom. Hence atom 2 needs an excess kinetic energy to compensate the difference in the mean-field energies. The connection between this energy difference and the inequality (2.55) may be seen in the Thomas-Fermi approximation where $U - \mu_c = gn_c$. As the collision partners have equal masses this leads to the constraint (2.55) in order to transfer the missing energy difference gn_c through a collision.
While the "out"-probability, P^{out}, looks similar to the collision probability between two thermal atoms, P_{22}, the "in"-probability takes a rather different form

$$P_i^{\mathrm{in}} = \frac{\sigma n_c}{\pi v_r^{\mathrm{in}}} \int d\mathbf{v}_\perp f_4(1 + f_3)\Delta t, \tag{2.56}$$

with v_r^{in} being the magnitude of the relative velocity $\mathbf{v}_r^{\mathrm{in}} = \mathbf{v}_2 - \mathbf{v}_c$ between an incoming thermal atom 2 and the condensate. The expression $f_4(1 + f_3)$ is integrated over all velocities, $\mathbf{v}_\perp$, lying in a plane perpendicular to $\mathbf{v}_r^{\mathrm{in}}$, where the velocity of the incoming atom 4, $\mathbf{v}_4$, is determined by $\mathbf{v}_\perp$ in the following way (please see Appendix A for a detailed discussion)

$$\mathbf{v}_4 = \mathbf{v}_c + \mathbf{v}_\perp + \frac{gn_c}{mv_r^{\mathrm{in}}} \hat{\mathbf{v}}_r^{\mathrm{in}}. \tag{2.57}$$

Here $\hat{\mathbf{v}}_r^{\mathrm{in}}$ is a unit vector in direction of $\mathbf{v}_r^{\mathrm{in}}$. The velocity of the outgoing atom

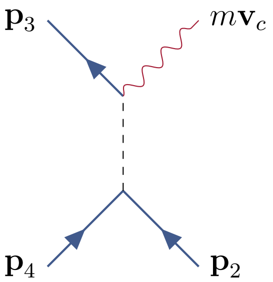

Figure 2.8 – Illustration of an "in"-scattering event for incoming thermal particles 2 and 4. The scattering event results in an outgoing thermal particle 3 and a condensate atom. Note that the indices of incoming and outgoing particles are different compared with those in Fig. 2.7 to get a similar looking expression for P_i^{in} and P_i^{out}.

3, $\mathbf{v}_3$, is then given by

$$\mathbf{v}_3 = \mathbf{v}_2 + \mathbf{v}_\perp + \frac{gn_c}{mv_r^{\text{in}}}\hat{\mathbf{v}}_r^{\text{in}}. \tag{2.58}$$

As in the case of C_{22} collisions, the integrals occurring in (2.53) and (2.56) are replaced by random numbers, so that specific values may be assigned to test particles if a collision takes place. The "out"-collision probability then takes the form

$$P_i^{\text{out}} = n_c\sigma v_r^{\text{out}}(1 + f_3^{\Omega_R})(1 + f_4^{\Omega_R})\Delta t, \tag{2.59}$$

where the expression $f_i^{\Omega_R}$ emphasizes the fact that the distribution function depends on a randomly selected scattering angle Ω_R. An "out"-collision process is illustrated in Fig. 2.7.

Using a Monte Carlo integration to solve the integral in (2.56), the "in"-collision probability becomes (for details see Appendix A)

$$P_i^{\text{in}} = \frac{\sigma n_c \mathcal{A}_v}{\pi v_r^{\text{in}}} f_4^{\mathbf{v}_\perp^R}(1 + f_3^{\mathbf{v}_\perp^R})\Delta t. \tag{2.60}$$

The distribution functions $f_i^{\mathbf{v}_\perp^R}$ depend on a randomly selected velocity $\mathbf{v}_\perp^R$ uniformly distributed over an area $\mathcal{A}_v$, which is perpendicular to the relative velocity $\mathbf{v}_r^{\text{in}}$.[2] By taking the average of the "in"-probability over N_v sample points, the value of the integral in (2.56) is approximated. This mean value is independent of the size of the area $\mathcal{A}_v$, as long as the whole occupied

---

[2] Please see Sec. 2.3.3 for a discussion about a convenient choice of $\mathcal{A}_v$ in dynamical simulations

phase-space is sampled by $f_4^{\mathbf{v}_\perp^R}$ and $f_3^{\mathbf{v}_\perp^R}$. An illustration of an "in"-collision process is given in Fig. 2.8.

To derive equations (2.59) and (2.60) quite different Monte Carlo approaches have been applied. In this form the cubic terms $f_2 f_3 f_4$, which cancel in the analytical C_{12} collision integral, may be non-zero due to numerical approximations. To solve this problem one may drop these terms artificially in the calculations, which is equivalent to dropping the terms $f_3 f_4$ in the final collision probabilities (2.59) and (2.60). This leads to new collision probabilities

$$\bar{P}_i^{\text{out}} = n_c \sigma v_r^{\text{out}} (1 + f_3^{\Omega_R} + f_4^{\Omega_R}) \Delta t, \tag{2.61}$$

and

$$\bar{P}_i^{\text{in}} = \frac{\sigma n_c \mathcal{A}_v}{\pi v_r^{\text{in}}} f_4^{\mathbf{v}_\perp^R} \Delta t. \tag{2.62}$$

To calculate whether a test particle takes actually part in an "in"- or "out"-collision, a random number $X_{12} \in [0,1]$ is selected. If $X_{12} < \bar{P}_i^{\text{out}}$ an "out"-collision takes place, which means that the velocity of the incoming particle is updated and a new test particle is created. If $\bar{P}_i^{\text{out}} < X_{12} < \left(\bar{P}_i^{\text{out}} + \bar{P}_i^{\text{in}}\right)$ an "in"-collision occurs and the incoming particle is deleted. Although an "in"-collision consists of two thermal particles colliding and one particle going into the condensate, the "in"-collision probability is calculated for every single test particle. Therefore if an "in"-collision takes place, a second thermal particle with velocity $\mathbf{v}_4$ must be found and updated to the outgoing velocity $\mathbf{v}_3$. If no suitable particle can be found in the current cell (this may happen due to the cloud-in-cell method) the search is expanded to neighboring momentum cells. Because this particle will have a velocity that differs slightly from $\mathbf{v}_4$, the calculations of the outgoing velocities are adapted to ensure momentum and energy conservation.

So far collisions were only considered in the context of the thermal cloud. However the C_{12} collisions have a direct effect on the condensate wavefunction $\Phi(\mathbf{r},t)$ due to the R-term appearing in (1.59), which couples the quantum Boltzmann equation to the generalized GPE. The equation defining this R-term (1.79) can be rewritten by splitting the total C_{12} collision rate into Γ_{12}^{in} and Γ_{12}^{out}, leading to

$$R(\mathbf{r},t) = \frac{\hbar}{2n_c(\mathbf{r},t)} (\Gamma_{12}^{\text{out}}(\mathbf{r},t) - \Gamma_{12}^{\text{in}}(\mathbf{r},t)). \tag{2.63}$$

In the simulation $R(\mathbf{r},t)$ is discretized on the grid used for the wavefunction $\Phi(\mathbf{r},t)$. For that purpose R_i, corresponding to the contribution of a test particle

i to the total term $R(\mathbf{r},t)$, is calculated using the collision probabilities

$$R_i = \frac{\gamma\hbar}{2n_c\Delta\mathbf{r}\Delta t}(\bar{P}_i^{\mathrm{out}} - \bar{P}_i^{\mathrm{in}}), \tag{2.64}$$

where $\Delta\mathbf{r}$ is the volume of a grid cell used for the wavefunction discretization. For each test particle R_i is assigned to grid points using the cloud-in-cell method described earlier. The source term R_{klm} at a given grid point r_{klm} (where k,l and m denote grid indices for the x, y and z directions respectively) is given by the sum over all single test particle contributions at that point. The change of the discretized wavefunction $\Phi(r_{klm},t)$ at that grid point r_{klm} due to the C_{12} collisions is then given by

$$\Phi(r_{klm},t+\Delta t) = e^{-R(r_{klm},t)\Delta t/\hbar}\Phi(r_{klm},t). \tag{2.65}$$

Therefore the norm of the wavefunction changes if there is a difference between the “in”-and “out”-collision rate, independent of whether collisions actually take place or not. Hence, the total atom number is only conserved in a statistical sense, and numerical fluctuations in thermal atom number and condensate atom number may occur.

Because “in”-and “out”-collisions are treated differently, a small numerical deviation even in equilibrium is inevitable. This may lead to drifts in the total particle number or a net particle transfer between the condensate and the thermal cloud. The main error arises due to the sampling of the distribution function with test particles. These effects can be minimized by an appropriate choice of collision cells. On the one hand many particles in a cell lead to good statistics, on the other hand the resolution of the distribution function increases with a lower cell size. An adaptive-binning method is therefore desirable because it is not clear how to choose an optimal grid in position- and in momentum-space beforehand. Details of a possible implementation are given in the next subsection.

2.3.3 Binning procedure

In order to calculate collision probabilities and find collision partners, test particles are binned into collision cells. In contrast to former ZNG implementations, which were optimized to systems with cylindrical symmetry [98], a Cartesian grid in position- and momentum-space was chosen, which allows simulations of arbitrary trap geometries.

The goal of an adaptive-binning method is to distribute particles into collision cells in position-space, so that each cell contains approximately an equal number of particles. The implemented procedure is based on a method outlined by Bird [99] and has been applied to very cold, dilute gases by Wade et. al. [103]. In this method the test particles are first binned on a master grid consisting of rectangular cuboids of equal size. After that, these so-called master cells are subdivided into smaller cells dependent on the particle number within a cell. This leads to a subdivision of highly occupied master cells, which increases the resolution of the distribution function in regions where there are many test particles. For this reason a threshold value N_{th} is chosen and a given master cell n with $\tilde{N}_{\mathrm{tp}}^{(n)}$ test particles is subdivided such that each subcell contains an average of N_{th} particles. This may be achieved by calculating an integer l, so that $\tilde{N}_{\mathrm{tp}}^{(n)}/2^l$ is close to, but not less than, N_{th}. Then the master cell is subdivided into 2^l subcells, with no preference in any direction. Afterwards, particles have to be binned on a new grid in momentum-space for each subcell. The number of grid points in momentum-space stays the same throughout the simulation and is equal for every subcell, but the resolution changes. The maximum momentum of the test particles in a subcell, p_{max}, is determined and the box in momentum-space is defined from $-p_{\mathrm{max}}$ to p_{max} in each direction. This also defines the size of the area $\mathcal{A}_v$ appearing in the "in"-probability expression (2.56):

$$\mathcal{A}_v = \frac{\pi p_{\mathrm{max}}^2}{m^2}. \tag{2.66}$$

This ensures that the whole occupied phase-space is sampled by $\mathcal{A}_v$ using a high resolution. The subdivision of master cells is illustrated in Fig. 2.9.

As a final comment it should be noted that the optimal threshold numbers N_{th} differ from those found for the classical Boltzmann equation in the case of dilute cold gases [103]. This is due to the fact that for a classical gas the collision probabilities do not directly depend on the distribution function. In that case a binning in momentum-space is unnecessary and N_{th} can be very low (down to only 2). This is not the case in a ZNG simulation where Bose enhancement is taken into account. In fact an unphysical particle drift from the thermal cloud into the condensate was observed for threshold numbers $N_{\mathrm{th}} \lesssim 85$, due to bad statistics, and N_{th} was in most simulations chosen to be around 200. An example for subdivision of collision cells from a simulation with 10^6 test particles is shown in Fig. 2.10.

2.3.4 Transient adaptive subcells

In the case of C_{22} collisions, particles are paired in subcells and the corresponding collision probabilities are calculated. When these pairs of particles are randomly chosen it may occur that colliding particles are far away from each other, depending on the size of the current subcell. This may lead to

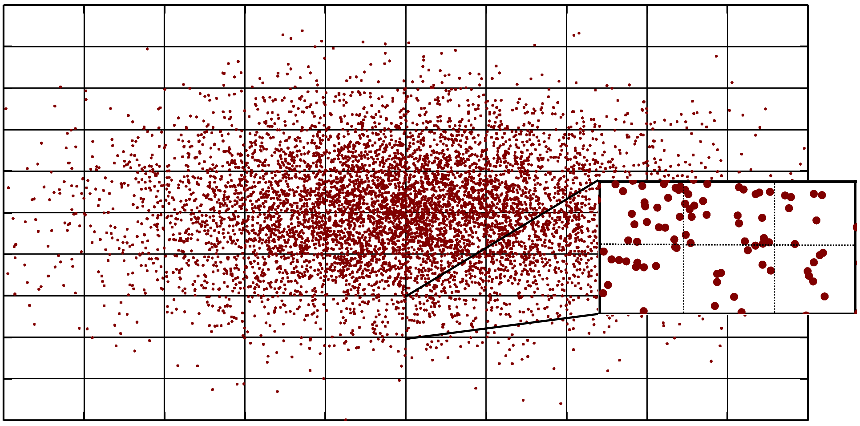

Figure 2.9 – A sketch of particles (red dots) representing a thermal cloud, which are binned into equally sized master cells in position-space. The cells on the master grid are chosen to be relatively large, leading to high particle numbers in regions where the density is high. Subdivision of these cells leads to a higher resolution of the distribution function.

unphysical information transport across a long distance. It would be desirable to form nearest neighbor pairs, so that only test particles in the vicinity of each other can collide. Unfortunately, calculating the exact nearest neighbor pairs is very expensive and scales with $\mathcal{O}(N^2)$. A possibility to avoid these costs was suggested among others by Bird [101, 102, 126]. In this scheme the already calculated subcells are further divided into even smaller cells, the so-called transient-adaptive subcells (TASC). Collision partners are then only chosen from the same or a neighboring TASC, reducing the separation between colliding particles significantly. The TASC are ideally chosen so that there is an average of two particles in each cell. This is achieved by dividing each subcell with a given test particle number $\tilde{N}_{\mathrm{sc}}$ into $\lfloor \sqrt[3]{\tilde{N}_{\mathrm{sc}}} \rfloor$ equally spaced TASCs in each direction, where $\lfloor x \rfloor$ is the floor function. Although the calculation of TASCs does not provide information about the exact nearest neighbors, the distance between colliding particles is drastically reduced and the run-time complexity scales with $\mathcal{O}(N)$. It is important to note that the TASCs are only used to determine collision partners for the C_{22} collisions. The distribution function is still sampled in the bigger subcell to ensure good statistics for the collision probabilities.

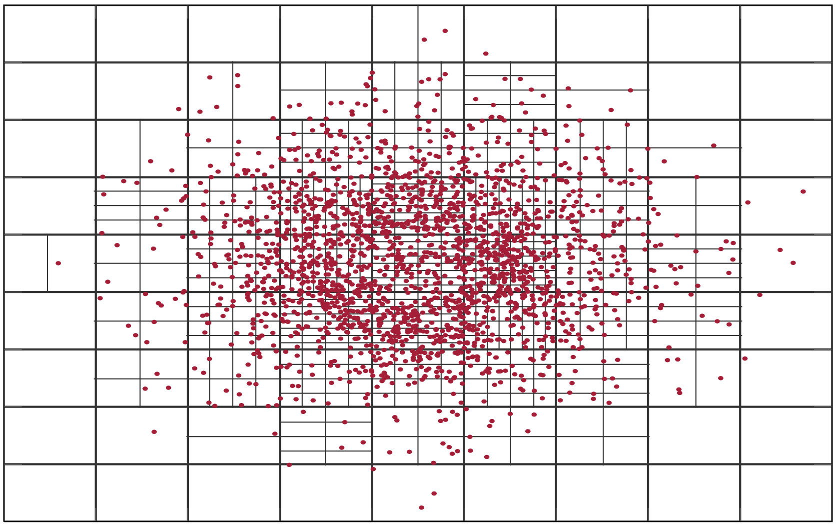

Figure 2.10 – Illustration of master cells and division into smaller subcells in regions where the test particle number is above $N_{\mathrm{th}} = 100$. The total test particle number is 10^6 and the equilibrium state is the same as that in Fig. 2.5. Nine master cells are used in each direction. Plotted are particles in master cells around $z = 0$ along the x- and y-direction. For clarity only a small fraction ($\sim 1\%$) of the particles is shown.

2.4 Parallelization

The time evolution of the condensate and the test particles can be very time consuming. In the case of test particle numbers $\gtrsim 10^6$ the thermal cloud evolution is the limiting factor of simulation run times. If this is the case it is favorable to distribute test particles over several processor cores and to calculate the collisionless term and collisions in parallel. For that purpose the open version of the message-passing-interface (openMPI) is used [127], where each core, which is referred to as a process in the context of MPI, has its own namespace. Information between different processes is then exchanged using messages. In the case of the ZNG algorithm this means that every core is responsible for a given portion of the box in which the condensate and the thermal cloud are defined and test particles, as well as the wavefunction, are distributed accordingly.

2.4.1 Data distribution

As mentioned before, the FFTW package is used to calculate the discrete Fourier transformation, which is needed for the calculation of the time evolution of the condensate and the thermal density. This package also allows calculations in parallel. FFTW chooses the distribution of grid points to cores itself and follows a 1D-block distribution along the first dimension. That means that a 3D vector is only divided along the first dimension (which was the x-dimension in the simulations). This distribution was adopted for the thermal cloud and test particles were sent to each process depending on their position in the x-direction. The FFTW package provides documentation on how to distribute a given data vector in parallel. The user is then responsible for implementing this distribution. The function fftw_mpi_local_size_3d, telling the user how FFTW wants to divide the 3D vector with total size $n_x \times n_y \times n_z$, can be called on every process. The distribution information for the current process is then stored in the variables $local\_n_x$ and

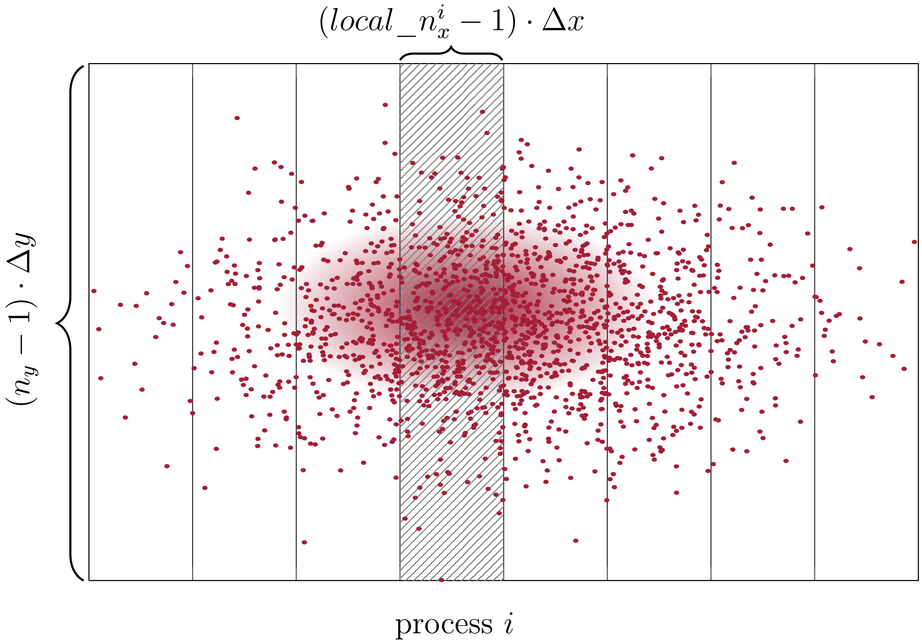

Figure 2.11 – Two-dimensional sketch of a 1D-block distribution along the x-dimension for the ZNG code. Δx and Δy denote the resolutions in the x- and y-direction. Each process stores the full box along the z- and y-direction and only a region of the size $(local\_n_x^i - 1) \cdot \Delta x$ along the x-direction.

local_x_start:

fftw_mpi_local_size_3d(ptrdiff_t n_x, ptrdiff_t n_y, ptrdiff_t n_z,
MPI_Comm *comm*,
ptrdiff_t $*$*local_n*$_x$, ptrdiff_t $*$*local_x_start*).

The variable *comm* tells the function which processes are involved in the calculation of the Fourier transform. After calling the function on process i, the variable *local_n*$_x$ gives the number of points along the x-direction which are transformed on the current process. Each process therefore only needs to store a vector with size *local_n*$_x \times n_y \times n_z$, where *local_n*$_x$ may differ between each process. The variable *local_x_start* tells the user where the *local_n*$_x \times n_y \times n_z$ sized portion lies in the original vector, so each process takes care of a part of the original vector, which starts at *local_x_start* and goes to *local_x_start*$+($*local_n*$_x-1)$ in the x-direction. This is illustrated in Fig. 2.11 for a given process i and corresponding local variables *local_n*^i_x and *local_x_start*^{i}. This data distribution is used throughout the parallelized ZNG algorithm for the condensate and for the thermal density.

2.4.2 Collisionless motion and ghost cells

The mean-field terms in the Hartree-Fock potential depend on the condensate and the thermal cloud density. Therefore, in order to evolve a test particle i at position $\mathbf{r}_i$ in time, the Hartree-Fock potential $U = 2g\left(n_c(\mathbf{r}_i) + \tilde{n}(\mathbf{r}_i)\right)$ corresponding to $\mathbf{r}_i$ has to be stored on the same process as the test particle. Hence, the data distribution discussed in the former section also dictates how test particles are assigned to processes. This is done by binning each test particle to a grid point in the x-direction and sending it to the corresponding process.

Although this provides values for the thermal cloud and the condensate density at the position $\mathbf{r}_i$ of the test particle i, the data distribution over several cores causes an inconvenience. The time iterator for a test particle demands the calculation of the potential term $U(\tilde{\mathbf{r}}_i)$ at an estimated midpoint $\tilde{\mathbf{r}}_i$ (see Eqs. (2.27) - (2.29))

$$\tilde{\mathbf{r}}_i = \mathbf{r}_i(t) + \frac{1}{2}\mathbf{v}_i(t)\Delta t. \tag{2.67}$$

If a particle's x-coordinate is close to the boundary of the local grid on the current process, it may happen that the necessary grid point $\tilde{\mathbf{r}}_i$ is stored on another process. Additionally the gradient of the potential term, $\nabla U(\tilde{\mathbf{r}}_i)$, has to be calculated in order to update the test particle's velocity, which involves

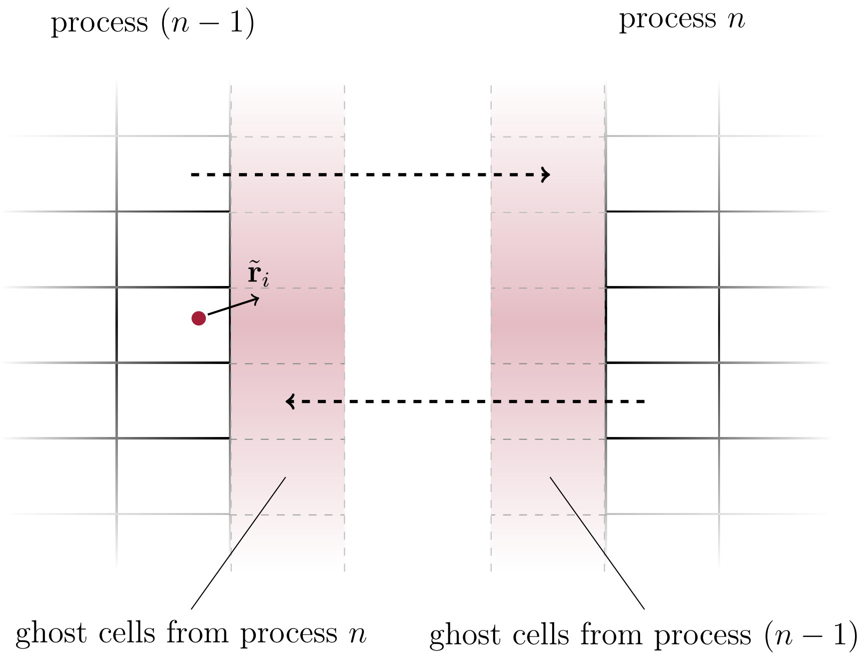

Figure 2.12 – Illustration of ghost cells for a two-dimensional grid. Every cell along the border of a process in the x-direction is copied and sent to the neighboring process.

information about neighboring grid points. So even more grid points, which may not be available on the process where the test particle is stored, have to be taken into account for the thermal cloud time evolution.

This problem can be solved by mirroring adjacent cells which are stored on different processes. Therefore the cells which lie at the border of a process are copied and sent to the next neighboring process, where they are stored into so-called ghost cells [128] after each time step, as illustrated in Fig. 2.12. A function which needs values from a neighboring process can then access this information using the corresponding ghost cells. Because two rows of ghost cells may be needed for the term $\nabla U(\tilde{\mathbf{r}}_i)$ a process has to store $4 \times n_y \times n_z$ ghost cells in total for each grid, $2 \times n_y \times n_z$ for both the upper and the lower neighboring process. This is done for the thermal density and the wavefunction of the current and the previous time step. The ghost cells not only provide an effective method to parallelize the test particle time evolution but also allow one to calculate physical values in parallel which require derivatives of the wavefunction, such as the condensate energy or the condensate velocity.

After each time step the ghost cells have to be updated and particles which crossed the line between two processes have to be sent to their new process. In addition processes have to communicate with each other when values are assigned to grid points using the cloud-in-cell method. A value (for example the R-term) which is calculated at the border of a process may be assigned to a grid point of an adjacent process. In that case the values are summed and assigned to ghost cell points, which are then sent to the neighboring process and added to the corresponding grid point.

2.4.3 Collisions

Parallel calculations of collisions are done by assigning an equal number of master cells to each process. In this way the calculation of subcells and TASC is straightforward but it introduces the constraint that the grid size has to be an integer multiple of the master cell number along the x-direction, to avoid master cells of differing size. In addition if the grid size is not an integer multiple of the number of processes used, the FFTW package distributes a data portion to the last process, which has a different size than all the others. This leads to master cell sizes in the last process, which differ from those in the other processes. However if the number of processes is high enough and the box is large enough, only a few particles reside on the last process and a difference in the master cell size at the border of the region has only a small effect on the dynamics.

2.4.4 Overview

To close the discussion about the implementation details of the ZNG method, this section gives an overview of the algorithm as a whole and shows in a simplified way, how a single time step is calculated (see Fig. 2.13).

At a given time step $n+1$ the algorithm iterates the discretized condensate wavefunction $\psi(r_{klm},t_n)$, where k,l,m are the discretization indices in the x-,y- and z-direction, in time using the split-step method. This gives a new value for the condensate density $n_c(r_{klm},t_{n+1})$. With the help of this new density the potential acting on the thermal atoms $U(r_{klm},t_{n+1})$ can be calculated and the test particles' positions and velocities are updated accordingly. This is the calculation of the collisionless part of the quantum Boltzmann equation. Afterwards, particles are assigned to grid points using the cloud-in-cell method and a convolution of the resulting histogram with a broadening function yields a new thermal density $\tilde{n}(r_{klm},t_{n+1})$.

The algorithm then proceeds by assigning test particles to master cells which are further divided into subcells depending on the test particle number in each cell. In the case of C_{22} collisions, collision partners are searched for within TASCs. After calculating C_{12} collisions, the R-term, which ensures total particle number conservation in a statistical sense, is determined and as a final step, boundary conditions concerning the test particles are calculated. These boundary conditions are given by the experimental setup.

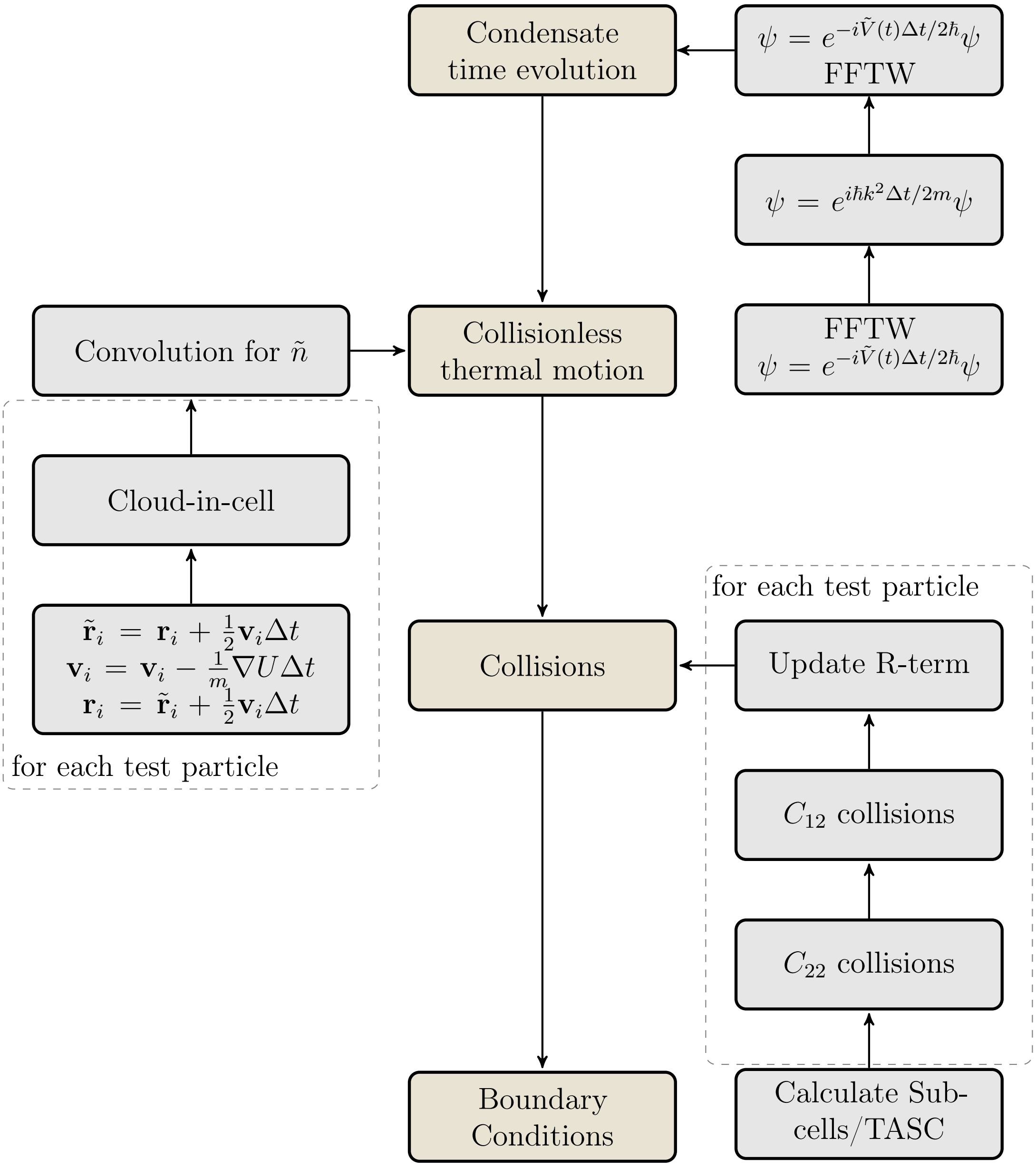

Figure 2.13 – A single, simplified time step of the ZNG algorithm. Main steps of the algorithm are highlighted in golden boxes, gray boxes give insight into the implementation, which is described in more detail in previous sections.

2.4.5 Benchmark

To show the effects of the previously discussed parallelization on run times, an initial state with a different number of test particles and a different number of cores is iterated in time. This is done using a full ZNG implementation including the collisionless Boltzmann term, collisions and condensate dynamics. The result is shown in Fig. 2.14. The time costs per single step of the algorithm are plotted against the number of test particles, where different colors denote different number of processes. For large test particle numbers the algorithm scales with $\mathcal{O}(N)$ and saturates for very low numbers mainly because of the time evolution of the condensate. By using 24 cores the cost of one single time step is approximately an order of magnitude lower than for the case of one single core for a gas with 1.8×10^6 test particles. Increasing the process number further leads to a saturation of the time used per step because the communication costs between processes becomes dominant.

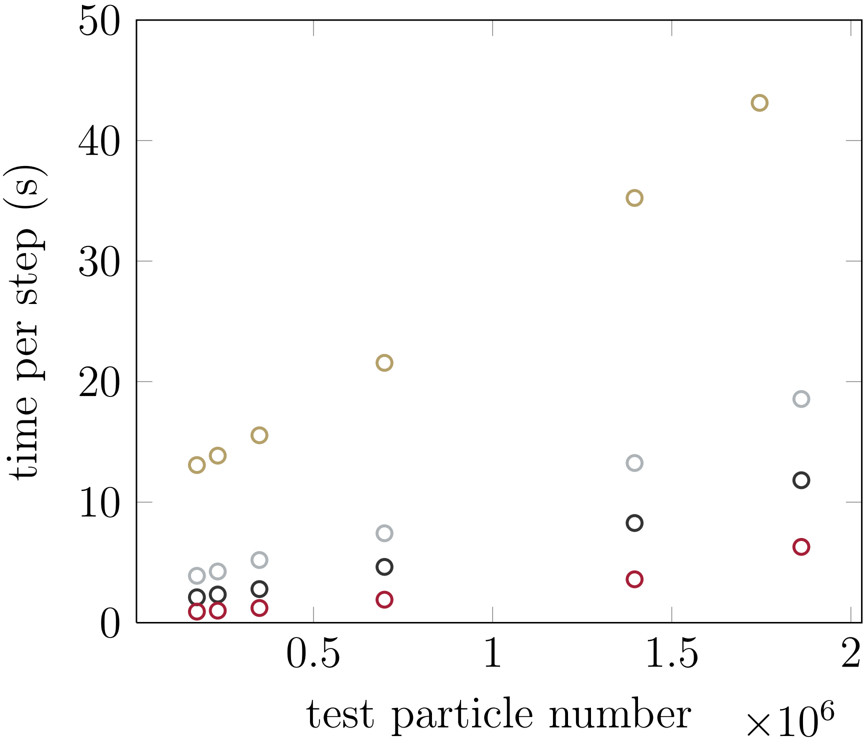

Figure 2.14 – Time per step for different test particle numbers shown for one core (gold open circle), four cores (gray open circles), eight cores (black open circles) and twenty four cores (red open circles).

2.5 Testing

Testing of implemented algorithms is an essential task, especially in numerical science. In most cases this is done by simulating a simple system which can either be described analytically or whose behavior is predictable. A comparison between the simulated data and the analytical values not only offers possibilities to debug the written code, but also gives insight into applicability and errors of a given model.

2.5.1 Equilibrium state

A system which is well studied, experimentally as well as theoretically, is an equilibrium state of bosons in a harmonic trap at very low temperatures. It is therefore an excellent system to test the ZNG implementation. In the first instance, this may be done by comparing the collision rate Γ_{22} of a full ZNG simulation with a direct Monte Carlo solution of the collision integral for the state discussed in Sec. 2.1.2 (Fig 2.15). Using the distribution function of the numerical Hartree-Fock equilibrium solver for that state one may calculate Γ_{22} directly using the expression (see Appendix A.2 Eq. (A.10))

$$\Gamma_{22} \simeq (p_{\max})^6 w_{\max} \frac{1}{N} \sum_i{}' g(p_i), \tag{2.68}$$

where $w_{\max}$ is the maximum of the function $w(p)$

$$w(p) = \frac{f(\mathbf{p}_1) f(\mathbf{p}_2)}{(2\pi\hbar)^6} \tag{2.69}$$

and

$$\tag{2.70}$$

$$g(p) = \int \frac{d\Omega}{4\pi} \sigma |\mathbf{v}_1 - \mathbf{v}_2| (1 + f_3) \cdot (1 + f_4). \tag{2.71}$$

Only accepted points p_i contribute to the sum in Eq. (2.68), which is denoted by the prime.

The golden curve in Fig. 2.15 shows the result of this direct calculation depending on the distance r from the trap center. The collision rate exhibits a sharp maximum in the region where the condensate vanishes and the thermal density is highest. This peak is enhanced in Fig. 2.15 by the multiplication with $4\pi r^2$, which corresponds to an integration over θ and ϕ in spherical coordinates, because of the isotropic trap geometry. The direct calculation

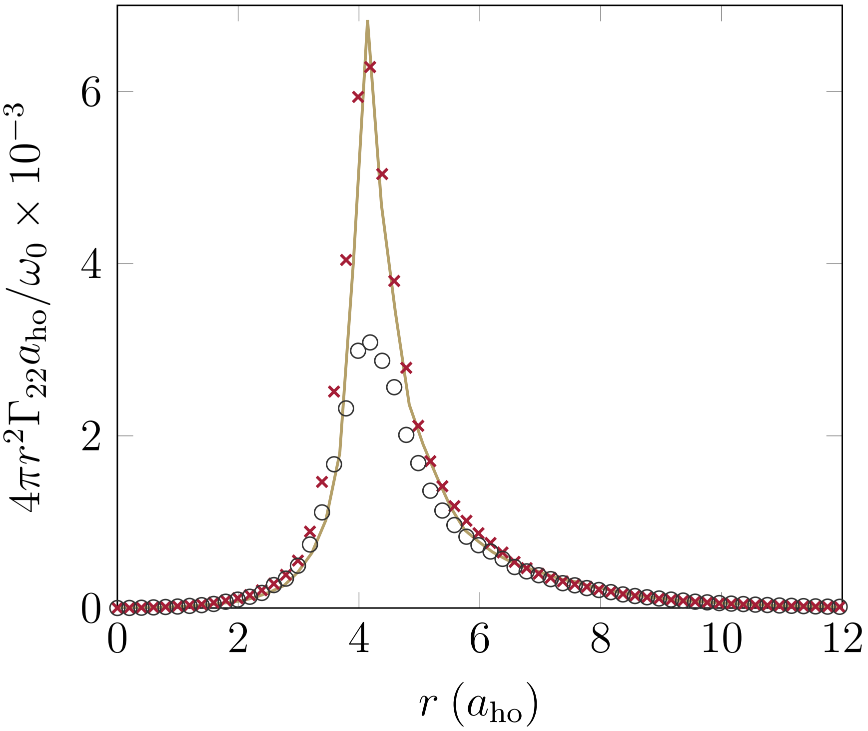

Figure 2.15 – Collision rate Γ_{22} over the distance r from the trap center. The golden curve shows direct Monte Carlo calculations of the collision integral using Eq. (2.68). Gray open circles are from a ZNG simulation with a fixed number of collision bins and no adaptive subdivision. Red crosses show the result from a ZNG simulation with adaptive subdivision of collision cells. The threshold particle number for a subdivision was 85 particles.

differs from a ZNG simulation with 24 collision cells in each dimension and no subdivision of cells (open gray circles) by approximately a factor of two in the region where collision rates are highest. Without a subdivision of collision cells the resolution of the distribution function is too low and the sharp peak in the collision rate cannot be modeled by the test particle simulation. However with an adaptive subdivision and a threshold number of 85 particles per cell (red crosses) the resolution of the distribution function rises significantly in regions where many test particles reside (and hence where the thermal density is highest). In this case the ZNG results are in good agreement with the direct calculation.

To further explore the behavior of the ZNG model over time the initial state was iterated using a full-dynamical ZNG code, which included the motion of test particles in the effective potential and the calculation of collisions. The resulting condensate and thermal atom numbers are shown in. Fig. 2.16. Because the cloud is supposed to be in thermal equilibrium during the simulation no net transfer of particles from one region to the other should be observed. However, at the beginning of the simulation, a small imbalance between the "in"- and "out"-collisions leads to a rethermalization of the state. After approximately 10 ms the gas reaches a new equilibrium state with ca. 17100 condensate atoms instead of 16735 atoms, which corresponds to an error of approximately 2.0%. This small error is mainly a consequence of differences between the calculations of "in"- and "out"-collisions (Eq. (2.56) and Eq. (2.53)) and discretization errors in the Hartree-Fock equilibrium state. However, after the initial thermalization the atom numbers in the thermal cloud and the condensate fluctuate around the new equilibrium values, where the fluctuations are on the order of about 0.5%. The total atom number is only conserved in a statistical sense.

2.5.2 Quench simulation

Although the equilibrium state is an important test for every finite-temperature model, it is not sufficient if one wants to study dynamics in a gas. Far from equilibrium, the collisions should rethermalize the initial system and drive it towards equilibrium again. It is therefore useful to look at the time evolution of a non-equilibrium initial state.

Taking an initial equilibrium state and reducing the temperature suddenly by a factor 2 yields an easy way to test this behavior. This has been done by Jackson et al [107] and by comparing the results of this "quench" simulation with their work yields the opportunity to test whether the presented ZNG implementation is consistent with former work. In addition, this system models radio-frequency evaporative cooling in a simplified way, which is a common way to produce a BEC in experiments [129]. It is therefore important to show that the implemented ZNG model reproduces the quench results of Jackson to be confident that it can describe cooling and condensate growth.

The initial state for this simulation consists of $N = 50000$ ^{87}Rb atoms in an isotropic trap with frequency $\omega = 2\pi \times 187\,\mathrm{rad\,s^{-1}}$ at a temperature $T = 200\,\mathrm{nK}$. The state is prepared using the Hartree-Fock equilibrium code leading to 2.58×10^4 atoms in the condensate. Using the rejection method, positions and velocities are assigned to the test particles, but in this case a distribution function was used, in which the temperature was reduced by a factor of 2

$$f(\mathbf{p},\mathbf{r}) = 2^{3/2} \frac{1}{z(\mathbf{r})^{-1} e^{2\beta \frac{\mathbf{p}^2}{2m}} - 1}. \tag{2.72}$$

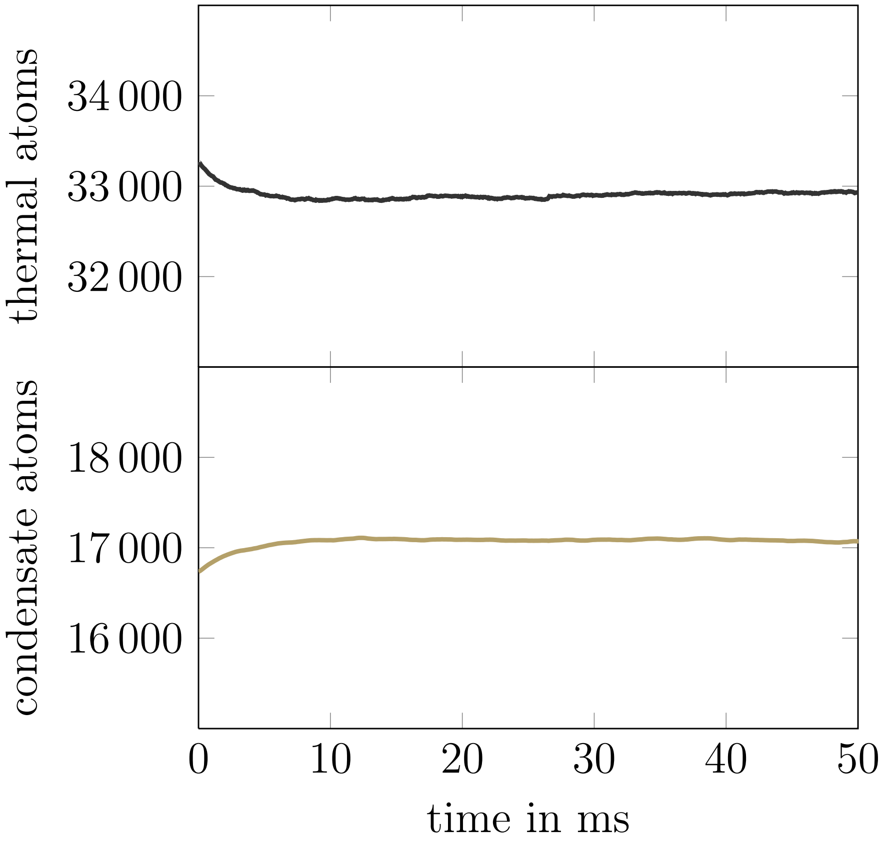

Figure 2.16 – Time evolution of the condensate (lower panel) and thermal particle (upper panel) number for the equilibrium state in Sec. 2.1.2. The initial state, which was calculated using the Hartree-Fock ground-state code as outlined in Sec. 2.1.2, rethermalizes to a new equilibrium state with a slightly higher condensate fraction.

As the simulation proceeds, the lowered velocities result in a motion of thermal particles towards the trap center and the thermal cloud collapses. However the mean-field potential as well as collisions lead to a repulsion of thermal atoms as the density in the middle of the trap rises and thermal atoms are again pushed away from the trap center. This leads to an oscillation of the cloud, which is damped out over time because of collisions. At the same time the “in”-collisions lead to a condensate growth and loss of thermal particles. This behavior is shown in Fig. 2.17, where the red curve shows the thermal atom number and the black curve refers to the atom number in the condensate. The golden curve shows the total atom number divided by 2 (for convenience of illustration), revealing that there is no significant total particle number drift beside the fluctuations mentioned in Sec. 2.3. This graph is in

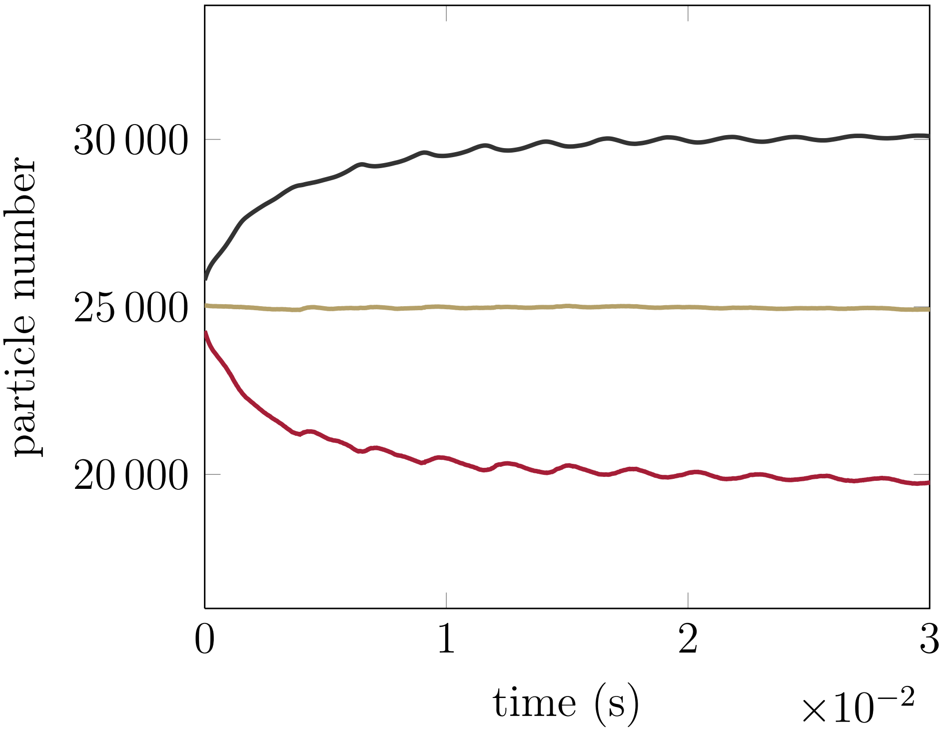

Figure 2.17 – Quench simulation for a state with 50000 ^{87}Rb atoms at an initial temperature $T = 200\,\mathrm{nK}$ in an isotropic trap with frequency $\omega = 2\pi \times 187\,\mathrm{rad\,s^{-1}}$. Shown is the condensate atom number (black curve), the thermal atom number (red curve) and total atom number divided by 2 (golden curve). The quench in momentum-space leads to a damped oscillation of the cloud and a growing condensate. Particle drifts due to numerical errors are small, which is indicated by a nearly constant total atom number.

close agreement with the results from Jackson et al [107], showing that the presented implementation is consistent with former work in the field.

Chapter 3

Surface evaporation

A cold cloud in front of a solid surface is one of the most basic hybrid systems consisting of cold atoms and solid-state devices. It is also rather common, as it is realizable in every atom chip experiment [58–63, 130–132] and the atom loss curves are frequently used to calibrate the position of the surface [47, 133]. Furthermore, bringing an atom cloud close to a surface can be an effective technique to cool the cloud [49, 134]. Atoms in a harmonic trap, which hit the surface, are lost either because they scatter from, or are absorbed by the surface. The surface cuts off atoms which have enough energy to reach it, leaving the other atoms nearly unperturbed and, depending on the position of the surface, evaporative cooling can be achieved [132, 135]. Counterintuitively, this holds true even for very cold atoms and a surface at room temperature, which makes it possible to cool a cold thermal cloud of ^{87}Rb down below the critical temperature T_c using a hot silicon surface.

However, despite the prevalence of the cloud-surface system there is little theoretical work on the subject. In fact, even for free-space radio-frequency (RF) evaporative cooling, most studies relied either on the uncontrolled assumption of ergodicity [66, 136], or were based on a classical model such as the classical Boltzmann equation [129, 137–139]. In this context condensate growth due to the cooling mechanism was studied. This was either done by a sudden truncation of the thermal distribution [136, 140–142] or through a dynamical quench [143–148].

However, the surface problem is even more complex and has not been theoretically studied, either qualitatively or quantitatively [149]. The description of the interactions between the atoms and a surface and between the atoms themselves makes the numerical simulation a challenging task. This holds especially true when the cloud undergoes a phase transition because of the cooling mechanism. A full dynamical description of the thermal cloud is needed, which allows one to model thermalization effects far from equilibrium, taking Bose enhancement into account.

To confirm the validity of ZNG for this set up, data from simulations is compared with experimental results in the following section. It is shown that ZNG, although not designed to model phase transitions, may capture the key physics of this system and the simulations lead to reasonable results considering the atom loss curves and condensate growth. Comparison with other simpler analytical models for the atom loss curves is provided and deviations from the ZNG simulations are discussed.

3.1 Atom-wall interaction

For distances larger than the atomic radius the potential between a single atom and a wall can be described by the Casimir-Polder potential [150]. In the case of an infinite wall it can be approximated by a so-called single-correction function [151]. For a surface lying in the $x = 0$ plane it takes the form

$$V_{\mathrm{CP}}(x) = -\frac{C_4}{x^3 \cdot (x + \frac{3\lambda}{2\pi^2})}, \tag{3.1}$$

where $\lambda \approx 780\,\mathrm{nm}$ is the effective atomic transition wavelength for ^{87}Rb and C_4 is a material constant

$$C_4 = \frac{3\hbar c\alpha}{32\pi^2\epsilon_0}\left(\frac{\epsilon - 1}{\epsilon + 1}\right)\Phi(\epsilon), \tag{3.2}$$

with ϵ the relative permittivity of the surface, ϵ_0 the vacuum permittivity, α the static polarizability of the atom, and $\Phi(\epsilon)$ a dimensionless constant for the surface [152]. For a silicon surface and ^{87}Rb, $C_4 = 1.22 \times 10^{-55}\,\mathrm{Jm}^4$ [153].

Atoms which are confined by magnetic fields of a microchip trap see this attractive Casimir-Polder potential and a harmonic potential coming from the trap. For a surface lying in the $x = 0$ plane and a trap center at a distance x_s to the surface, the total potential becomes

$$V(\mathbf{r}) = \frac{1}{2}m\omega_x^2(x - x_s)^2 + \frac{1}{2}m\omega_y^2 y^2 + \frac{1}{2}m\omega_z^2 z^2 + V_{\mathrm{CP}}(x). \tag{3.3}$$

Far away from the surface the atoms only see the trapping potential, whereas close to the surface the attractive Casimir-Polder potential dominates. In the intermediate regime, the Casimir-Polder potential leads to an opening of the trap and atoms are lost due to the surface. This behavior is sketched in Fig. 3.1.

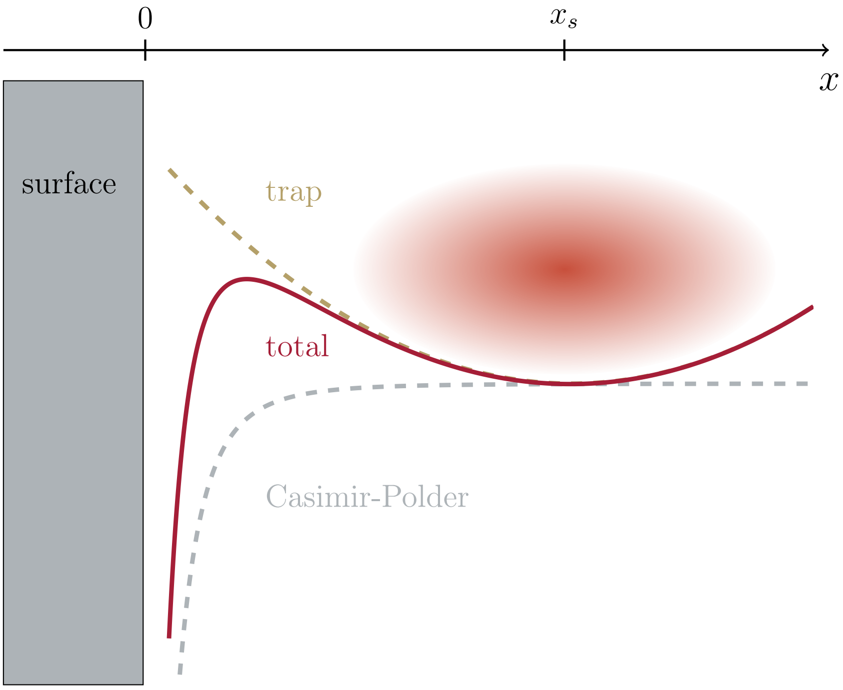

Figure 3.1 – The total potential $V(x,y=0,z=0)$ (red solid curve) for atoms in a harmonic trap in the vicinity of a surface. For short distances the Casimir-Polder potential (gray dashed curve) dominates. Far away from the surface the atoms only see the trapping potential (gold dashed curve). In between, the Casimir-Polder potential leads to an opening of the trap. Solid rectangle indicates the surface and the colored oval indicates the atom cloud. Black arrow shows the x-axis with x_s the distance between the trap center and the surface.

3.2 Implementation details

In the simulations the total potential in Eq. (3.3) was calculated for the condensate evolution and combined with a linear imaginary potential, starting from the point where the trap opens, which leads to particle loss. In addition, test particles beyond this point were deleted after each time step. For a constant value of $\gamma = \tilde{N}/\tilde{N}_{\mathrm{tp}}$ this also leads to a loss of physical thermal particles.

During experiments, a condensate may form due to the evaporative cooling effect. In order to describe condensate growth in the simulations, the "in"-collision probability in Eq. (2.60) needs to be finite. However, when starting with a thermal gas in a simulation the condensate density is zero and hence the "in"-collision probability is also zero. In reality, large occupation-number fluctuations near the critical temperature T_c would provide a condensate seed, which allows an enhanced growth of the ground-state population due to Bose statistics. Because these fluctuations are neglected in the ZNG model a condensate seed is implemented artificially. The approximate size of the seed was estimated by using the Bose-Einstein distribution and assuming $\mu_c = 0$, which results in a ground-state occupation of about ~ 200 atoms. Thus a seed of 200 atoms was planted in the thermal cloud and was not allowed to drop below this critical value. This is a mere 0.1% of the total atom number and hence should not affect other results.

3.3 Time series

Particle loss curves of a cold cloud in front of a surface exhibit a non-trivial behavior. The curves are influenced by the atom species, the surface material, the initial particle number, the trap frequencies, the temperature, the distance to the surface and the transport velocity of the cloud. In this section, experimental loss curves as a function of time, which were measured by Federsel in the group of Prof. Fortágh, are compared with ZNG simulations and it is shown that the method may be used to describe the experimental data within the given error bounds.

In the experiments a cloud of ^{87}Rb atoms was prepared in a trap with frequencies $\omega_x = 2\pi \times 16\,\mathrm{rad\,s^{-1}}$, $\omega_y = \omega_z = 2\pi \times 85\,\mathrm{rad\,s^{-1}}$ and a trap center located at $x_s \approx 134\,\mu\mathrm{m}$ away from the surface. The cloud was then transported in 1 s towards the surface and held at a final position for a variable time. In order to measure the remaining atom number, N, after a certain hold time the cloud was swiftly brought back to its initial position and time-of-flight and CCD imaging measurements were performed. Because this technique leads to a destruction of the cloud, different hold times, and hence different experimental points, correspond to different experimental runs. This whole procedure was repeated for three final hold points, $x_s \approx 14\,\mu\mathrm{m}$, $29\,\mu\mathrm{m}$ and $72\,\mu\mathrm{m}$. The hold points were estimated by measuring the reference point, where the trap completely opened and all atoms were lost to the surface. However, these reference measurements revealed temperature induced drifts of the surface position by up to $10\,\mu\mathrm{m}$. Hence the hold points were approximate and the uncertainty in the absolute position was the dominant source of error in the experiments. The estimated initial cloud temperatures were 130 nK for the $14\,\mu\mathrm{m}$ and $29\,\mu\mathrm{m}$ hold point and 140 nK for the $72\,\mu\mathrm{m}$ hold point. The initial atom number was 1.4×10^5 in all three cases.

Fig. 3.2 shows the measured data (points) and simulations (curves), which were performed using the same parameters as in the experiments. However,

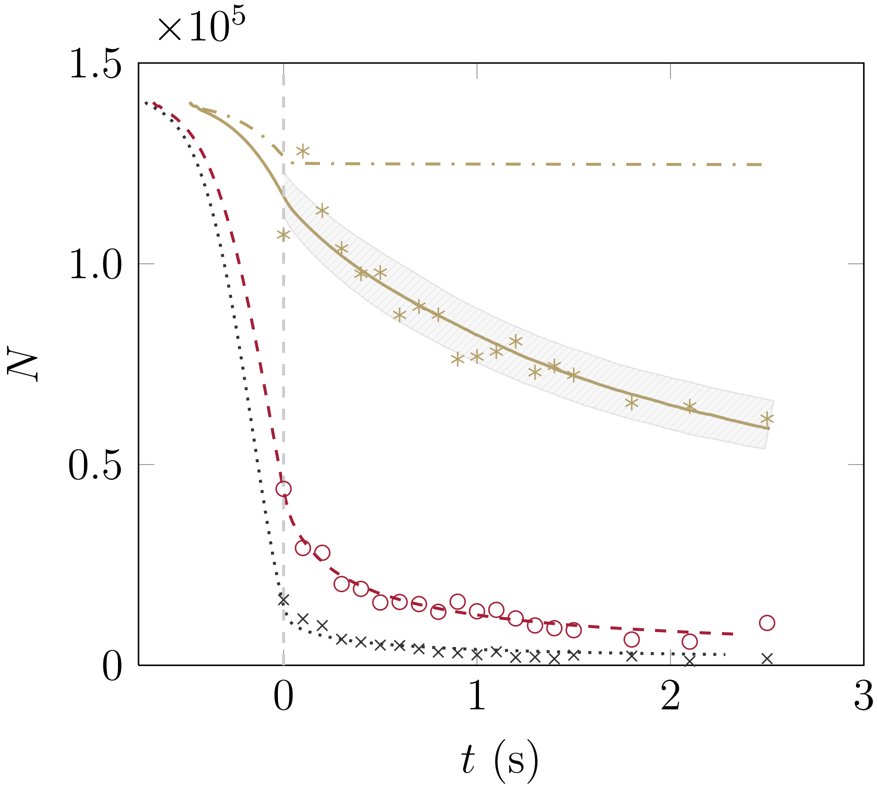

Figure 3.2 – Total atom number, N, against time t for three different trap-surface separations 68.0 μm (gold solid curve), 30.0 μm (red dashed curve) and 15.0 μm (black dotted curve). Points correspond to experimental data and the curves correspond to simulations. The dot-dash gold curve shows a simulation for $x_s = 68.0\,\mu$m without collisions ($C_{12} = C_{22} = 0$). The vertical dashed gray line marks the point when the atom cloud reaches its final hold position. The gray hashed area shows the shift of the curve when the surface position is varied by ±2.5 μm.

because of the uncertainty in the absolute surface position, varying cloud-surface separations were used in the simulations and the best fit was used to model the corresponding experimental loss curve. Thus the simulations served as a calibration tool and the best fits were obtained at a cloud-surface separation of $x_s = 15\,\mu\text{m}$, $x_s = 30\,\mu\text{m}$ and $x_s = 68\,\mu\text{m}$ for the $x_s \approx 14\,\mu\text{m}$, 29 µm and 72 µm curves respectively. In order to help increase the simulation grid resolution, the initial cloud-surface separation was $x_s = 100\,\mu\text{m}$ instead of $x_s = 134\,\mu\text{m}$ leading to different starting points in time for each simulation. However, this did not affect the loss curves, as there was still negligible overlap between the cloud and the surface at the beginning of the simulation and the transport velocities were the same as in the corresponding experiments.

The gold star points and golden curve in Fig. 3.2 correspond to the 68 µm hold position, red open circles and red dashed curve to the 30 µm, and black crosses and black dotted curve to the 14 µm hold position. To illustrate the effect of surface drifts, the gray hashed area shows the shift of the 68 µm curve when the surface position is varied by ±2.5 µm in the simulations. Both, experiments and simulations reveal a non-trivial behavior for the atom losses. As the cloud is transported towards the surface the losses increase, until the point where the final trap position is reached. After that point (denoted by the gray dashed vertical line at $t = 0\,\mathrm{s}$) the losses swiftly reduce. Only atoms with sufficient kinetic energy in the x-direction, which are able to reach the opening point, are lost after the trap reaches its final position. Hence without collisions the atom losses would stop after one trap period t_{trap}.

However, atoms which initially do not have enough kinetic energy in the x-direction may get this energy from other atoms in the gas through collision events. Therefore a slow loss of atoms continues long after the trap has stopped moving. Without collisions these atom losses would not occur, which is illustrated by the gold dot-dashed curve showing the results of a simulation without collisions (i.e. $C_{12} = C_{22} = 0$).

The resulting loss curves are further complicated by the fact that the cloud may change its shape during the time in which atoms are lost to the surface (t_{overlap}). Depending on the thermalization time, t_{therm}, the cloud can be cooled significantly during the evaporation process, thereby reducing its spatial extent and hence the overlap between the cloud and the surface. This lowers the atom losses. Fig. 3.3 reveals a cooling effect during the simulations by showing condensate growth over time for the 68 µm hold position. Approximately 0.5 s after reaching the final position the number of thermal atoms decreases abruptly and the condensate atom number shows the expected, broad s-shaped growth curve [136].

The appearance of a condensate can also be seen by looking at the density profiles during the simulations which are shown in Fig. 3.4. The upper panels show the total cloud densities integrated along the y-direction and the lower panels show cross sections of the thermal cloud density at (a) time $t = 0\,\mathrm{s}$, (b) $t = 1.2\,\mathrm{s}$ and (c) $t = 2.85\,\mathrm{s}$. The simulation starts with a gas above T_c with a thermal density distribution. After $t = 1.2\,\mathrm{s}$ a condensate is clearly visible in the total density, which takes the form of a bimodal distribution. The condensate starts to push thermal atoms out of the trap center resulting in a lower thermal density. After $t = 2.85\,\mathrm{s}$ only a small thermal cloud remains and the depletion of the thermal cloud is clearly visible. Along the long trap axis in the x-direction two density "shoulders" have emerged, which is typical for a ZNG simulation in an anisotropic trap and has also been experimentally

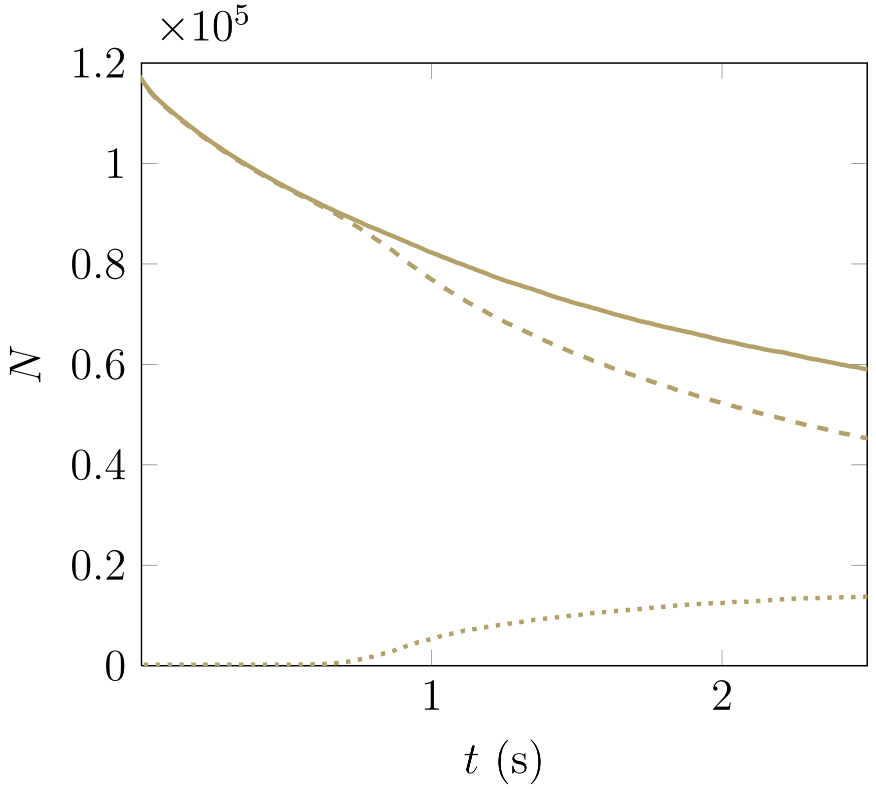

Figure 3.3 – A breakdown of the cloud atom numbers against time for a trap surface separation $x_s = 68.0\,\mu$m (corresponds to gold solid curve in Fig. 3.2) from the point when the cloud reaches its holding position. Solid curve shows the total atom number, dashed curve corresponds to thermal atoms, and the dotted curve to the condensate atom number.

observed in other cold quantum gas systems [154].

The condensate growth is also seen in the experiments and an average of $N_c \approx 9000$ condensate atoms between 1.5 s and 3.0 s at least reveals no serious inconsistencies with a predicted condensate atom number of $N_c \approx 11000$ from the simulation. The same holds true for the 15 µm curve with $N_c \approx 3000$ in the experiments and $N_c \approx 2500$ in the simulation. However, to study condensate growth over time in detail, further work with small atom number fluctuations and surface drifts is needed.

3.4 Distance series

To further investigate the influence of the introduced time scales t_{trap}, t_{overlap} and t_{therm} on the atom losses, it is useful to study final atom numbers after

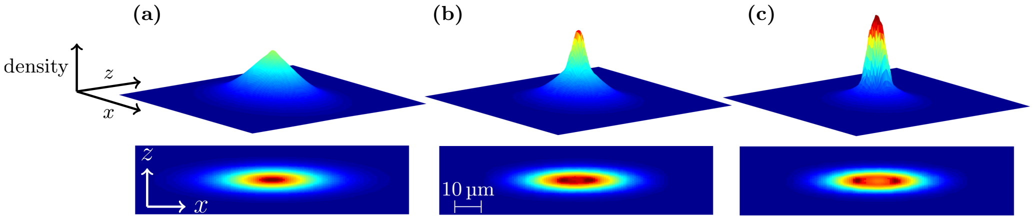

Figure 3.4 – Density profiles of the gas during the 68 µm simulation at (a) time $t = 0$ s, (b) time $t = 1.2$ s and (c) $t = 2.85$ s. The upper panels show the full cloud density, integrated along the y-direction and the lower panels show cross sections of the thermal cloud density through the $y = 0$ plane. Arrows indicate axes and bars indicate scale. In the upper panels, the z-direction has been stretched by a factor of 4 leading to a quadratic profile to improve clarity.

several time series at varying final hold points x_s. The resulting curves are also of particular interest for hybrid system experiments, because they can be used to calibrate the approximate surface position and the cloud temperature [47, 49, 133]. The same trap parameters were used as before in the experiments and reference measurements showed a slightly smaller initial temperature of 115 nK for 1.37×10^5 atoms. Time series measurements with a hold time of $t = 0.6$ s were performed and final surface-trap center distances varied from 110 µm down to 5 µm. The transport time was again 1 s and the starting point was 134 µm.

Gold crosses in Fig. 3.5 show the measured remaining atom number, N, after the full hold time over distance. The red curve shows a full ZNG simulation and the gray curve with open circles a ZNG simulation without collisions ($C_{12} = C_{22} = 0$). The gray hashed area around the red curve shows the error for the full ZNG simulation due to temperature induced surface position drifts of $\pm 2.5\,\mu$m.

As discussed before, collisions may have a big effect on atom losses and the deviation between the two ZNG simulations is significant. This reveals that thermalization plays an important role for the used parameters and in the context of the three dominant time scales this means $t_{\mathrm{trap}} < t_{\mathrm{therm}} \lesssim t_{\mathrm{overlap}}$.

Thermalization effects in this regime are further analyzed by comparing the simulated losses with three different simplified analytical models in Fig. 3.5: an error function (black dash dotted line) and classical energy cutoff models in 1D (black dashed line) and 3D (black dotted line) [153]. The error function yields a description of a truncated Boltzmann distribution in space along one direction

$$N = N_0 \cdot \int_0^\infty \sqrt{\frac{\alpha}{\pi}} e^{-\alpha(x-x_s)^2} dx. \qquad (3.4)$$

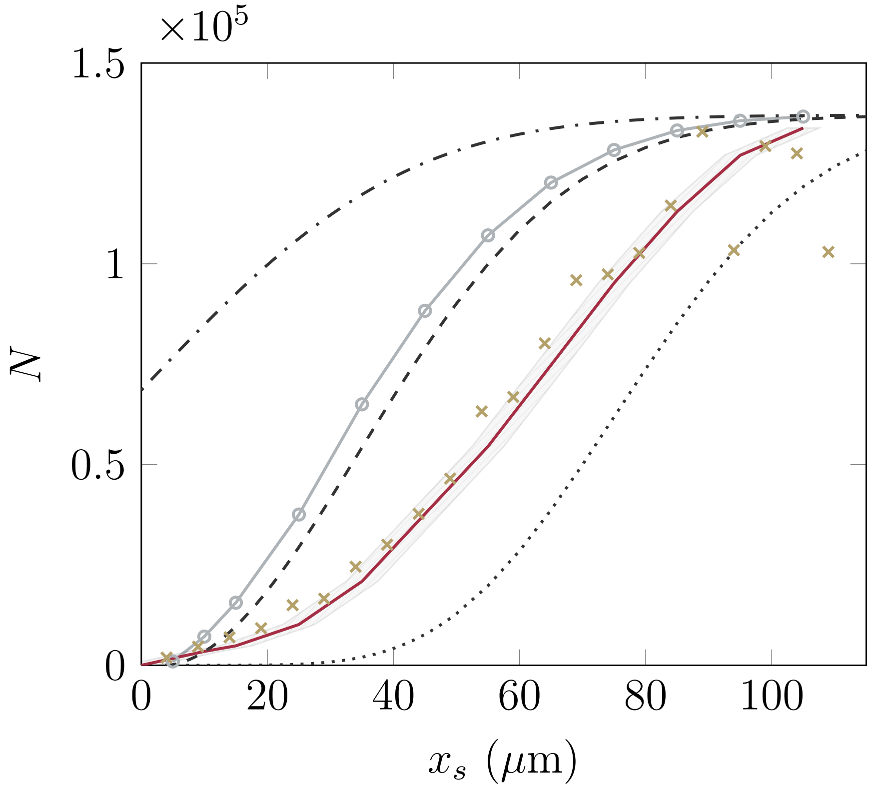

Figure 3.5 – Measured (crosses) and simulated (curves) atom number, N, for a cloud held for 600 ms at a surface for varying trap surface separations. The red curve corresponds to a ZNG simulation with collisions, gray curve with open circles to a simulation without collisions. The black dashed curve comes from a 1D classical model and the dotted curve from a 3D classical model (see text). The black dot-dashed curve is an error function (Eq. (3.4)).

Here N_0 is the initial atom number and $\alpha = m\omega_x^2/2k_\mathrm{B}T$. This models the situation of a cloud which is instantaneously shifted towards the surface and also instantaneously removed. Thus half of the atoms are lost in the case of $x_s = 0$. This is, of course, an idealistic approach. In experiments rapid transport would lead to in-trap sloshing of the cloud, which has dramatic effects on the atom losses. However if t_overlap is very small compared with t_trap and t_therm this model may still lead to reasonable results even for lower transport velocities.

Instead of considering a spatial cutoff it is convenient to compare the losses with a model which describes a cutoff in energy space. These calculations were performed by Günther at the university of Tübingen. As discussed, the Casimir-Polder potential leads to an opening of the trap and the resulting potential can be approximated by a harmonic potential with a finite trap height ΔV. The fraction of remaining atoms $N(\Delta V)/N_0$ is then given by

$$\frac{N(\Delta V)}{N_0} = \frac{\int_0^{\Delta V} D(E) e^{-E/k_B T} dE}{\int_0^{\infty} D(E) e^{-E/k_B T} dE}, \tag{3.5}$$

where $D(E)$ denotes the density of states which takes the form [77]

$$D(E) = \frac{1}{(d-1)!} \frac{E^{d-1}}{\Pi_{k=1}^{d} \omega_k} \tag{3.6}$$

for a harmonic oscillator potential in d dimensions. For $d =$ 1,2,3 this results in

$$\frac{N(\eta)}{N_0} = \begin{cases} 1 - e^{-\eta} & \text{for } d = 1 \\ 1 - (1+\eta) e^{-\eta} & \text{for } d = 2 \\ 1 - (1 + \eta + \frac{1}{2}\eta^2) e^{-\eta} & \text{for } d = 3, \end{cases} \tag{3.7}$$

with the dimensionless parameter $\eta = \Delta V / k_B T$.

In the case of $d = 1$ the model only cuts off atoms which initially have enough energy in the x-direction. That means collisions are neglected completely and no redistribution of velocities and hence no rethermalization can be described with it. In Fig. 3.5 losses in the classical 1D energy cutoff model (dashed black curve) are significantly higher than in the case of the error function approach (dot-dashed black curve), because atoms which are not in contact with the surface (more precisely atoms which are not beyond the point where the trap opens) but have enough energy to reach it within a trap period, t_{trap}, are lost in the energy model but not in the error function model. The 1D energy cutoff calculations correspond to a ZNG simulation without collisions (gray curve with open circles) and the only deviation between the two curves comes from the Bose enhancement in the initial state of the simulation. For a system in which $t_{\text{trap}} \approx t_{\text{overlap}} \ll t_{\text{therm}}$ holds true, this model denotes an appropriate approximation for the atom losses.

An energy cutoff for $d = 3$ takes a redistribution of velocities from the y- and z-direction into the x-direction into account. Atoms which initially do not have enough energy along the x-direction, but with a total energy higher than the trap depth ΔV, are additionally lost. This simulates a redistribution of velocities due to scattering events. However, as the change in total energy of an atom during collisions is not described by the analytical model in Eq. (3.7), it can not simulate an evaporative cooling effect. Hence for a system which is supposed to be evaporatively cooled by the surface, the estimated losses are higher in the 3D model (black dotted curve) than in the experiments, because the model does not account for a change in the cloud's spatial extent during the evaporation. A gas which is cooled by the surface shrinks and therefore reduces its overlap with the surface, which is not considered by the classical 3D model. Hence in contrast to the 1D model the predicted losses are too high when rethermalization and cooling become important. Therefore the 3D model can be seen as an upper bound for the expected losses.

Although the simple models presented here may work in the discussed limiting situations, the relevant experimental systems spend most of the time in an intermediate regime, where there is a complex interplay between the different time scales t_{trap}, t_{overlap} and t_{therm}. As can be seen by the presented experimental data in Fig. 3.2 only a full ZNG simulation can describe losses in these regimes where thermalization plays an important role.

3.5 Condensate Optimization

From an experimental point of view it is desirable to know beforehand how to optimize condensate growth using a surface. But just as with the loss curves, the final condensate atom number depends on many factors. Because a full exploration of the parameter space is not possible, a simplified test system is considered in order to study condensate optimization. Based on an isotropic trap and a fixed transport velocity of the cloud, the final hold position and the trap frequency are varied to explore the effects on condensate formation, which should at least provide some basic guidance on how to obtain large and pure condensates.

Four different trap frequencies were considered in this context $\omega_1 = 2\pi \times 40\,\mathrm{rad\,s^{-1}}$, $\omega_2 = 2\pi \times 80\,\mathrm{rad\,s^{-1}}$, $\omega_3 = 2\pi \times 120\,\mathrm{rad\,s^{-1}}$ and $\omega_4 = 2\pi \times 160\,\mathrm{rad\,s^{-1}}$. For each trap geometry an initial equilibrium state just above T_c is created using 10^5 ^{87}Rb atoms. The cloud was prepared at 2.215 W_l away from the surface, where $W_l = \sqrt{2k_bT/m\omega_i^2}$ is the thermal width of the initial state, leading to different starting positions for each trap frequency ω_i. The cloud was then transported with a velocity $v = 0.1\,\mathrm{mm\,s^{-1}}$ towards the surface and held at a final distance x_s from the surface using a total simulation time of $t = 0.75\,\mathrm{s}$. Fig. 3.6 (a) shows the condensate fraction against different holding distances x_s. For better comparison between the curves, the holding distance is shown in harmonic oscillator units $a_{\text{ho}} = \sqrt{\hbar/m\omega_i}$. Gold solid diamond-shaped points show the condensate fraction for ω_1, gray solid triangles for ω_2, open red circles for ω_3 and black stars for ω_4. In all four cases a fairly pure condensate with up to 80% condensate fraction is formed at relatively close distances to the surface between 4 a_{ho} and 7.5 a_{ho}. However, at these distances, there is already significant overlap between the condensate and the surface leading to loss of condensate atoms. Hence, the resulting condensate atom numbers are relatively small which is shown in Fig. 3.6 (b). Larger condensates are observed further away from the surface with a maximum between $10\,a_{\mathrm{ho}}$ and $15\,a_{\mathrm{ho}}$. In order to maximize the condensate fraction and minimize the remaining thermal atoms at the same time, a holding distance $x_s \sim 10\,a_{\mathrm{ho}}$ appears to be a good compromise. The observed optimal distances were largely independent of transport velocities.

The effect of transport velocity on the condensate formation for the trap with $\omega_3 = 2\pi \times 120\,\mathrm{rad\,s^{-1}}$ is shown in the inset of Fig. 3.6. By reducing the velocity below $0.1\,\mathrm{mm\,s^{-1}}$ the condensate fraction increases from $\sim 60\%$ to up to $\sim 70\%$ but saturates for velocities below $\lesssim 20\,\mathrm{\mu m\,s^{-1}}$. In terms of condensate fraction there is, therefore, little to be gained through lower approach speeds. However, as expected, larger and purer condensates are obtained in traps with higher frequencies due to higher densities and hence smaller thermalization times.

The results in Fig. 3.6 are for a very cold cloud just above T_c. In order to mimic a more realistic starting state when atoms are loaded into a chip trap, further simulations for $\omega_4 = 2\pi \times 160\,\mathrm{rads\,s^{-1}}$ were performed, but with a significantly higher starting temperature of $2\,\mu$K and $2\ \times 10^6$ atoms. A hold position of $10\,a_{\mathrm{ho}}$ was used, as suggested by the results in Fig. 3.6. Due to the higher atom number, condensates of $\sim 90\%$ purity and $\sim 100{,}000$ atoms were observed. It is interesting to note that the ZNG method remains at least qualitatively correct even for this unusually warm starting state. It suggests the primary limitations of the method are the simulation run time and the s-wave scattering approximation, which is valid up to approximately $100\ \mu$K [103].

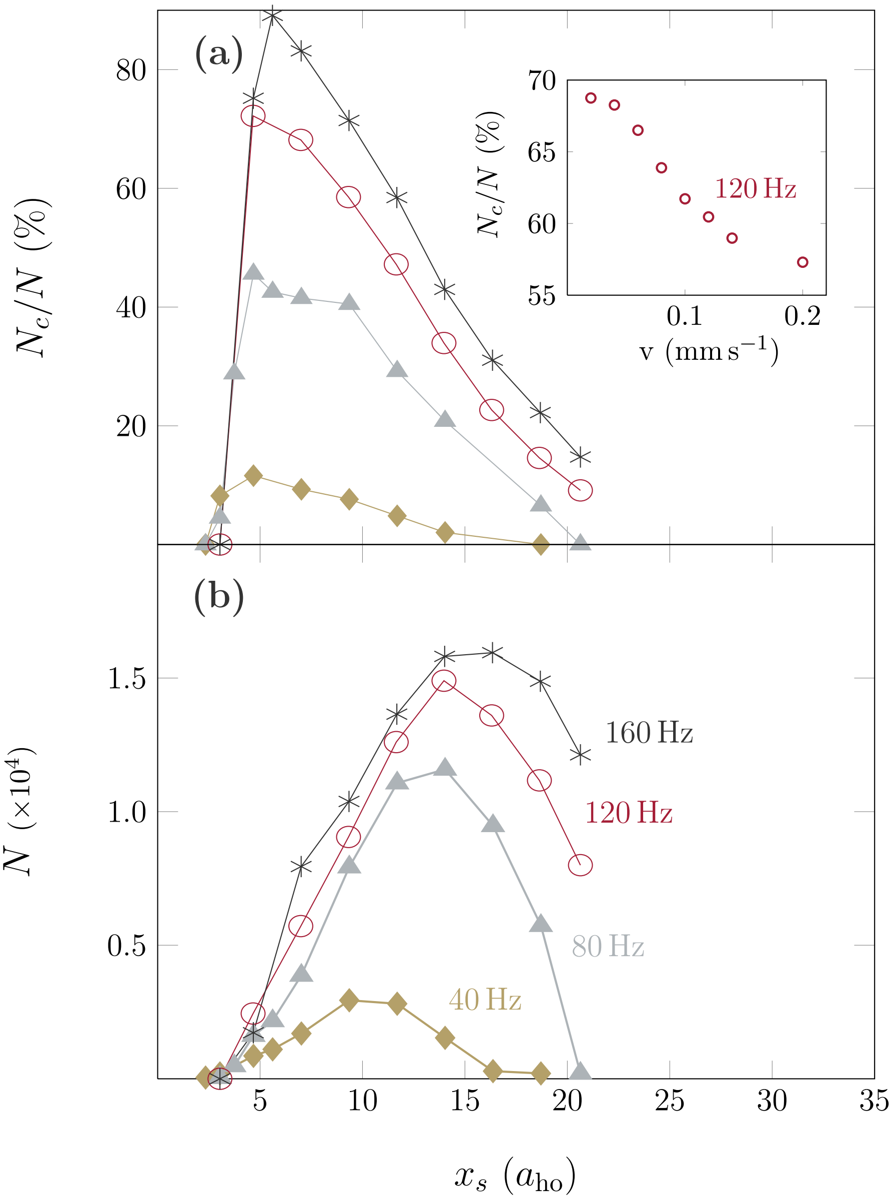

Figure 3.6 – Condensate fraction N/N_c (a) and condensate atom number (b) for different hold points in the case of an isotropic trap, in units of the harmonic oscillator length a_ho. The results for four different trap frequencies $\omega_1 = 2\pi \times 40\,\text{rad}\,\text{s}^{-1}$ (gold diamond points), $\omega_2 = 2\pi \times 80\,\text{rad}\,\text{s}^{-1}$ (gray triangles), $\omega_3 = 2\pi \times 120\,\text{rad}\,\text{s}^{-1}$ (open red circles) and $\omega_4 = 2\pi \times 160\,\text{rad}\,\text{s}^{-1}$ (black stars) are shown. Condensate fractions are highest for these parameters between $4\,a_\text{ho}$ and $7.5\,a_\text{ho}$, whereas the condensate atom number has a maximum between $10\,a_\text{ho}$ and $15\,a_\text{ho}$. The inset in (a) shows condensate fractions plotted against transport velocity for a trap with frequency $\omega_3 = 2\pi \times 120\,\text{rad}\,\text{s}^{-1}$.

3.6 Conclusions

The data shown in this chapter suggests that the ZNG model is capable of describing loss rates of a thermal or a condensed gas in the vicinity of a solid surface, while at the same time leading to reasonable results for condensate growth. Despite the fact that in principle many parameters affect loss curves in front of the surface, different theoretical models suggest that these parameters can be summarized in different time scales t_{therm}, t_{overlap} and t_{therm}. The atom losses in front of the surface are then just governed by the interplay between these time scales. While simpler analytical approaches, like the error function or classical energy cutoff models in 1D or 3D, may only be used in extreme or idealistic situations, the ZNG model yields good results even in an intermediate regime, in which thermalization plays an important role. In experiments the model may therefore be used to calibrate the surface position.

Although resulting loss curves are well described and condensate atom numbers seem to be consistent with experiments, further work is needed to investigate whether all aspects of an emerging condensate can be captured by the method. Time resolved condensate atom numbers are of special interest because quantitative discrepancies between theory and experiments were observed in previous work in the field [136]. This suggests that there are still unexplored effects concerning the BEC phase transition.

Experimental work has also shown that surface evaporation is an efficient route to Bose-Einstein condensation, despite initial concerns in the 1990s that surface cooling might not be competitive compared with free space radio frequency (RF) cooling, because of its limitation to 1D. This was confirmed by the shown simulations. In addition surface cooling may convey certain advantages: the Casimir-Polder potential leads to a very sharp energy “knife”, which together with the position accuracy of the atom chip trap ($<2\,\mathrm{nm}$ [133]) introduces a well controlled energy cutoff, without the need for a RF-signal generator.

As a final remark, the results from section 3.5 can be used to derive a complete cooling scheme of ^{87}Rb atoms in a chip trap within the explored parameter space: as a starting point the cloud should be rapidly transported to a hold position $x_s = 3.0\,W_l$ while avoiding in-trap sloshing. At this point there is negligible overlap between the cloud and the surface. The trap should then be moved with a velocity $v \lesssim 0.1\,\mathrm{mm\,s^{-1}}$ to a final hold position at about $10\,a_{\text{ho}}$. In this way a large and relatively pure condensate can be achieved even for low trap frequencies in a time which is comparable to that of conventional RF cooling [134]. In order to obtain purer or larger condensates the cloud should be shifted closer to, or further away from the surface, respectively.

Chapter 4

Ion buffer gas cooling

Over the last two decades not only the manipulation of cold neutral atoms has experienced tremendous progress but also the cooling, trapping and manipulation of charged particles. In experiments, so called Paul traps, which create an oscillating saddle-shaped potential for any charged particle, have allowed researchers to store cold, single, positively charged ions [155, 156]. Combined with laser cooling techniques this offered the possibility to cool the ions down to the zero-point energy [157]. Since then, cold ions have been a promising system for the realization of a scalable quantum computer [31–33, 158], as they allow for a deterministic entanglement of quantum states and they can be stored for long durations, without being perturbed by their environment. This provides long coherence times and the accessibility needed for quantum computation [159].

Despite the experimental progress in trapping ions and neutral cold atoms, the two fields have been largely separated for a long time. However, a hybrid system combining both components may yield the opportunity to study new ultra-cold quantum mechanical effects in a very controlled way. It has already been theoretically predicted that the charge transfer radius between the ion and a neutral atom becomes greater than the s-wave scattering length in the case of very low temperatures [160]. This would lead to a diffusion of the charge through the whole cloud, because electrons would be able to hop from atoms to ions resulting in a conductive cloud. Similar theoretical work predicted the creation of mesoscopic molecular ions in atom-ion systems [161], where a large number of polarized neutral atoms are loosely bound due to the $1/r^4$ potential surrounding the ion.

Additionally, because the ion represents a small impurity when immersed in a neutral cold gas, polaron physics, which has already been studied theoretically in solid-state physics [162] or in cold gases [163, 164], may be explored experimentally due to the high controllability of the ion. The polaron, a quasi particle consisting of the impurity and the coupling to its surrounding environment, may even be in the strong-coupling regime in the case of an atom-ion system, which could not be realized in any other system so far [56]. This strong coupling could lead to a self-trapping and localization of the polaron (Fröhlich polaron) [57].

Furthermore, ions are believed to play a crucial role for cold chemical reactions in interstellar gases [165, 166] and may explain unexpected molecule formation in diffuse and dense clouds inside our Milky Way galaxy. An atom-ion system is a suitable test bed for theoretical models describing these chemical reactions.

However, although an ion confined in a Paul trap in combination with a cold buffer gas seems to be a promising system for these effects, there are certain limitations, which prevent the experiments from reaching the regimes of interest. Because the Paul trap creates a rotating saddle instead of a simple harmonic oscillator potential, the ion undergoes an additional fast oscillating motion, the so-called micromotion. This micromotion leads to heating and coherence loss and its minimization is an important challenge not only in the context of hybrid systems but in every experiment involving a Paul trap. While a certain micromotion, which is induced by the ion's movement in the trapping potential, is inevitable, the excess micromotion, coming from electric stray fields can in principle be compensated.

However, in order to do so, another experimental challenge arises. In most setups the excess micromotion is not known and hard to measure, making a compensation impossible. Hence, to reduce the excess micromotion, yielding the possibility to reach very low temperature regimes for the ion, a tool is needed to extract detailed information about the ion's energy.

In this chapter a numerical description of a single trapped ion in a thermal atom cloud is discussed. The atom cloud is modeled by a quantum Boltzmann equation but instead of coupling it to a generalized GPE via a collision integral, as in the case of the ZNG model, collision probabilities between the ion and thermal atoms are calculated using multiple partial waves. As in the case of the surface evaporation the simulation results are first compared with experimental data. It is shown that the simulations are capable of describing atom-loss curves within the given error bars. Furthermore, a method that allows one to use the thermal cloud as a calorimeter for the ion is presented. This enables the determination of the unknown excess micromotion in the experiments. The chapter proceeds by investigating so far unexplored non-equilibrium properties of the system.

4.1 Interactions between an ion and a neutral atom

The interactions between an ion and a neutral atom are governed by the long-range polarization potential. The electric field of the ion shifts the charges in a neutral atom resulting in an attractive force. This electric field can be approximated by that of a point charge [167], and for a singly charged ion it becomes

$$E(r) = \frac{e}{4\pi\epsilon_0 r^2}, \tag{4.1}$$

where e is the elementary charge, ϵ_0 is the vacuum permittivity and r the distance of the neutral atom from the ion.

The charge separation in a neutral atom at a distance r leads to a dipole moment $p(r)$

$$p(r) = 4\pi\epsilon_0 \alpha E(r), \tag{4.2}$$

which depends on the polarizability α of the atom. The potential of an electric dipole in an electric field is given by

$$V(r) = -\frac{1}{2} p(r) E(r), \tag{4.3}$$

and by substituting the expressions from Eq. (4.1) and Eq. (4.2) into Eq. (4.3) the resulting potential becomes

$$V(r) = -\frac{C_4}{r^4}, \tag{4.4}$$

with $C_4 = \alpha e^2/(8\pi\epsilon_0)$. The $1/r^4$ dependence leads to a long-range interaction between atoms and ions with an energy-dependent elastic cross section σ_{ai}, that is usually orders of magnitude higher compared with the cross section for the scattering between two neutral atoms [168].

It should be noted that only elastic-scattering processes are considered in this chapter. In general inelastic charge-transfer collisions may also happen in an atom-ion system. However, neglecting these inelastic processes is both convenient and justifiable as they occur very rarely.

4.1.1 Semi-classical model for the differential cross section

The full differential cross section between an ion and an atom for a given collision energy E_{coll} can be numerically calculated using the partial wave expansion in a semi-classical approach. The partial wave expansion leads to a differential cross section of the form [169]

$$\frac{d\sigma}{d\Omega} = \frac{1}{k^2}\left|\sum_{l=0}^{\infty}(2l+1)e^{i\eta_l}\sin(\eta_l)P_l(\cos(\theta))\right|^2, \tag{4.5}$$

where θ is the deflection angle and P_l denotes the l-th Legendre polynomial with l being the angular momentum quantum number of the partial wave. The collision momentum is $\hbar k = \sqrt{2\mu E_{\text{coll}}}$, where μ is the reduced mass of the atom-ion system

$$\mu = \frac{m_{\text{ion}}m_{\text{n}}}{m_{\text{n}} + m_{\text{ion}}}, \tag{4.6}$$

with m_{n} the mass of the neutral atom and m_{ion} the mass of the ion. The scattering phase η_l, which depends on the scattering potential, can be obtained by solving the radial Schrödinger equation containing a centrifugal barrier term $\hbar^2 l(l+1)/(2\mu R^2)$, with R the distance from the origin in the center-of-mass frame.

Because the centrifugal barrier increases with angular momentum l this term dominates for higher partial-wave numbers and the phase shift η_l is only given by the long-range interaction potential (Eq. (4.4)). However lower partial waves with $l < l_0 = 1/\hbar\sqrt{2\mu\sqrt{2C_4E_{\text{coll}}}}$ have a collision energy higher than the centrifugal barrier and the inner structure of the potential well contributes to the scattering phase. Because this inner structure is typically not known, scattering phases for $l < l_0$ are assumed to be uniformly distributed within $[0,2\pi)$. Each partial wave with $l < l_0$ therefore contributes $\sigma_l = 2\pi l/k^2$ to the total cross section [170].

When tunneling effects are neglected, the phase shift for higher partial waves with $l > l_0$ can be approximated using a semi-classical model [171, 172]

$$\eta_l = -\frac{\mu}{\hbar}\int_{R_0}^{\infty}\frac{V(R)}{\sqrt{k^2 - ((l+1/2)^2/R^2)}}dR, \tag{4.7}$$

with

$$R_0 = \frac{l+1/2}{k}. \tag{4.8}$$

For the long-range polarization potential in Eq. (4.4) the phase shift can alternatively be approximated with the expression [168]

$$\eta_l = \frac{\pi\mu^2 C_4 E_{\text{coll}}}{4\hbar^4 l^3}. \tag{4.9}$$

In order to numerically calculate the differential cross section for a given collision energy the approach outlined in [170] was used. The sum in Eq. (4.5) was performed with up to 10000 partial waves. This was done by using 100 sets of random scattering phases η_l for each partial wave with $l < l_0$ and using Eq. (4.9) for partial waves with $l > l_0$.

With the help of the determined differential cross section, $\frac{d\sigma}{d\Omega}$, a collision probability distribution $I(\theta{,}E_{\text{coll}})$ can be calculated, which only depends on the collision energy, E_{coll}, and the deflection angle, θ, for a given atom species

$$I(\theta{,}E_{\text{coll}}) = \frac{d\sigma}{d\theta} = \int_0^{2\pi} \frac{d\sigma}{d\Omega} \sin(\theta) d\phi = 2\pi \sin(\theta) \frac{d\sigma}{d\Omega}. \tag{4.10}$$

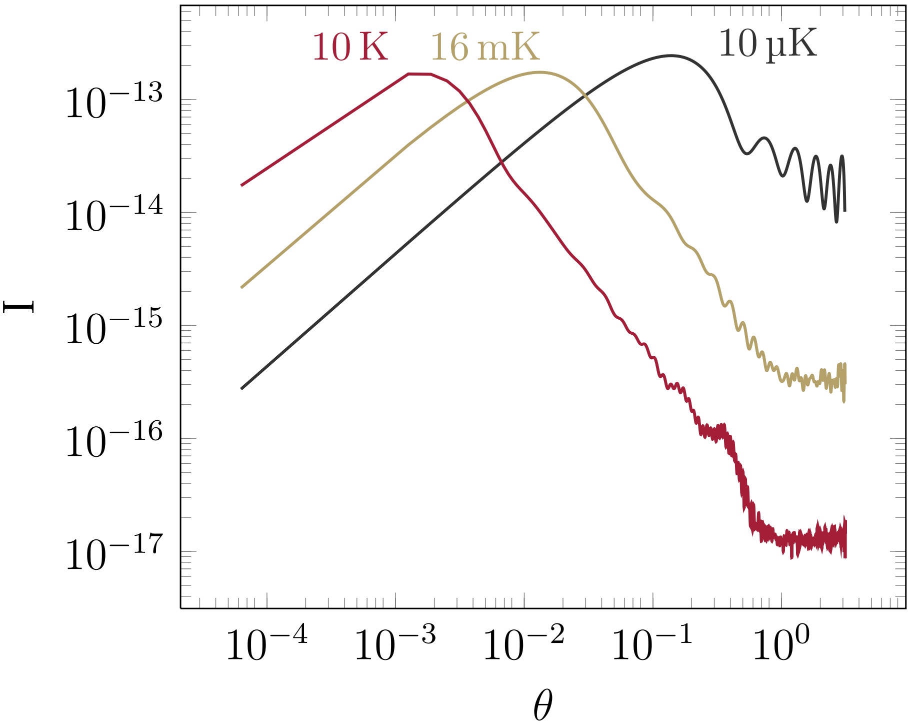

Figure 4.1 – Probability distribution $I(\theta{,}E_{\text{coll}})$ over the deflection angle θ for three different collision energies $E_{\text{coll}} = 10\,\text{K} \times k_{\text{B}}$, $E_{\text{coll}} = 16\,\text{mK} \times k_{\text{B}}$ and $E_{\text{coll}} = 10\,\mu\text{K} \times k_{\text{B}}$ for the case of a $^{87}\text{Rb}^+$ ion colliding with a neutral ^{87}Rb atom. When normalizing the collision probability to unity the forward-scattering peak becomes more pronounced for higher collision energies.

In Fig. 4.1 collision probabilities over the deflection angle θ are shown for three different collision energies $E_{\text{coll}} = 10\,\text{K} \times k_{\text{B}}$, $E_{\text{coll}} = 16\,\text{mK} \times k_{\text{B}}$ and $E_{\text{coll}} = 10\,\mu\text{K} \times k_{\text{B}}$ for a $^{87}\text{Rb}^+$ ion interacting with a neutral ^{87}Rb atom. The double logarithmic scale reveals a forward-scattering peak, leading to high collision probabilities for small deflection angles. These peaks get more pronounced for high collision energies when the collision probability is normalized to unity. A hot ion in a cold atom cloud is therefore involved in many so-called glancing collisions with a small deflection angle. Although they have little effect on the ion's trajectory, they have a big influence on the temperature and losses from the cloud and cannot be neglected in a detailed description. To model the cross section in the simulations, fifty collision probability distributions were calculated in this way for collision energies between $E_\mathrm{coll} = 10\,\mathrm{K} \times k_\mathrm{B}$ and $E_\mathrm{coll} = 10\,\mu\mathrm{K} \times k_\mathrm{B}$.

4.2 Ion motion in a Paul trap

The Earnshaw theorem states that there are no local minima of an electrostatic potential in free space [173]. Therefore a charged particle can not be trapped by electro-static forces alone. In a Paul trap this problem is solved by combining an electro-static field with a radio-frequency (RF) driven, oscillating electric quadrupole field. In this way a rotating saddle potential can be achieved leading to an effective potential, which is similar to that of a three-dimensional harmonic oscillator. This effective potential is sketched in Fig. 4.2.

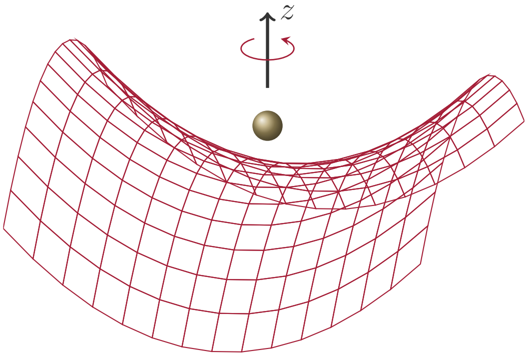

Figure 4.2 – Sketch of the oscillating trapping potential created by a Paul trap.

The total potential of a linear Paul trap, Φ_tot, consisting of a superposition of the oscillating potential term, Φ_RF, and the static potential term, Φ_static, is given by the expression [56, 174]

$$\begin{aligned}\Phi_{\text{tot}} =&\Phi_{\text{RF}} + \Phi_{\text{static}}\\ =&\frac{V_0}{2}\left[(1+\frac{x^2-y^2}{R'^2_{\text{rad}}}-\frac{z^2}{R'^2_z})\cos(\Omega_D t)\right]+\frac{m_{\text{ion}}}{2Q}\omega^2_{\text{ion},z}\left(z^2-\frac{1}{2}(x^2+y^2)\right),\end{aligned} \tag{4.11}$$

where V_0 is the RF-voltage amplitude, which oscillates with a frequency Ω_D. Q is the charge and m_{ion} the mass of the ion. R'_{rad} and R'_z denote the effective radial and axial extension of the trap. The classical motion of an ion in the total potential in Eq. (4.11) is given by the Mathieu equations

$$\frac{\partial^2 r_i}{\partial t^2}+(a_i+2q_i\cos(\Omega_D t))\frac{\Omega_D^2}{4}r_i=0, \tag{4.12}$$

in three different spatial dimensions $i = x,y,z$. The trap-specific parameters q_i and a_i depend on the applied voltages, the ion species and the trap geometry. For $|a_i| \ll 1$ and $q_i \ll 1$ the motion of the ion can be approximately split into two parts - a slow secular harmonic motion $\mathbf{r}_{\text{sec}}$ and a fast oscillating micromotion. This is often referred to as the pseudo-potential approximation [175, 176]. The slow secular term describes the motion of a particle with energies E_i in a harmonic potential with trapping frequencies $\omega_{\text{ion},i}$

$$r_{\text{sec},i}=\frac{1}{\omega_{\text{ion},i}}\sqrt{\frac{2E_i}{m_{\text{ion}}}}\sin(\omega_{\text{ion},i}t+\varphi_i), \tag{4.13}$$

where φ_i are the oscillation phases.

The fast micromotion is driven by the oscillating electrode voltages with frequency Ω_D and is due to the displacement of the ion from the trap center. On the one hand, this displacement occurs because of the slow secular motion and on the other hand, small offset fields drag the ion away from the trap center even for an ion at rest. This second micromotion resulting from stray electric fields is called the excess micromotion, $\mathbf{v}_{\text{mm,excess}}$, and it sets a lower limit for the ion's energy in a Paul trap. The total micromotion velocity can be written in the form

$$\begin{aligned}\mathbf{v}_{\text{mm}} =&(\mathbf{v}_{\text{mm,sec}}+\mathbf{v}_{\text{mm,excess}})\\ =&\begin{pmatrix} q_x\cdot(r_{\text{sec,x}}(t)+\Delta r_x)\\ q_y\cdot(-r_{\text{sec,y}}(t)-\Delta r_y)\\ q_z\cdot(r_{\text{sec,z}}(t)+\Delta r_z)\end{pmatrix}\frac{\Omega_D}{2}\cos(\Omega_D t),\end{aligned} \tag{4.14}$$

with Δr_i being the displacement as a result of electric stray fields and $\mathbf{v}_{\text{mm,sec}}$ the micromotion resulting from the secular motion of the ion.

4.3 Numerical realization of atom-ion collisions

To study the dynamics of an ion in a cold but thermal buffer gas, the DSMC techniques described in chapter 2 for solving the quantum Boltzmann equation were used, in order to model the thermal cloud. But instead of coupling the Boltzmann equation to a generalized GPE via the C_{12} collision integral, as in the case of the ZNG model, another collision term, C_{ion}, describing scattering between neutral atoms and the ion is considered. The time evolution of the thermal-cloud distribution function then becomes

$$\frac{\partial f(\mathbf{r},\mathbf{p},t)}{\partial t} + \frac{p}{m} \cdot \nabla_{\mathbf{r}} f(\mathbf{r},\mathbf{p},t) - \nabla U \cdot \nabla_{\mathbf{p}} f(\mathbf{r},\mathbf{p},t) = C_{\text{ion}} + C_{22}[f]. \tag{4.15}$$

This new scattering term is calculated using a Monte Carlo method described in [170]. In this scheme an upper bound for the time-dependent collision rate, Γ_{max}, is calculated leading to an estimated time interval t_{min}, after which a collision is likely to happen.

In detail the algorithm works as follows: the collision probability distribution, $P(t)$, gives the probability for an event to take place after a time t and it takes the form

$$P(t) = \Gamma(t) \exp\left(-\int_0^t \Gamma(t_1) dt_1\right) \tag{4.16}$$

for a time-dependent scattering rate $\Gamma(t)$. In the case of an ion in a thermal buffer gas this rate is given by the thermal cloud density $\tilde{n}(\mathbf{r})$, the total scattering cross section $\sigma(E_{\text{coll}})$ for a collision with energy E_{coll} and the velocity of the ion $v_{\text{ion}}(t)$

$$\Gamma(t) = \tilde{n}(\mathbf{r}) \sigma(E_{\text{coll}}) v_{\text{ion}}(t). \tag{4.17}$$

An upper bound for $\Gamma(t)$ can be found by using the neutral-cloud peak density $\tilde{n}_{\text{max}}$ and the highest possible total ion velocity $v_{\text{ion,max}}$. The highest ion velocity also determines the highest collision energy $E_{\text{coll,max}}$ (when neglecting the neutral atom's velocity) and the upper bound for $\Gamma(t)$ becomes

$$\Gamma_{\text{max}} = \tilde{n}_{\text{max}} \sigma(E_{\text{coll,max}}) v_{\text{ion,max}}. \tag{4.18}$$

Using inverse transform sampling, a collision time, t_{min}, corresponding to this Γ_{max} can be estimated

$$t_{\text{min}} = -\frac{1}{\Gamma_{\text{max}}} \cdot \log(p_1), \tag{4.19}$$

with p_1 being a uniformly distributed random number between 0 and 1. The whole system is then iterated in time using t_{min}. For the thermal cloud this is done by the DSMC method; the analytical expressions in Eq. (4.13) and Eq. (4.14) in the pseudo-potential approximation are used to iterate the ion's properties.[1] Because t_{min} is a collision time estimated by an upper bound for the collision rate, a rejection method is then used to check whether a collision should take place after t_{min} for the actual collision rate $\Gamma(t)$, which is lower. For that purpose a rescaled rate, $\gamma(t + t_{\text{min}}) = \Gamma(t + t_{\text{min}})/\Gamma_{\text{max}}$, is compared with another uniformly distributed random number p_2. If $p_2 > \gamma(t + t_{\text{min}})$ the collision is rejected, a new collision time t_{min} is calculated and the system is iterated accordingly. If $p_2 < \gamma(t + t_{\text{min}})$ a collision takes place.

In previous work on an ion in a gas [170] the thermal cloud was modeled by a simple, classical Boltzmann distribution with instantaneous thermalization. An atom-ion collision was implemented by updating the ion's properties according to the deflection angle θ, while neglecting the velocity of the neutral atom. In this work a more sophisticated approach, which takes the neutral atom velocity into account and allows for the description of non-equilibirum effects in the thermal cloud, is used. This works as follows: because the DSMC uses test particles to solve the quantum Boltzmann equation, a collision partner is sought within the collision cell where the ion resides. The ion and the test particle velocities are transformed into the center-of-mass frame, where a deflection angle θ is determined with the help of a rejection method and the corresponding cross section. Cross sections for a range of collision energies are calculated only once and can be used for all simulations with the corresponding atom-ion species. The velocities of the ion and of the test particle are updated taking energy and momentum conservation into account. This changes the secular energies E_i and the phases φ_i of the ion, while leaving the micromotion velocity and position of the ion unaltered. This is convenient because the micromotion is driven by external fields, and it is therefore not affected by collisions.

However, the described method may cause a numerical inconvenience. In the case of a dilute cold gas the test particle number is usually bigger than the actual physical particle number. Therefore when an ion-atom collision takes place, the ion has to scatter with an ensemble of $1/\gamma$ test particles representing a physical atom. Because the ion's velocity has to take a specific value, one atom-ion collision pair is chosen randomly to determine the ion's properties after the collision. However, the velocities of the test particles are adjusted using the actual corresponding center-of-mass frames with a given

---

[1] A numerical iteration of the ion's trajectory would be computationally expensive due to the high Paul trap frequencies, which would demand small numerical time steps.

scattering angle. In this way energy and momentum is only conserved in a statistical sense, but it should provide a more realistic description of the system, compared with a model that neglects the neutral atom's velocity.

Another numerical problem arises from the comparatively high temperatures of the initial states of the thermal clouds. Some of the clouds considered in this chapter have an initial temperature, which is much higher than the critical temperature T_c. The assumption that the chemical potential vanishes (i.e. $\mu = 0$) is not appropriate for these states and would lead to unphysically high trap-center densities. Therefore the chemical potential is estimated beforehand using the constraint [76]

$$N = \sum_{i=0} \frac{1}{e^{\beta(\epsilon_i - \mu)} - 1}. \tag{4.20}$$

The constraint states that the total particle number N is given by the sum over all expected particle numbers of state i with energy ϵ_i. In the case of an ideal gas in a harmonic trap Eq. (4.20) becomes

$$N = \sum_{k,l,m=0} \frac{1}{e^{\beta(\epsilon_{klm} - \mu)} - 1}, \tag{4.21}$$

with

$$\epsilon_{klm} = \hbar\omega_x(n_k + \frac{1}{2}) + \hbar\omega_y(n_l + \frac{1}{2}) + \hbar\omega_z(n_m + \frac{1}{2}). \tag{4.22}$$

In order to calculate the chemical potential μ the sum in Eq. (4.21) was performed over 8×10^6 modes for a given temperature T. The chemical potential then was used to set up an Hartree-Fock equilibrium state (see Sec. 2.1).

4.4 Steady-state energy and excess micromotion

A hot ion in a cold atom cloud is cooled by collisions with the cloud, which therefore acts as a buffer gas. However, after an initial cool-down phase the ion's energy fluctuates around a so-called steady-state energy. For a relatively hot ion and negligible neutral-atom velocities this energy is given by the trap geometry, the atom-ion species and most importantly the excess micromotion. The micromotion couples to the ion's secular motion in each collision event and sets a lower limit for the steady-state energy.

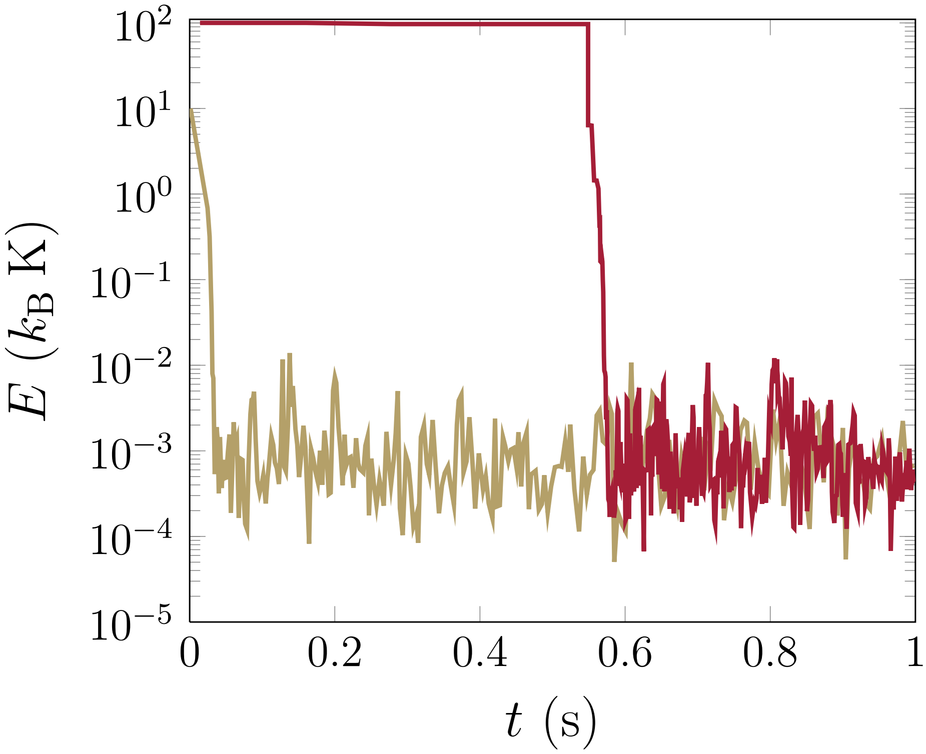

Figure 4.3 – Simulated ion energy over time for two different initial energies $E_{\text{init}} = 10\,\text{K} \times k_\text{B}$ (gold curve) and $E_{\text{init}} = 100\,\text{K} \times k_\text{B}$ (red curve). The excess micromotion energy in both cases was $E_{\text{eMM}} = 1.0\,\text{mK} \times k_\text{B}$. After an initial cool-down the energy fluctuates around a steady-state energy of about $E_{\text{steady}} \approx 1.18 \times E_{\text{eMM}}$.

A typical cool-down simulation is illustrated in Fig. 4.3 for a $^{138}\text{Ba}^+$ in a neutral cloud consisting of 13500 ^{87}Rb atoms at a temperature $T = 205\,\text{nK}$ for two different initial ion energies, $E_{\text{ion}} = 10\,\text{K} \times k_\text{B}$ (gold curve) and $E_{\text{ion}} = 100\,\text{K} \times k_\text{B}$ (red curve). The ion was confined in a linear Paul trap with trapping frequencies $\omega_{x,\text{ion}} = \omega_{y,\text{ion}} = 2\pi \times 122 \times 10^3\,\text{rad}\,\text{s}^{-1}$, $\omega_{z,\text{ion}} = 2\pi \times 15.8 \times 10^3\,\text{rad}\,\text{s}^{-1}$ and a driving frequency $\Omega_D = 2\pi \times 4.214 \times 10^6\,\text{rad}\,\text{s}^{-1}$. In both cases the excess micromotion was chosen to be $E_{\text{eMM}} = 1\,\text{mK} \times k_\text{B}$. Trapping frequencies for the neutral cloud were $\omega_z = 2\pi \times 28\,\text{rad}\,\text{s}^{-1}$, $\omega_y = 2\pi \times 134\,\text{rad}\,\text{s}^{-1}$ and $\omega_x = 2\pi \times 144\,\text{rad}\,\text{s}^{-1}$. The parameters are chosen to model real experiments in the group of Prof. Denschlag in Ulm.

The hot ion (red curve) remains close to its starting energy of $E_{\text{ion}} = 100\,\text{K} \times k_\text{B}$ for a relatively long time, before it undergoes a major collision event, which reduces the energy significantly. For such high secular energies the radius of the ion in the Paul trap is much higher than the extent of the thermal cloud, thereby reducing the effective overlap between the ion's trajectory and the cloud. This leads to few collisions at the beginning of the simulation. In addition the scattering peak for small deflection angles is more pronounced for higher ion energies. As a result collisions are likely to be glancing collisions with a small deflection angle. Glancing collisions have little effect on the ion's energy, and, as can be seen in Fig. 4.3 the ion cooling is dominated by only a few collisions with a high energy transfer and hence big deflection angles. As a consequence, the high ion-trajectory radius and the higher scattering peak for small deflection angles both increase the cooling time of the ion. In contrast, for a starting energy of $E_{\mathrm{ion}} = 10\,\mathrm{K} \times k_{\mathrm{B}}$ (gold curve) the initial overlap between the cloud and the ion's trajectory is increased and the smaller energy also reduces the ratio of glancing collisions. This leads to a cooling time, which is approximately an order of magnitude lower compared with the cooling time of the hot ion.

After cooling down, the ion's energy undergoes rapid fluctuations by up to two orders of magnitude on time scales of about 10 ms. The steady-state energy, E_{steady}, was extracted by taking the mean energy value after cooling and was comparable to the ion's micromotion in this setup ($E_{\mathrm{steady}} \approx 1.18 \times E_{\mathrm{eMM}}$).

4.5 Atom losses and excess micromotion

Collisions between the ion and the neutral cloud lead to atom losses from the trap. A laser-cooled ion in a Paul trap is usually much hotter than a neutral bosonic cloud close to T_c and the energy transfer in a scattering event often results in an atom leaving the trap, even for small deflection angles. In this section, simulated atom-loss curves are compared with experimental results. As in the case of the surface evaporation problem this demonstrates the applicability of the model. In addition, it is shown how the simulation curves can be used as a calorimeter for the ion, yielding a possibility to directly measure the excess micromotion and the steady-state energy in the experiments.

The experiments were done in the group of Prof. Denschlag in Ulm and were mostly performed by Härter and Krükow using the setup described in [56]. Single $^{87}\mathrm{Rb}^+$ or $^{138}\mathrm{Ba}^+$ ions in a Paul trap were immersed in a neutral $^{87}\mathrm{Rb}$ cloud. By applying external electro-static fields, a well known, additional excess micromotion was added to an unknown inherent excess micromotion, E_{Res}, to explore the effects on the atom losses.

Figure 4.4 shows remaining atoms for a $^{87}\mathrm{Rb}^+$ ion in a thermal atom cloud with initially 10870 atoms for different excess micromotions over an

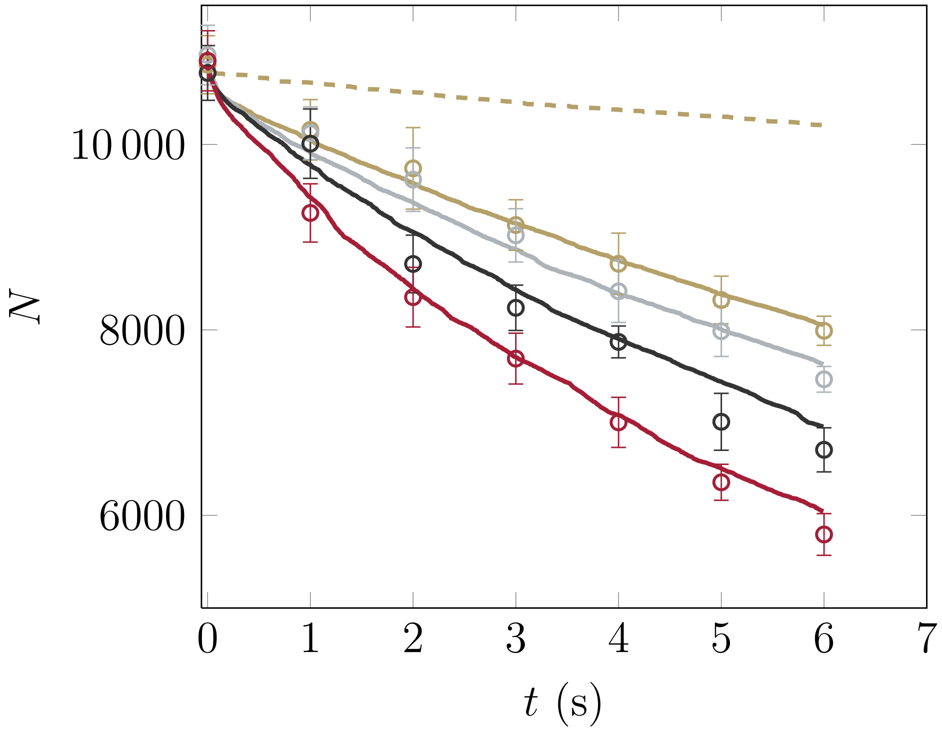

Figure 4.4 – Remaining thermal atoms, N, over interaction time t for a $^{87}\mathrm{Rb}^{+}$ ion in a thermal gas of initially 10870 neutral $^{87}\mathrm{Rb}$ atoms. Different colors correspond to different artificial excess-micromotion energies, which were produced by well controlled electro-static fields, with values $E_{\mathrm{mm}} = 0.270\,\mu\mathrm{K} \times k_{\mathrm{B}}$ (gold curve), $E_{\mathrm{mm}} = 1.04\,\mathrm{mK} \times k_{\mathrm{B}}$ (gray curve), $E_{\mathrm{mm}} = 8.9\,\mathrm{mK} \times k_{\mathrm{B}}$ (black curve) and $E_{\mathrm{mm}} = 43.8\,\mathrm{mK} \times k_{\mathrm{B}}$ (red curve). The data points corresponding to $E_{\mathrm{mm}} = 0.270\,\mu\mathrm{K} \times k_{\mathrm{B}}$ were used to estimate the unknown residual excess micromotion, E_{Res}, and the best fit was obtained with $E_{\mathrm{Res}} = 500\,\mu\mathrm{K} \times k_{\mathrm{B}}$. The dashed gold curve shows a simulation with $E_{\mathrm{mm}} = 0.270\,\mu\mathrm{K} \times k_{\mathrm{B}}$ and no residual micromotion.

interaction time t. Trapping frequencies for the cloud were $\omega_x = \omega_y = 2\pi \times 136\,\mathrm{rad\,s^{-1}}$ and $\omega_z = 2\pi \times 40\,\mathrm{rad\,s^{-1}}$. The ion was confined in a linear Paul trap with frequencies $\omega_{x,\mathrm{ion}} = \omega_{y,\mathrm{ion}} = 2\pi \times 350 \times 10^{3}\,\mathrm{rad\,s^{-1}}$, $\omega_{z,\mathrm{ion}} = 2\pi \times 70 \times 10^{3}\,\mathrm{rad\,s^{-1}}$ and Mathieu parameters $q_x = -q_y = 0.24$, and $q_z = -0.043 \times q_x$. In this and in all further setups, the ion trap center coincided with the trap center of the neutral cloud. The different curves in Fig. 4.4 correspond to different electro-static fields, which add a well defined, artificial excess micromotion energy to the system. The resulting energies were $E_{\mathrm{mm}} = 0.270\,\mu\mathrm{K} \times k_{\mathrm{B}}$ (gold curve), $E_{\mathrm{mm}} = 1.04\,\mathrm{mK} \times k_{\mathrm{B}}$ (gray curve), $E_{\mathrm{mm}} = 8.9\,\mathrm{mK} \times k_{\mathrm{B}}$ (black curve) and $E_{\mathrm{mm}} = 43.8\,\mathrm{mK} \times k_{\mathrm{B}}$ (red curve). The initial ion energy was $E_{\text{init}} = 6\,\text{K} \times k_{\text{B}}$, equally distributed in all three dimensions. As mentioned above, another unknown excess micromotion, E_{Res}, the result of electric stray fields in the middle of the Paul trap, was present in the experiments. This residual energy was estimated to be below $1\,\text{mK} \times k_{\text{B}}$ and therefore has little effect on losses for high electro-static fields (black and red open circles). However, it dominates the losses for the smallest electric field (gold data points). Thus, by fitting the simulation for the smallest electric field to the corresponding data points (gold open circles) for varying E_{Res}, the unknown residual energy in the experiments was determined. Independent of E_{Res}, the measured data for high electro-static fields (black and red open circles) could be described using the experimental parameters. The simulations shown were performed using $E_{\text{Res}} = 500\,\mu\text{K} \times k_{\text{B}}$ and the figure reveals good agreement between theory and experiments in all four cases.

The conclusions which can be drawn from Fig. 4.4 are hence twofold: the curves corresponding to higher excess micromotions (red and black solid curves) show that the method is capable of describing the interactions between an ion and a thermal cloud in the experiments within the given, small, experimental error bars, whereas the curves for lower excess micromotions can be used to estimate the intrinsic residual micromotion of the ion setup. The second point is of special interest, because this residual energy is the most crucial parameter in almost every experiment involving a Paul trap. It determines the ion's lowest reachable steady-state energy and is hard to measure in experiments. With the help of the simulations atom loss curves may be used to examine the ion's micromotion and hence its steady-state energy.

4.6 Non-equilibrium effects on the thermal cloud

When studying effects of an ion on a thermal cloud, previous approaches mostly relied on equilibrium descriptions of the cloud [170], i.e. the cloud was modeled by a Gaussian distribution with a given temperature at any time. The method described here offers a big advantage compared with the equilibrium model, because it gives rise to non-equilibrium phenomena affecting the velocity and spatial distribution of the cloud. The scattering rate of the ion depends on the thermal cloud density and hence it influences the atom-loss curves. Therefore, when the thermal cloud is used as a calorimeter for the ion, as discussed in the former section, these deviations may become important.

A demonstration that these deviation effects can be strong is given in

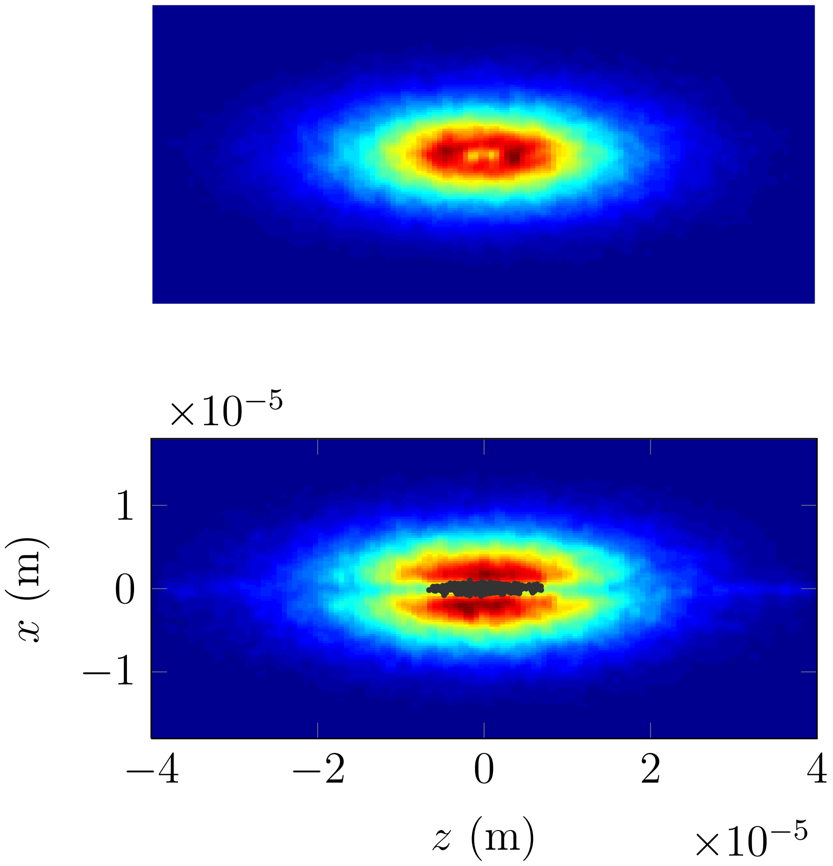

Figure 4.5 – Cross-sections of the thermal cloud density in the $y = 0$ plane at different interaction times 3 ms (upper figure) and 50 ms (lower figure) are shown. Black dots in the lower figure illustrate the position of atom-ion collision events in the cloud. Deviations from a Gaussian distribution are clearly visible after 50 ms.

Fig. 4.5 for different interaction times. In the simulation a $^{138}\mathrm{Ba}^+$ ion was immersed in a neutral atom cloud of 10870 $^{87}\mathrm{Rb}$ atoms at a temperature $T = 120\,\mathrm{nK}$ with trap frequencies $\omega_x = \omega_y = 2\pi \times 110\,\mathrm{rad\,s^{-1}}$ and $\omega_z = 2\pi \times 40\,\mathrm{rad\,s^{-1}}$. The ion's trap frequencies were $\omega_{x,\mathrm{ion}} = \omega_{y,\mathrm{ion}} = 2\pi \times 130 \times 10^3\,\mathrm{rad\,s^{-1}}$ in radial direction and $\omega_{z,\mathrm{ion}} = 2\pi \times 15.5 \times 10^3\,\mathrm{rad\,s^{-1}}$ in the axial direction, the driving frequency was $\Omega_D = 2\pi \times 4.214 \times 10^6\,\mathrm{rad\,s^{-1}}$ and the Mathieu parameters $q_x = -q_y = 0.089$ and $q_z = 0.0$. The excess micromotion energy was $E_{\mathrm{eMM}} = 2.46\,\mathrm{mK} \times k_{\mathrm{B}}$. The initial ion energy was $E = 6\,\mathrm{mK} \times k_{\mathrm{B}}$ equally distributed in all three dimensions.

After an interaction time of 3 ms (upper figure) a small dip in the thermal cloud density appears in the middle of the cloud, where collisions are most

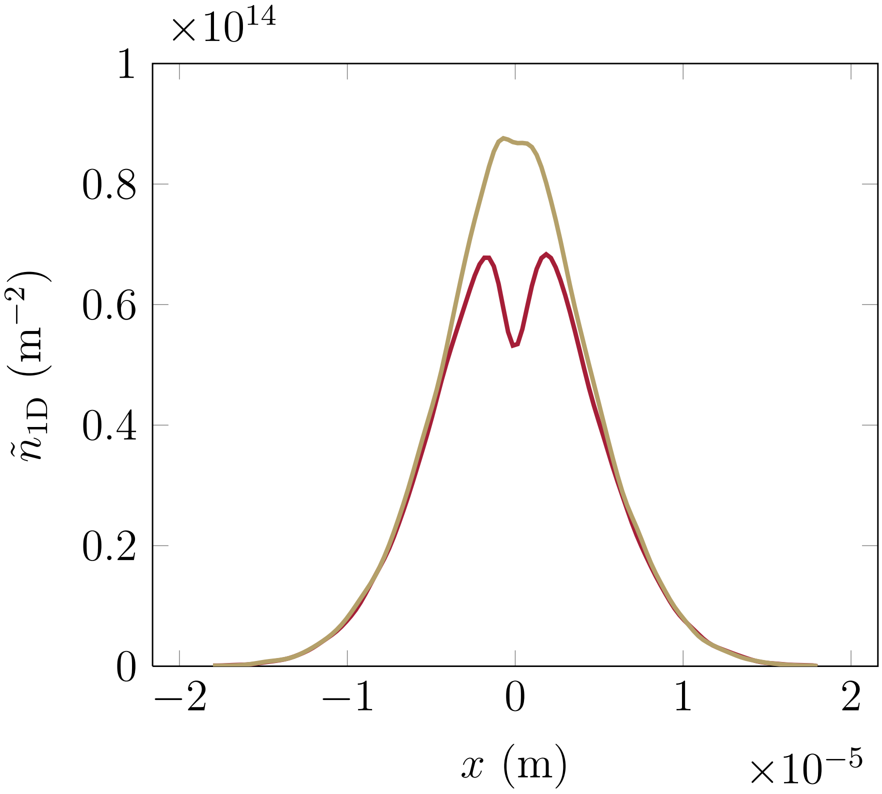

Figure 4.6 – Integrated densities along the z-direction after 3 ms (gold curve) and 50 ms (red curve) interaction time. After 50 ms the thermal density exhibits a dip at $x = 0$ of about 12.5%, which may be visible in experiments.

likely to happen. Because the long z-axis of the Paul trap and the long axis of the ion trap coincide, a small tunnel through the gas along this direction can be seen after an interaction time of 50 ms (lower figure). The position of the scattering events (black points) reveals that atom-ion collisions mostly happen in that region, thereby repelling the scattered thermal atoms and leaving a gap where the collisions took place. This depletion effect in the thermal cloud density obviously affects the scattering rate after Eq. (4.17) and hence the atom-loss curves.

The strong deviation from a Gaussian distribution can also be seen in an integrated version of the thermal cloud density along the z-direction, $\tilde{n}_{\mathrm{1D}}$, as shown in Fig. 4.6. After 3 ms only small changes to the integrated density are visible, whereas after 50 ms the integrated density shows a dip of about 12.5% around $x = 0$, which should be visible in experiments for imaging systems with a spatial resolution higher than 2 µm.

In order to quantify this depletion effect in the density distribution further, the simulated density is compared with a density of an instantaneously thermalized Gaussian distribution. This is of special interest because the simpler model of a Gaussian distribution has been used in previous analyses of the atom-ion system [56, 170]. In this model the temperature T of the gas is updated after each collision, depending on whether the neutral particle leaves the gas or remains trapped. If the particle is still trapped, the transferred energy $E_{\mathrm{t}} = 4(1-\beta)E_{\mathrm{coll}}\sin^2(\theta/2)$ increases the system temperature by

$$\Delta T = \frac{E_{\mathrm{t}}}{3k_{\mathrm{B}}N}. \tag{4.23}$$

However, if the neutral atom leaves the trap the total particle number N is decreased by one and the new temperature is calculated using [170]

$$T = \frac{3Nk_{\mathrm{B}}T - (3/2)k_{\mathrm{B}}T - E_{\mathrm{pot}}(\mathbf{r})}{(N-1)3k_{\mathrm{B}}}, \tag{4.24}$$

where E_{pot} is the harmonic oscillator potential at position $\mathbf{r}$. That means the model simply subtracts the mean kinetic energy and the potential energy of a single atom at the position of the collision from the total energy of the cloud. This new total energy leads to the temperature T in Eq. 4.24 and it is used to calculate an updated version of the Gaussian density, which is given by the expression [177]

$$n_{\mathrm{cl}}(\mathbf{r}) = \frac{N}{(2\pi)^{3/2}\cdot\sigma_x\cdot\sigma_y\cdot\sigma_z}\exp\left(-\frac{x^2}{2\sigma_x^2}-\frac{y^2}{2\sigma_y^2}-\frac{z^2}{2\sigma_z^2}\right), \tag{4.25}$$

where

$$\sigma_i = \sqrt{\frac{k_{\mathrm{B}}T}{m\omega_i^2}}. \tag{4.26}$$

This Gaussian density can be compared with the density in the quantum Boltzmann simulation, $\tilde{n}(\mathbf{r})$, to quantify deviations between the classical model with instantaneous thermalization and the quantum Boltzmann equation. For that purpose the mean values of the densities are calculated in a region around the middle of the trap, where collisions are likely to happen. In order to determine that region, the steady-state energy of the ion was used. For the setup in Fig. 4.6 a steady-state energy $E_{\mathrm{steady}} \sim 5\,\mathrm{mK}\times k_{\mathrm{B}}$ was estimated, which results in oscillation amplitudes $r_{\mathrm{max},x} = r_{\mathrm{max},y} = \sqrt{2E_{\mathrm{steady}}/(m_{\mathrm{ion}}\omega_x^2)} \approx 1\,\mu\mathrm{m}$ and $r_{\mathrm{max},z} = \sqrt{2E_{\mathrm{steady}}/(m_{\mathrm{ion}}\omega_z^2)} \approx 3\,\mu\mathrm{m}$ for the ion. Therefore the mean value of the thermal cloud density in the simulation was taken in a box with length $2\times r_{\mathrm{max},x} \approx 2\,\mu\mathrm{m}$ in the x- and y-direction and $2\times r_{\mathrm{max},z} \approx 6\,\mu\mathrm{m}$ in the z-direction. In order to reduce fluctuations this spatial mean value was additionally averaged over 0.5 ms in time. The same procedure was performed in the classical simulation resulting in spatial and time mean values, $\bar{n}_{\mathrm{cl}}$ for the classical and $\tilde{n}_{\mathrm{mean}}$ for the quantum Boltzmann density. Both averaged densities were compared with each other by calculating the percentage variation e_{gauss}

$$e_{\mathrm{gauss}} = \frac{\bar{n}_{\mathrm{cl}} - \tilde{n}_{\mathrm{mean}}}{\tilde{n}_{\mathrm{mean}}} \times 100. \tag{4.27}$$

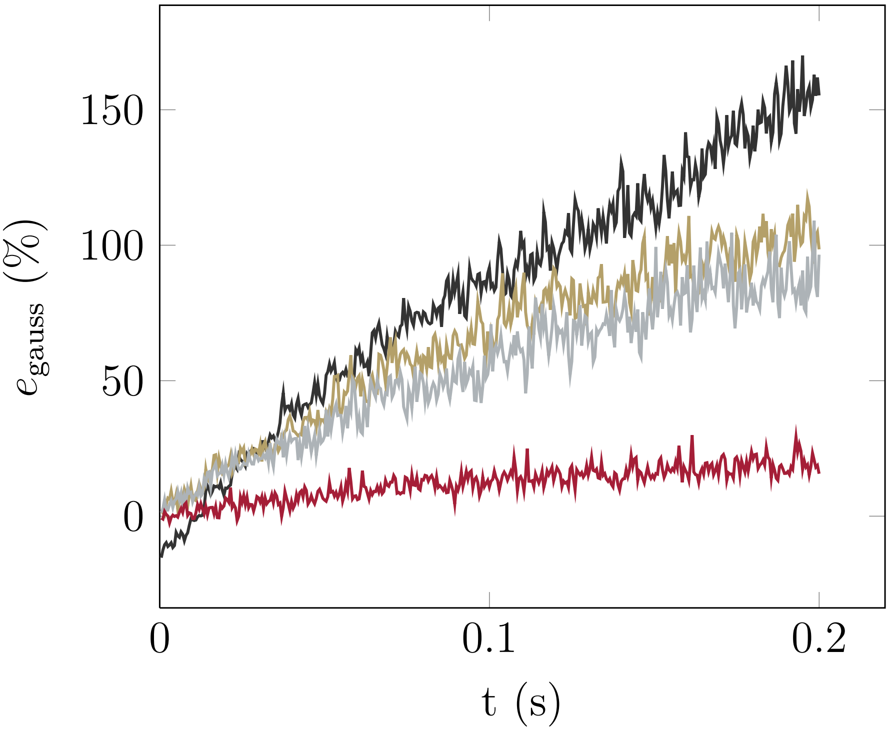

Figure 4.7 – The deviation e_{gauss} between an instantaneously thermalized Gaussian distribution and a thermal cloud described by the quantum Boltzmann equation for four different initial neutral cloud temperatures $T = 90\,\mathrm{nK}$ (black curve), $T = 150\,\mathrm{nK}$ (gold curve), $T = 200\,\mathrm{nK}$ (gray curve) and $T = 800\,\mathrm{nK}$ (red curve).

In Fig. 4.7 e_{gauss} is plotted over the interaction time t of the ion and the cloud for four different temperatures $T = 90\,\mathrm{nK}$ (black curve), $T = 150\,\mathrm{nK}$ (gold curve), $T = 200\,\mathrm{nK}$ (gray curve) and $T = 800\,\mathrm{nK}$ (red curve) for the same setup as in Fig. 4.5. The critical temperature of this system, which was estimated using Eq 1.5, was $T_c = 78.8\,\mathrm{nK}$. In all four cases the deviation between the models grows with increasing interaction time and is higher for lower temperatures. This deviation is the result of two competing effects. One effect is the discussed depletion of thermal atoms, which leads to a reduced density around the trap center. In the setup considered here, this is the dominant error source of the equilibrium model, which overestimates the density in the middle of the trap. However, another effect, which underestimates the density in the equilibrium model is the assumption of instantaneous thermalization. If a neutral atom stays in the trap after the collision, it will most likely have a much higher energy compared with the mean energy, even for small deflection angles. For ion-atom collisions this happens on a much smaller time scale than the thermalization time of the cloud, and therefore results in a few thermal atoms with a very high kinetic energy compared with the mean kinetic energy. As a consequence, the assumption of instantaneous thermalization overestimates the temperature of the whole system because of these few, highly energetic thermal atoms. Therefore, the assumption results in a lower thermal cloud density. However, in the discussed setup this error is small compared with the depletion effect and hence the observed deviations e_{gauss} are positive after 0.2 s for all temperatures. As can be seen in Fig. 4.7 the density deviation between the equilibrium model and the simulations is large for cold clouds close to T_c and increases with interaction time. However, in the case of a relatively warm gas the error is on the order of 10% for this setup and it yields a reasonable estimate for the thermal cloud density. The initial negative error for the state with 90 nK is due to the fact that Bose enhancement already has significant effects on the density distribution of the cloud. The density in the middle of the trap is therefore higher than in the case of a Gaussian distribution.

4.7 Evaporative cooling with ions

Depending on the ion's position in the cloud the induced atom losses lead to cooling or heating of the cloud. An ion far away from the neutral-cloud trap center is more likely to collide with relatively energetic atoms, which may leave the trap because of the transferred collision energy, and cooling can be observed. If the ion is in the center of the trap and scatters mostly with neutral atoms having a smaller energy than the mean kinetic energy, collisions lead to an effective heating.

This behavior can be seen in Fig. 4.8 for the setup described in Sec. 4.5. The ion trap center was shifted relative to the neutral cloud trap center along the z-axis and the resulting energy per particle ϵ is shown over the interaction time t. This was done for four different trap-center separations $d_1 = 20\,\mu\text{m}$

(black curve), $d_2 = 40\,\mu\mathrm{m}$ (red curve), $d_3 = 60\,\mu\mathrm{m}$ (gray curve) and $d_4 = 80\,\mu\mathrm{m}$ (gold curve). The excess micromotion of the ion was $E_{\mathrm{eMM}} = 2.46\,\mathrm{mK} \times k_{\mathrm{B}}$.

In all four cases the energy per particle decreases during the very short ion cool-down phase, which lasts about 0.05 s. Before cooling down, the ion's energy is sufficient to reach regions with more energetic neutral particles. Collisions resulting in an atom leaving the trap are therefore likely to lower the energy per particle irrespective of the atom-ion trap separation. After the cool-down phase, the ion's range of movement is significantly reduced and collisions increase ϵ for $d_1 = 20\,\mu\mathrm{m}$, $d_2 = 40\,\mu\mathrm{m}$ and $d_3 = 60\,\mu\mathrm{m}$. For $d_4 = 80\,\mu\mathrm{m}$ the ion still resides in regions of the cloud, where atoms have a higher energy than the mean energy, even after the ion has cooled down. Hence the evaporative cooling effect continues, albeit slowly.

Although this cooling scheme is less efficient compared with surface evaporation or RF-free-space evaporative cooling, it offers the possibility to truncate only well defined portions of a cloud, given a low ion excess micromotion. This may help in reaching even lower temperatures in ultra-cold gases, when technical heating effects are small.

4.8 Conclusions

The coupling between the quantum Boltzmann equation and a Monte Carlo technique to simulate atom-ion collisions is an adequate model for describing a single trapped ion in a cold thermal cloud. The method is able to describe experimental atom loss curves and gives a detailed description of the ion's motion and energy evolution. Because the atom loss curves depend on the ion's energy, the simulations can be used as a calorimeter for the ion in the experiments, giving insight into the ion's initial energy, the excess micromotion and its steady-state energy. This is of special interest because the excess micromotion is the limiting factor in almost every experiment involving a Paul trap and its minimization is crucial for reaching the ultra-cold regime. In addition the model gives rise to non-equilibrium effects in the distribution function of the thermal cloud. Such an effect is the depletion of thermal atoms from regions where collisions are likely to happen. This leads to a lowered thermal cloud density around the center of the ion trap, which should be measurable in the experiments. The effect is more dominant for cold gases with high densities and becomes negligible for higher temperatures. As with the surface evaporation, the simulations also show a cooling effect due to atom-ion collisions for an ion which resides far away from the trap center. Because the ion's trajectory can be tuned via the excess micromotion this can be used to truncate only small, well defined regions of the cloud in order

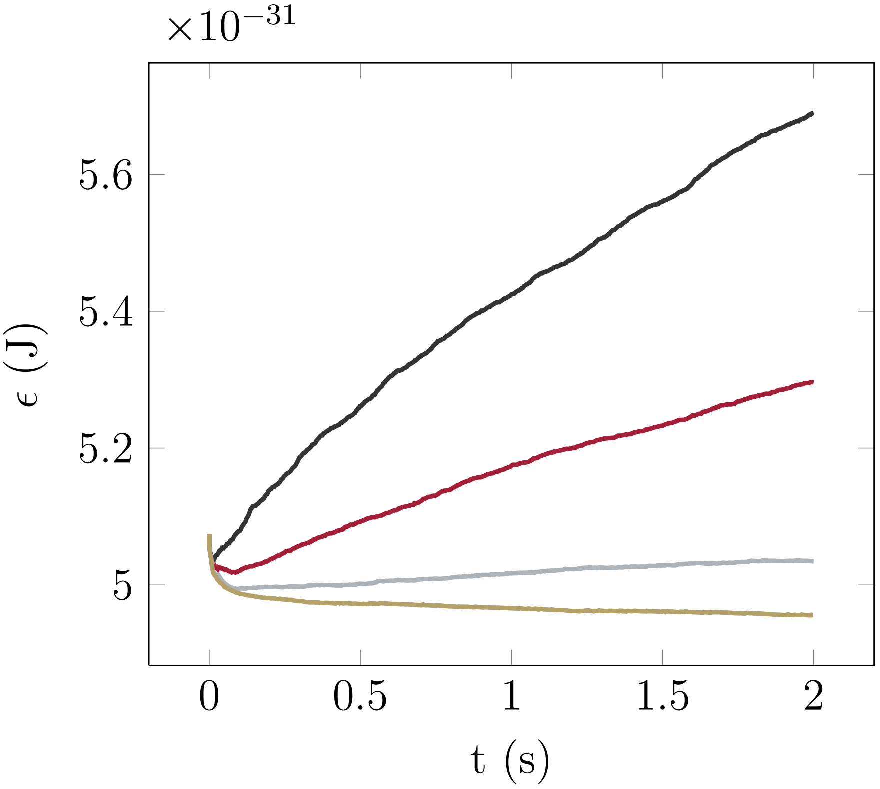

Figure 4.8 – Energy per particle, ϵ, over interaction time t for four different atom-ion trap center separations $d_1 = 20\,\mu\text{m}$ (black curve), $d_2 = 40\,\mu\text{m}$ (red curve), $d_3 = 60\,\mu\text{m}$ (gray curve) and $d_4 = 80\,\mu\text{m}$ (gold curve). After a short cool-down phase the mean energy per particle starts to rise again for d_1, d_2 and d_3. A cooling effect over a longer period can only be observed for a trap center separation of $d_4 \gtrsim 80\,\mu\text{m}$.

to reach even smaller temperatures in ultra-cold gases.

Chapter 5

Cold atoms and vibrating Nanostructures

Mechanical resonators on the micro- or nano-scale offer the possibility to study the transition between classical and quantum physics [178]. In optomechanics the interaction between light and a mechanical resonator is studied and cooling of resonators is an important topic [179–181]. In the context of hybrid systems, nano-mechanical resonators, such as small membranes [182], cantilevers [51] or carbon nanotubes [183] can be coupled to cold atom clouds in order to combine the long coherence times of cold atoms and the accessibility and controllability of the nano structure [42]. This yields new possibilities in the fields of high-precision measurement [45] and quantum-memory devices [184]. However, an oscillating nano object may disrupt clouds of quantum coherent atoms leading to coherence loss, which is unfavorable if the cloud is used to store quantum information [159].

This chapter provides a brief analysis of how an oscillating nanotube lowers the coherence of a BEC depending on its oscillation frequency. It is also discussed how thermal excitations of a nano oscillator may affect a condensed cloud. This is first done for a pure condensate using the GPE and it is shown how to estimate the condensate fraction using the one-particle density matrix in the ergodic hypothesis. The system is then analyzed using the ZNG method and condensate atom numbers as well as density plots are shown over time.

5.1 Oscillating nanotube in a pure condensate

The starting point for the simulations was a fully coherent cloud consisting of 10^4 ^{87}Rb atoms, i.e. $T = 0$ and all atoms were in the ground state. Hence no thermal particles and test particles were present in the system, which could therefore be described by a GPE. The nanotube was modeled by an attractive step function combined with an imaginary potential [185]. The results produced using this simplified potential are not expected to differ much from results obtained with the full Casimir-Polder potential [186]. When at rest the nanotube was located in the cloud-trap center aligned along the y-axis.

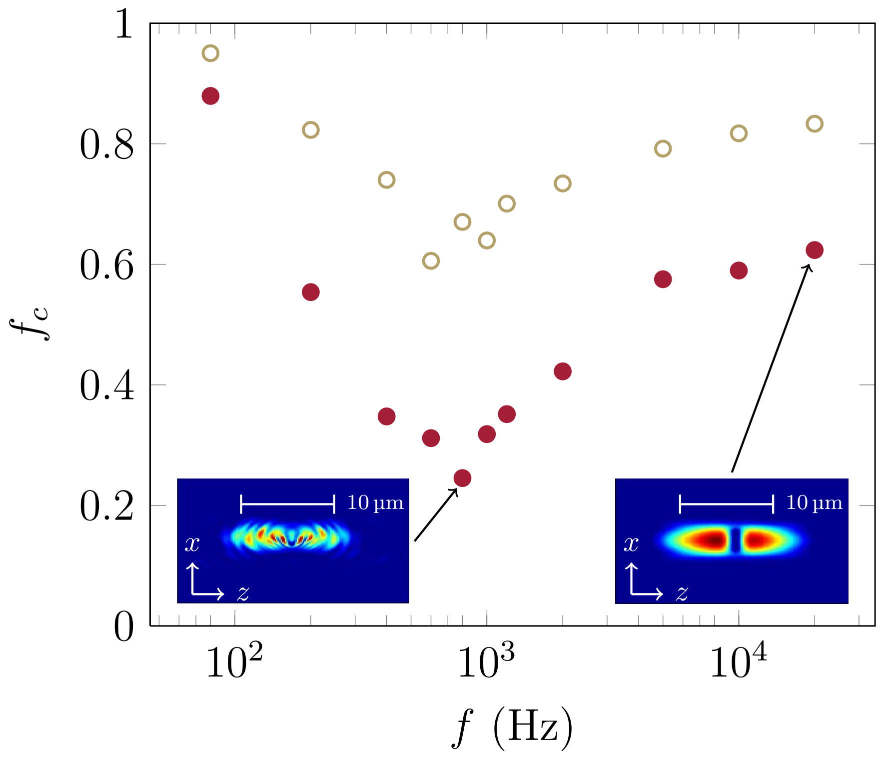

Figure 5.1 – Remaining condensate fraction, $f_c = N_c/N$, against nanotube oscillation frequencies for an interaction time of 0.02 s and for oscillation amplitudes A = 0.75 µm (open gold points) and 1.5 µm (solid red points). Insets show cross-section cloud profiles at the end of the oscillation process.

The cloud was confined in a cigar-shaped trapping potential with trap frequencies $\omega_r = 2\pi \times 80\,\mathrm{rad\,s^{-1}}$ in the radial direction and $\omega_z = 2\pi \times\ 37\,\mathrm{rad\,s^{-1}}$ in the axial direction. To simulate the insertion of the nanotube into the cloud, the tube potential was ramped up within 1 ms. The tube was oscillated with frequency f and amplitude A in the x-direction for 0.02 s, then the tube potential was immediately turned off. Spatial and energy cutoffs absorbed atoms that were excited to very high energies by the process.

In order to estimate the coherence of the cloud, the one-particle density matrix $\rho^{(1)}(z,z') = \langle \Psi^\dagger(z)\Psi(z')\rangle$ along the line $x = 0$ and $y = 0$ in the z-direction was calculated. This was done using the ergodic hypothesis, which allows one to replace the ensemble average in $\rho^{(1)}(z,z')$ by a time average of the line $\Psi(0,0,z)$. The time average was taken over 0.04 s after the oscillation stopped. Diagonalization of $\rho^{(1)}(z,z')$ then gave the highest eigenvalue and hence the relative ground state occupation, after Penrose and Onsager [187].

The relative ground state occupation, i.e. ground state atoms over remaining atom number $f_c = N_c/N$, is plotted in Fig. 5.1 against oscillation frequencies for two oscillation amplitudes $A = 1.5\,\mu\text{m}$ (solid red points) and $A = 0.75\,\mu\text{m}$ (open gold points). Although the insertion and removal of the tube already leads to excitations of ground state atoms, f_c is largely maintained for low frequencies. When raising the frequency, f_c decreases until it reaches a minimum at around $f = 800\,\text{Hz}$. If the frequency is further increased the condensate fraction becomes larger again, saturating at a constant value. As expected, higher amplitudes create more disruption.

The occurence of a resonant frequency can be explained by looking at the local speed of sound $v_\text{s}(\mathbf{r})$

$$v_\text{s}(\mathbf{r}) = \sqrt{n_c(\mathbf{r})\frac{4\pi\hbar^2 a}{m^2}} \tag{5.1}$$

and the correlation time, $t_c = l_\text{H}/v_\text{s}$, of the BEC, where l_H is the condensate healing length [77]. The local speed of sound sets a lower limit for the formation of topological excitations. Therefore a drop in f_c occurs when the tube velocity exceeds $v_\text{s}(\mathbf{r})$. The maximal velocity for an oscillating tube is given by $v_\text{max} = A2\pi f$. By using the peak density in the middle of the trap, this leads to a threshold frequency of $f \sim 60\,\text{Hz}$ for an amplitude $A = 1.5\,\mu\text{m}$; the population of excited modes increases with frequency.

However, if the oscillation period is much smaller than the correlation time, i.e. $1/f \ll t_c$, the condensate is not able to respond to the fast varying tube potential and sees an effective static, time-averaged potential causing only minimal disruption in the cloud (Fig. 5.1 inset bottom right). Hence, f_c is also retained for very high oscillation frequencies and another threshold frequency of $1/t_c \approx 3000\,\text{Hz}$ is obtained, by assuming the peak density for the correlation time. Therefore the cloud should only be strongly disrupted for $60\,\text{Hz} \lesssim f \lesssim 3000\,\text{Hz}$, which is confirmed by the simulation results.

Concerns that thermal vibrations of a nanotube might reduce the coherence of a cold cloud are hence baseless: thermally excited mechanical vibrations in nanotubes typically have frequencies $f > 100\,\text{kHz}$ and amplitudes $A \ll 1\,\mu\text{m}$ [188], and are therefore very unlikely to disrupt the cloud. Hence coherence loss due to oscillations of the nanotube should only be observed if it is externally driven at frequencies, which are much lower than thermally excited oscillation frequencies.

5.2 Oscillating nanotube in a cold cloud at finite temperatures

In addition to a fully coherent cloud, the behavior of a gas surrounding an oscillating nanotube at a very low but finite temperature was studied using the ZNG formalism. This description differs significantly from the one described in the previous section and hence a direct comparison between the two models is not practicable. Compared with the former analysis ZNG includes the simulation of highly energetic excitations, which affect the condensate fraction of the cloud. In addition, the condensate atom number is determined by an integral over the wavefunction, $N_c = \int d\mathbf{r}\psi(\mathbf{r},t)$, instead of the biggest eigenvalue of the one-particle density matrix. Furthermore, the initial condensate fraction is necessarily below one in the ZNG simulation, because the starting state is at a temperature $T > 0$. Nevertheless, the ZNG model confirms the resonant behavior, which was observed in the fully coherent simulations.

In order to model particle loss, test particles were deleted when hitting the nanotube, as in the case of the surface problem. The scattering between condensate atoms and the tube was simulated by the same attractive step potential as in the section before. A total number of 9850 ^{87}Rb atoms was simulated. The initial temperature was $T = 5\,\mathrm{nK}$ resulting in approximately 9100 condensate and 750 thermal atoms in the Hartree-Fock ground state. The geometry, position and oscillation direction of the tube were identical to those in the previous section. The oscillation time was chosen to be $t_{\mathrm{osc}} = 10\,\mathrm{ms}$, the oscillation amplitude $A = 2\,\mu\mathrm{m}$ and the total simulation time was 1 s.

In Fig. 5.2 the resulting condensate atom numbers (upper plot) and thermal atom numbers (lower plot) are shown over time for two different tube oscillation frequencies $f = 80\,\mathrm{Hz}$ (red curve) and $f = 200\,\mathrm{Hz}$ (black curve). During the oscillation time, t_{osc}, the condensate atom number experiences a rapid drop, which stops abruptly when the nanotube is removed. This drop is much more pronounced for the condensate than for the thermal cloud, because the overlap between the tube and the condensate is much higher than the overlap between the thermal cloud and the tube. After the short oscillation time the cloud is not in thermal equilibrium any more and

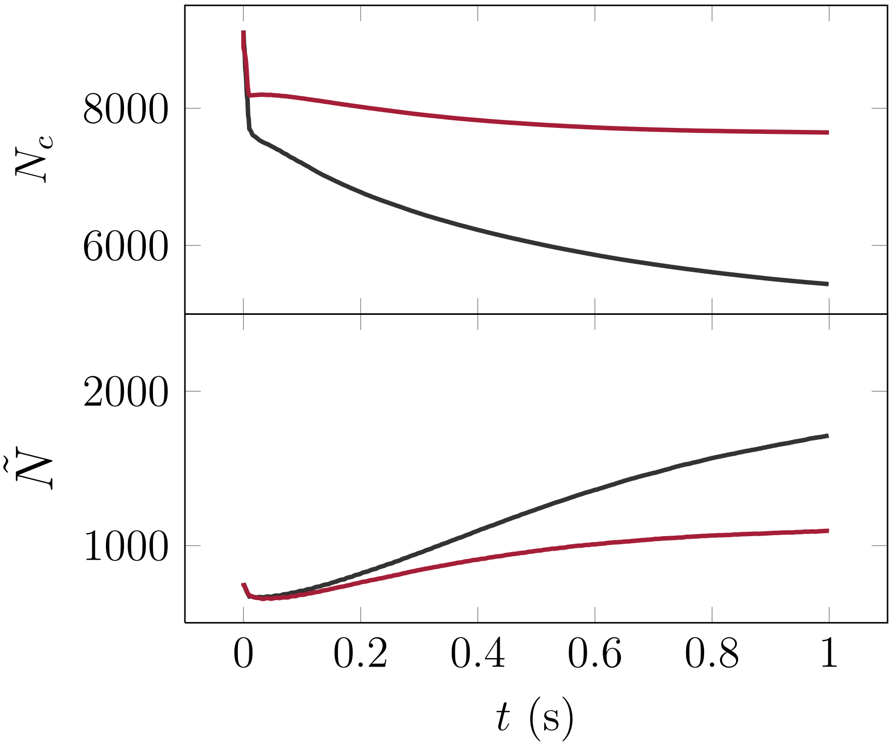

Figure 5.2 – Condensate (upper plot) and thermal atom number (lower plot) over time for a cold cloud, which was exposed to an oscillating nanotube with two different frequencies $f = 80\,\mathrm{Hz}$ (red curves) and $f = 200\,\mathrm{Hz}$ (black curves). The initial temperature of the cloud was $5\,\mathrm{nK}$, the oscillation amplitude $A = 2\,\mu\mathrm{m}$ and the oscillation time $t_{\mathrm{osc}} = 10\,\mathrm{ms}$. Trap frequencies were the same as in Sec. 5.1.

condensate particles scatter into the thermal cloud. Hence, a heating effect due to the oscillating nanotube is evident. After 1 s the cloud consists of approximately 7650 condensate and 1100 thermal atoms in the $f = 80\,\mathrm{Hz}$ case, leading to a final condensate fraction of $f_c \approx 88\%$. The final condensate fraction in the case of $f = 200\,\mathrm{Hz}$ is $f_c \approx 76\%$.

In Fig. 5.3 the final condensate fraction for different oscillation frequencies f is shown. For a gas at 5 nK the ZNG method reveals the same resonance frequency for coherence loss around $f \sim 800\,\mathrm{Hz}$ as the density matrix calculations in the previous section. However, a direct comparison between condensate fractions is difficult due to the difference in the initial condensate atom numbers and the neglection of highly energetic excitations in the case of the one-particle density matrix approach. In addition the oscillation time for the ZNG simulations was half as long as the one used in Fig. 5.1 in order to keep more atoms in the trap and hence lower the following thermalization times (simulation times would have otherwise been unacceptably long). This led to significantly higher condensate fractions.

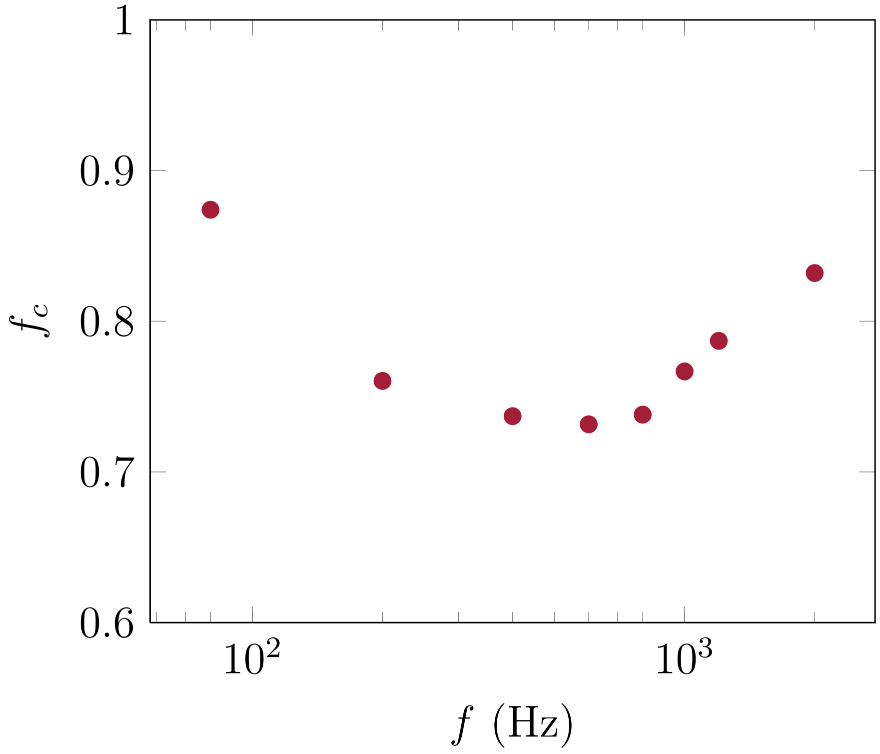

Figure 5.3 – Remaining condensate fraction, $f_c = N_c/N$, in the ZNG simulations against nanotube oscillation frequencies for an interaction time $t_{\mathrm{osc}} = 10\,\mathrm{ms}$ and oscillation amplitude $A = 2.0\,\mu\mathrm{m}$. The initial state temperature was $T = 5\,\mathrm{nK}$ resulting in 9100 condensate and 750 thermal atoms.

Figure 5.4 shows density cross sections of the condensate and the thermal cloud through the $y = 0$ plane at different simulation times, t, for the $f = 200\,\mathrm{Hz}$ simulation. The top row shows the densities after a full oscillation period at $t = 5\,\mathrm{ms}$. Topological excitations such as sound waves in the condensate are visible. In contrast, the thermal cloud is still nearly unperturbed. After $t = 75\,\mathrm{ms}$ the condensate as well as the thermal cloud are clearly disrupted. Unlike in the equilibrium case, where both regions are largely separated, the thermal cloud and the condensate are mingled inside the trap. After $t = 975\,\mathrm{ms}$ the cloud has enough time to re-thermalize and the two regions are again separated, with the condensate sitting in the middle of the trap and the thermal cloud surrounding it.

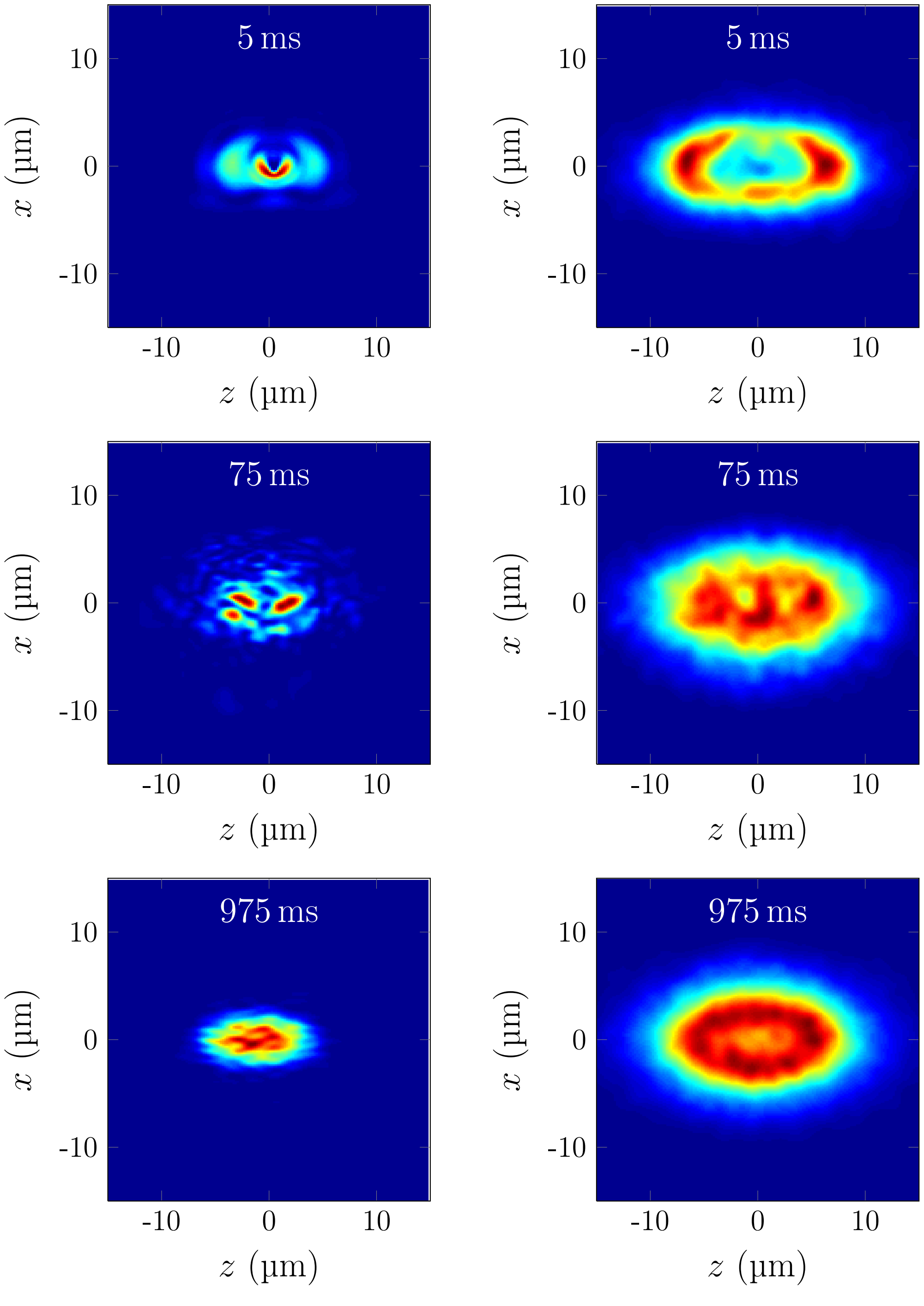

Figure 5.4 – Condensate (left column) and thermal-cloud-density cross sections (right column) in the $y = 0$ plane at different times, t, for a cloud exposed to an oscillating nanotube with oscillation frequency $f = 200\,\mathrm{Hz}$. The interaction time was $t_{\mathrm{osc}} = 10\,\mathrm{ms}$. The first row is after one oscillation period of the tube at $t = 5\,\mathrm{ms}$, the second row is at $t = 75\,\mathrm{ms}$ and the third row shows the densities after $t = 975\,\mathrm{ms}$. The color bar has been rescaled for each image.

Chapter 6

Conclusions

In this thesis a numerical implementation of the ZNG model was outlined. In contrast to previous implementations, the presented algorithms were based on square collision bins to solve the collision integrals, which should allow for simulations of arbitrary geometries. In addition an adaptive scheme was used to minimize the effects of finite test-particle numbers and increase the collision-grid resolution. The code was written in parallel, which reduced calculation times by approximately an order of magnitude for test-particle numbers used in the simulations. The new code was carefully tested by recreating known results for finite-temperature systems. The model was then used to study finite-temperature effects in three different hybrid systems.

The numerical simulations of a cold ^{87}Rb cloud in front of a solid surface showed that the ZNG model in the presented form meets the demanding criteria necessary to describe the arising atom losses. Although these losses are governed by many factors, the simulations revealed that these factors can be summarized by three different time scales, determining the atom losses. Whereas analytical models can only be used in extremely limited situations, the ZNG model, including collisions, is able to describe non-equilibrium thermalization effects, which are important for the surface-evaporation problem. In addition, ZNG allows for a description of condensate growth and reasonable condensate atom numbers are achieved even for initial states well above T_c. This is of special interest because the model was initially not designed for phase transitions, as it neglects fluctuations. However simulating ground-state-number fluctuations by setting a condensate seed creates the expected broad s-shaped growth curves.

The simulations seem to suggest that the main fundamental limitation of the model is the assumption of s-wave scattering, which breaks down at about 100 µK. A first attempt to consider scattering events that go beyond s-wave scattering was made for a hot ion in a cold thermal cloud. The scattering cross section was calculated semi-classically using many partial waves and the time evolution of the thermal cloud was determined by a quantum Boltzmann equation. The observed atom losses are in agreement with experimental data. It was outlined how the corresponding loss curves may be used to estimate the steady-state energy and micromotion of the ion, which is difficult to measure experimentally. In comparison with other methods, the quantum Boltzmann equation allows for non-equilibrium effects in this system. An example of such an effect is a density depletion due to atom-ion collisions. Differences between the quantum Boltzmann and a Gaussian equilibrium model were quantified by comparing the simulated density with the equilibrium distribution.

As a final consideration, the coherence loss of a pure BEC was explored when coupled to an oscillating nanotube. A resonance frequency was observed at which the condensate fraction drops to a minimum, whereas very large or small frequencies had little effect on the coherence of the cloud. This was explained by looking at the speed of sound and the healing length of the condensate, which together form a coherence time, allowing one to estimate the resonance frequency. Because thermal excitations of a nanotube usually have much larger frequencies and much smaller amplitudes, coherence loss is expected to be negligible.

In summary, the simulations showed that the derived tools are able to describe common, yet numerically challenging hybrid systems. Where possible this was confirmed by comparing the numerical results with experimental data. The ZNG model yields a full dynamical description of the thermal cloud and gives rise to non-equilibrium effects, which is a big advantage not only in the context of hybrid systems. It should be noted that, whenever thermalization plays an important role in these systems a full implementation of the ZNG algorithm, which includes collision integrals, is needed. Descriptions of collisions beyond s-wave scattering can also be numerically calculated, reproducing experimental loss rates and hence collision rates, as shown by the discussion of the atom-ion hybrid system.

6.1 Future work

In order to simulate more realistic hybrid setups an intuitive next step would be to improve the models used for solid-state devices. This includes the implementation of a back action on the device, yielding the possibility to describe energy exchange between the two systems and hence cooling or heating of the solid-state device. Another way towards the simulation of a relevant system can be done by modeling the detailed Casimir-Polder potential of a solid-state device used for precision measurement. Although the exact shape of the potential has little effect on atom losses in a BEC, the smaller de Broglie wavelength of thermal atoms leads to a higher sensitivity towards the external potential [186]. So far there is still a discrepancy between the theoretically predicted and measured Casimir-Polder potential for a carbon nanotube immersed in a thermal cloud [186]. Simulating these losses using the quantum Boltzmann equation and the theoretically predicted Casimir-Polder potential may help to explain these deviations. In precision measurement approaches, which consist of a hybrid system with a condensed gas, the effect of thermal excitations might not be negligible. In these cases the derived tools are excellent candidates for estimating the effect of the thermal cloud on the quantities of interest.

In addition, the numerical methods outlined in this thesis offer also great potential in areas other than hybrid systems. Because every experiment in the lab is performed at non-zero temperature, the ZNG method may yield a possibility to describe a broad range of problems in a very realistic manner, especially as the role of thermal fluctuations is not always predictable beforehand. For example, this includes cold atoms in optical lattices or two-component gas mixtures. The method may also be improved to give a full dynamical simulation of thermal excitations in dipolar condensed Bose gases, which are the subject of experimental and theoretical studies because of the long-ranged dipole-dipole interaction potential [189–191]. For example, these dipolar gases are used to simulate magnetic effects in superconductors [192].

In the context of fluid dynamics a form of the classical Boltzmann equation has already been used [193] to study “the most important unsolved problem of classical physics”, a quote by Feynman about the still unsolved problem of turbulence [194]. In the fully quantum degenerate regime the GPE was used to study quantum turbulence. However, the ZNG method, combining both equations, should allow for a description in an intermediate regime for a not-fully condensed gas. Also, a regime close to T_c, where the ground state occupation is still negligible but Bose statistic becomes important, may be studied by using the quantum Boltzmann equation instead of its classical counterpart.

Another interesting future project would be the inclusion of fluctuations, which are neglected by ZNG, and are important for a gas close to T_c. A possible way to include these fluctuations could be to couple the quantum Boltzmann equation to the stochastic GPE instead of a generalized GPE. Although the choice of an energy cutoff defining the coherent region is a non-trivial problem, the resulting method might be able to capture all the physics necessary to model the BEC phase transition and answer open questions concerning the growth rate of a BEC [136].

In summary many effects on the promising “small” scale, mentioned by

Feynman in his speech, are still not understood completely and need to be explored, in order to get a better picture of the fundamental physics taking place at the quantum scale. There is still a lot to learn about Casimir forces, decoherence, quantum fluctuations and quantum reflection effects, and their importance for newly engineered nano- or quantum-computation devices. But in order to explore these effects in detail, hybrid-system experiments need a well-founded theoretical background. Depending on the system thermal fluctuations and temperature can play an important role and should therefore be considered by the underlying theory. In this thesis it has been shown how finite temperatures can be included in a numerical description of hybrid systems and the applied models may be used as a basis for further work in the field, to get a better theoretical understanding of "the bottom".

Appendix A

Monte Carlo calculations

In this Appendix, numerical methods, which are based on random number sampling or Monte Carlo methods that are mentioned in the main text, are discussed in detail.

A.1 Rejection method

To calculate random numbers from a distribution function $f(x)$, for which other common sampling methods fail (for example if the corresponding cumulative distribution function does not exist or can not be calculated easily, which makes inverse transform sampling difficult), the von Neumann rejection method offers an elegant solution [195]. In order to sample $f(x)$, another distribution function $g(x)$ with

$$f(x) \leq g(x) \tag{A.1}$$

for all x, is used. The distribution function $g(x)$ is also referred to as the comparison function. If one chooses a point (x,y) which is uniformly distributed in the area under the comparison function $g(x)$, the point is rejected if it lies above the original distribution function $f(x)$ and another point is chosen. The point is accepted if it lies in the area below $f(x)$. Because the selected points were uniformly distributed in the area under $g(x)$ they are also uniformly distributed in the area under $f(x)$ and therefore their x values follow the desired distribution.

The ratio between rejected and accepted points is given by the ratio between the areas under $f(x)$ and $g(x)$. The actual method works as follows:

- Choose a random number X which follows the distribution function $g(x)$ (for example with inverse transform sampling).

- Choose another random number Y with $Y \in [0,g(X)]$. The point (X,Y) is then uniformly distributed under the area of $g(x)$.
- If $Y < f(X)$ accept X, otherwise select another random pair (X,Y).

This scheme gives random variables X which follow the distribution $f(x)$.

A.2 Collision rates

The connection between the collision rates (Γ_{22} and Γ_{12}) and the collision probabilities (P_{ij}^{22}, P_i^{out} and P_i^{in}) can be seen by integrating them numerically using Monte Carlo methods [75].

As outlined in section 2.3 the mean collision rate between two thermal atoms per unit time and unit volume is given by

$$\begin{aligned}\Gamma_{22}^{\mathrm{out}}(\mathbf{r},t) =& \int \frac{d\mathbf{p}_1}{(2\pi\hbar)^3} C_{22}^{\mathrm{out}}(\mathbf{r},t)\\ =& \frac{\sigma}{\pi h^6 m^2} \int d\mathbf{p}_1 f_1 \int d\mathbf{p}_2 f_2 \int d\mathbf{p}_3 \int d\mathbf{p}_4 \\ &\times \delta(\mathbf{p}_1 + \mathbf{p}_2 - \mathbf{p}_3 - \mathbf{p}_4)\delta(\tilde{\epsilon}_1 + \tilde{\epsilon}_2 - \tilde{\epsilon}_3 - \tilde{\epsilon}_4)\\ &\times (1 + f_3)(1 + f_4).\end{aligned} \tag{A.2}$$

As in the case of a classical two-body problem it is convenient to split the dynamics into a relative and center-of-mass motion by introducing new momenta

$$\mathbf{p}' = \frac{\mathbf{p}_1 - \mathbf{p}_2}{\sqrt{2}} \tag{A.3}$$

$$\mathbf{p}_0 = \frac{\mathbf{p}_1 + \mathbf{p}_2}{\sqrt{2}}. \tag{A.4}$$

Together with the constraint of momentum and energy conservation this leads to a collision rate of the form

$$\Gamma_{22}^{\mathrm{out}} = \int \frac{d\mathbf{p}_1}{(2\pi\hbar)^3} f_1 \int \frac{d\mathbf{p}_2}{(2\pi\hbar)^3} f_2 \int \frac{d\Omega}{4\pi} \sigma |\mathbf{v}_1 - \mathbf{v}_2| (1 + f_3) \cdot (1 + f_4), \tag{A.5}$$

with $\mathbf{p}_{3,4} = (\mathbf{p}_0 \pm p'\hat{\mathbf{u}}(\Omega))/\sqrt{2}$, where p' denotes the magnitude of $\mathbf{p}'$, and $\hat{\mathbf{u}}$ a unit vector in a direction determined by the scattering angle Ω. To write the above expression in a more compact form, the integrand in the above expression is split into two functions $w(p)$ and $g(p)$

$$w(p) = \frac{f(\mathbf{p}_1) f(\mathbf{p}_2)}{(2\pi\hbar)^6} \tag{A.6}$$

$$g(p) = \int \frac{d\Omega}{4\pi} \sigma |\mathbf{v}_1 - \mathbf{v}_2| (1 + f_3) \cdot (1 + f_4), \tag{A.7}$$

where p is a point in the six dimensional momentum space

$$p = \begin{pmatrix} p_{x1} \\ p_{y1} \\ p_{z1} \\ p_{x2} \\ p_{y2} \\ p_{z2} \end{pmatrix}. \tag{A.8}$$

Substituting these expressions in Eq. (A.5) leads to

$$\Gamma_{22}^{\text{out}} = \int d^6p \, w(p) g(p). \tag{A.9}$$

The six dimensional integral is now solved using a rejection method. For that purpose a momentum interval $[-p_{\max}/2, p_{\max}/2]$ for each component of p is defined on which the integrand is non-zero. Then a six-dimensional random point p_i, where each component $p_{i=1,\ldots,6}$ of p_i fulfills $p_{i=1,\ldots,6} \in [-p_{\max}/2, p_{\max}/2]$, and a uniformly distributed random number $R_i \in [0, w_{\max}]$ are chosen. Here $w_{\max}$ denotes the maximum of the function $w(p)$. If $R_i < w(p_i)$ the point is accepted. For every accepted point the quantity $g(p_i)$ is accumulated and divided by the total number of random points N chosen, leading to an approximation of the integral

$$\Gamma_{22}^{\text{out}} \simeq (p_{\max})^6 w_{\max} \frac{1}{N} \sum_i{}' g(p_i). \tag{A.10}$$

The prime on the summation denotes the fact that only accepted points are considered for the sum. For $g = 1$ the approximated integral would be $\tilde{n}(\mathbf{r})^2$ and therefore

$$\tilde{n}(\mathbf{r})^2 = (p_{\max})^6 w_{\max} \frac{N_s}{N}. \tag{A.11}$$

With this expression Eq. (A.10) becomes

$$\Gamma_{22}^{\text{out}} \simeq \tilde{n}(\mathbf{r})^2 \frac{1}{N_s} \sum_i{}' g(p_i). \tag{A.12}$$

All N_s accepted points correspond to N_s momentum pairs, $\mathbf{p}_1$ and $\mathbf{p}_2$, in a volume $\Delta^3 r$ around the position $\mathbf{r}$, which follow the distribution $f(\mathbf{p})$. The accepted points can therefore be identified with N_s pairs of phase-space points or test particles. As these test particles model the thermal density in a collision cell it follows

$$\tilde{n}(\mathbf{r}) = \gamma \frac{2N_s}{\Delta^3 r}. \tag{A.13}$$

By inserting this and the exact expression for g into Eq. (A.12) one obtains

$$\Delta^3 r \Gamma_{22}^{\text{out}} \simeq 2\gamma \sum_{(i,j)} \tilde{n}(\mathbf{r})\sigma|\mathbf{v}_i - \mathbf{v}_j| \int \frac{d\Omega}{4\pi}(1+f_3)(1+f_4), \tag{A.14}$$

where the sum over accepted points was rewritten to emphasize the fact that it is equivalent to a sum over test particle pairs (i,j). This equation allows the definition of a collision probability P_{ij}^{22} for a test particle pair (i,j) in a time interval Δt to be written as

$$P_{ij}^{22} = \tilde{n}(\mathbf{r})\sigma|\mathbf{v}_i - \mathbf{v}_j| \int \frac{d\Omega}{4\pi}(1+f_3)(1+f_4)\Delta t, \tag{A.15}$$

which is equal to Eq. (2.48).

For the C_{12} collisions it is convenient to split the collision rate into an "in"- and "out"-rate which refers to particles scattering into or out of the condensate. This leads to "in"- and "out"-collision probabilities for each individual test particle. By rewriting the "out"-collision rate with respect to the center-of-mass and relative motion as in the case of Γ_{22}^{out} (with the relative velocity now being $v_r^{\text{out}} = \sqrt{|\mathbf{v}_c - \mathbf{v}_2| - 4gn_c/m}$), one finds

$$\Gamma_{12}^{\text{out}} = \int \frac{d\mathbf{p}_2}{(2\pi\hbar)^3} f_2 n_c v_r^{\text{out}} \int \frac{d\Omega}{4\pi}\sigma(1+f_3)\cdot(1+f_4). \tag{A.16}$$

As before, the integrand can be split up into two functions $g(p)$ and $w(p)$

$$g(p) = n_c v_r^{\text{out}} \sigma \int \frac{d\Omega}{4\pi}(1+f_3)\cdot(1+f_4) \tag{A.17}$$

$$w(p) = \frac{f(p)}{(2\pi\hbar)^3} \tag{A.18}$$

and the Monte Carlo integration leads to a sum over N_s test particles

$$\Delta^3 r \Gamma_{12}^{\text{out}} \simeq \gamma \sum_{i=1}^{N_s} g(p_i), \tag{A.19}$$

which gives the "out"-collision probability P_i^{out} for each test particle

$$P_i^{\text{out}} = g(p_i)\Delta t = n_c \sigma v_r^{\text{out}} \int \frac{d\Omega}{4\pi}(1+f_3)\cdot(1+f_4)\Delta t. \tag{A.20}$$

For the "in"-collision rate, defined by Eq. (2.3.2), energy conservation can be rewritten, taking into account that the thermal atom scattering into the condensate has a lower potential energy. This leads to

$$\frac{\mathbf{p}_2^2}{2m} + \frac{\mathbf{p}_4^2}{2m} = \frac{\mathbf{p}_c^2}{2m} + \frac{\mathbf{p}_3^2}{2m} + gn_c \tag{A.21}$$

for two incoming thermal atoms 2 and 4, one outgoing thermal atom 3 and an outgoing condensate atom. Together with momentum conservation

$$\mathbf{p}_2 + \mathbf{p}_4 = \mathbf{p}_3 + \mathbf{p}_c \tag{A.22}$$

this leads to a constraint for $\mathbf{p}_4$ and $\mathbf{p}_2$

$$(\mathbf{p}_c - \mathbf{p}_2) \cdot (\mathbf{p}_c - \mathbf{p}_4) - mgn_c = 0. \tag{A.23}$$

Therefore the integration over $\mathbf{p}_3$ leads to an "in"-collision rate of the form

$$\begin{aligned}\Gamma_{12}^{\mathrm{in}} = \int \frac{d\mathbf{p}_2}{(2\pi\hbar)^3} f_2 \int \frac{d\mathbf{p}_4}{(2\pi\hbar)^3} f_4 \frac{n_c \sigma (2\pi\hbar)^3}{\pi m} \\ \cdot\, \delta((\mathbf{p}_c - \mathbf{p}_2) \cdot (\mathbf{p}_c - \mathbf{p}_4) - mgn_c).\end{aligned} \tag{A.24}$$

Because of the constraint given by Eq. (A.23) $\mathbf{p}_4$ may be written as

$$\mathbf{p}_4 = \mathbf{p}_c + \mathbf{p}_\perp + \frac{gn_c}{mv_r^{\mathrm{in}}} \mathbf{p}_r^{\mathrm{in}}, \tag{A.25}$$

where $p_r^{\mathrm{in}} = m\,|\mathbf{v}_2 - \mathbf{v}_c|$ and $\mathbf{p}_\perp$ is a momentum vector perpendicular to $\mathbf{p}_r^{\mathrm{in}}$. With that, the integral over $\mathbf{p}_4$ in Eq. (A.24) can be substituted by an integral over velocities $\mathbf{v}_\perp$, which are perpendicular to $\mathbf{v}_r^{\mathrm{in}} = |\mathbf{v}_2 - \mathbf{v}_c|$

$$\Gamma_{12}^{\mathrm{in}} = \int \frac{d\mathbf{p}_2}{(2\pi\hbar)^3} f_2 \frac{n_c \sigma}{\pi v_r^{\mathrm{in}}} \int d\mathbf{v}_\perp f_4 (1 + f_3). \tag{A.26}$$

Following the same procedure as for the "out"-collisions this leads to an "in"-collision probability for each test particle, P_i^{in}, of the form

$$P_i^{\mathrm{in}} = \frac{\sigma n_c}{\pi v_r^{\mathrm{in}}} \int d\mathbf{v}_\perp f_4 (1 + f_3) \Delta t. \tag{A.27}$$

Appendix B

Algorithms

This Appendix shows pseudo-code examples of some of the discussed algorithms to facilitate the implementation of a full ZNG code. The algorithms give insight into implementation details, which are typically not presented in the literature.

Hartree-Fock equilibrium state code

```
input  : $N_c$,$N$,$T$,$a$,$\omega_{i=x,y,z}$
output : Equilibrium values $\Phi_0(\mathbf{r})$, $\mu_0$ and $\tilde{n}$

// Initialize data;

$\Phi_0(\mathbf{r}) \leftarrow$ Gaussian function normalized to $N_c$;
$\tilde{n}(\mathbf{r}) \leftarrow 0$;
$\mu_0 \leftarrow 0$ ;

/* Iterate imaginary time solver ImTimeSolve($\Phi_0$) with
adjusting values $N_c$, $\tilde{n}$ and $n_{c0}$ until chemical potential
converges                                                        */

while $\mu_0$ is not converged do
    $\Phi_0(\mathbf{r}), \mu_0 \leftarrow$ ImTimeSolve($\Phi_0$) ;
    $n_c(\mathbf{r}) \leftarrow |\Phi_0(\mathbf{r})|^2$ ;

    // calculate thermal properties and new $N_c$

    $\tilde{n}(\mathbf{r}) \leftarrow \frac{1}{\Lambda^3} g_{3/2}(z_0(\mathbf{r}))$ ;
    $\tilde{N} \leftarrow \int d\mathbf{r}\tilde{n}_0(\mathbf{r})$;
    $N_c \leftarrow N - \tilde{N}$ ;

    // renormalize wavefunction

    $\Phi_0(\mathbf{r}) \leftarrow \sqrt{N_c} \cdot \Phi_0(\mathbf{r}) / \sqrt{\int d\mathbf{r}\Phi_0(\mathbf{r})}$;
end
```

Algorithm 1: Self consistent equilibrium solver for the coupled equations Eq. (2.1) and Eq. (2.2). The function ImTimeSolve(Φ_0) iterates the wave function Φ_0 in imaginary time for one small time step Δt.

Condensate time evolution

```
input  : $\Phi(x,t)$
output : $\Phi(x,t+\Delta t)$
$\tilde{V}(t) \leftarrow \frac{1}{2}\left[3\hat{V}(t) - \hat{V}(t-\Delta t)\right]$ ;        // calculate mixed potential
$\Phi(x,t) \leftarrow e^{-i\tilde{V}(t)\Delta t/2\hbar} \cdot \Phi(x,t)$ ;                      // multiply V-term
$\Phi(k,t) \leftarrow$ FFTW($\Phi(x,t)$) ;             // transform in momentum space
$\Phi(k,t) \leftarrow e^{i\hbar k^2 \Delta t/2m} \cdot \Phi(k,t)$ ;                      // multiply T-term
$\Phi(x,t) \leftarrow$ FFTW$^{-1}$($\Phi(k,t)$) ;         // transform in position space
$\Phi(x,t+\Delta t) \leftarrow e^{-i\tilde{V}(t)\Delta t/2\hbar} \cdot \Phi(x,t)$ ;                // multiply V-term
```

Algorithm 2: Single time step of the pseudo-spectral method. FFTW denotes a fast Fourier transformation and FFTW^{-1} is the corresponding inverse transform.

Test particle time evolution

```
input  : $N$ test particles at time $t$ with positions $\mathbf{r}$ and velocities $\mathbf{v}$,
         Hartree-Fock potential $U(\mathbf{r})$
output : $N$ test particles at time $t + \Delta t$
for $i<N$ do
    $\tilde{\mathbf{r}}_i \leftarrow \mathbf{r}_i(t) + \frac{1}{2}\mathbf{v}_i(t)\Delta t$ ;                          // apply $\mathcal{L}_V$
    $\mathbf{v}_i(t+\Delta t) \leftarrow \mathbf{v}_i(t) - \frac{1}{m}\nabla U(\tilde{\mathbf{r}}_i)\Delta t$ ;      // apply $\mathcal{L}_T$
    $\mathbf{r}_i(t+\Delta t) \leftarrow \tilde{\mathbf{r}}_i + \frac{1}{2}\mathbf{v}_i(t+\Delta t)\Delta t$ ;       // apply $\mathcal{L}_V$
end
```

Algorithm 3: Simplectic time evolution of test particles.

Calculation of thermal cloud density

```
input  : $N$ test particles at positions $(x_n,y_n,z_n)$
output : Smooth thermal density $\tilde{n}_s(\mathbf{r},t)$
// Calculate histogram using the cloud-in-cell method
for $n<N$ do
    // Calculate lower grid points;
    $k \leftarrow$ floor($(x_n + x_{max})/\Delta x$);
    $l \leftarrow$ floor($(y_n + y_{max})/\Delta y$);
    $m \leftarrow$ floor($(z_n + z_{max})/\Delta z$);
    // Calculate alpha factors;
    $\alpha_x \leftarrow (x_n - x_k)/(x_{k+1} - x_k)$;
    $\alpha_y \leftarrow (y_n - y_l)/(y_{l+1} - y_l)$;
    $\alpha_z \leftarrow (z_n - z_m)/(z_{m+1} - z_m)$;
    // Add weighting factors to corresponding grid point;
    $\tilde{n}_s(x_k,y_l,z_m) \leftarrow \tilde{n}_s(x_k,y_l,z_m) + (1-\alpha_x)(1-\alpha_y)(1-\alpha_z)$;
    $\tilde{n}_s(x_{k+1},y_l,z_m) \leftarrow \tilde{n}_s(x_{k+1},y_l,z_m) + \alpha_x(1-\alpha_y)(1-\alpha_z)$;
    $\tilde{n}_s(x_k,y_{l+1},z_m) \leftarrow \tilde{n}_s(x_k,y_{l+1},z_m) + (1-\alpha_x)\alpha_y(1-\alpha_z)$;
    $\tilde{n}_s(x_k,y_l,z_{m+1}) \leftarrow \tilde{n}_s(x_k,y_l,z_{m+1}) + (1-\alpha_x)(1-\alpha_y)\alpha_z$;
    $\tilde{n}_s(x_{k+1},y_{l+1},z_m) \leftarrow \tilde{n}_s(x_{k+1},y_{l+1},z_m) + \alpha_x\alpha_y(1-\alpha_z)$;
    $\tilde{n}_s(x_{k+1},y_l,z_{m+1}) \leftarrow \tilde{n}_s(x_{k+1},y_l,z_{m+1}) + \alpha_x(1-\alpha_y)\alpha_z$;
    $\tilde{n}_s(x_k,y_{l+1},z_{m+1}) \leftarrow \tilde{n}_s(x_k,y_{l+1},z_{m+1}) + (1-\alpha_x)\alpha_y\alpha_z$;
    $\tilde{n}_s(x_{k+1},y_{l+1},z_{m+1}) \leftarrow \tilde{n}_s(x_{k+1},y_{l+1},z_{m+1}) + \alpha_x\alpha_y\alpha_z$;
end
// Smooth density with the sampling function;
// using the convolution theorem;
$\tilde{n}_s \leftarrow$ FFTW($\tilde{n}_s$)$\cdot\mathcal{F}(S)$;
$\tilde{n}_s \leftarrow$ FFTW$^{-1}$($\tilde{n}_s$);
```

Algorithm 4: Calculation of the thermal density using test particles and the cloud-in-cell method followed by a convolution with the broadening function S.

Bibliography

[1] Feynman, R. P. "There's plenty of room at the bottom". *Engineering and Science* **23**(5), 22–36 (1960).

[2] Toumey, C. "Plenty of room, plenty of history". *Nat. Nanotechnol.* **4**(12), 783–784 (2009).

[3] Dreyfus, R., Baudry, J., Roper, M. L., Fermigier, M., Stone, H. A., and Bibette, J. "Microscopic artificial swimmers". *Nature* **437**(7060), 862–865 (2005).

[4] Howse, J. R., Jones, R. A. L., Ryan, A. J., Gough, T., Vafabakhsh, R., and Golestanian, R. "Self-Motile Colloidal Particles: From Directed Propulsion to Random Walk". *Phys. Rev. Lett.* **99**, 048102 Jul (2007).

[5] Nelson, B. J., Kaliakatsos, I. K., and Abbott, J. J. "Microrobots for Minimally Invasive Medicine". *Annual Review of Biomedical Engineering* **12**(1), 55–85 (2010).

[6] Dujardin, G., Walkup, R. E., and Avouris, P. "Dissociation of Individual Molecules with Electrons from the Tip of a Scanning Tunneling Microscope". *Science* **255**(5049), 1232–1235 (1992).

[7] Mo, Y. W. "Reversible Rotation of Antimony Dimers on the Silicon (001) Surface with a Scanning Tunneling Microscope". *Science* **261**(5123), 886–888 (1993).

[8] Comtet, G., Dujardin, G., Mayne, A. J., and Riedel, D. "Principles of operating molecular nanomachines by electronic excitation". *J. Phys. Condens. Matter* **18**(33), 1927 (2006).

[9] Trevethan, T., Shluger, A., and Kantorovich, L. "Modelling components of future molecular devices". *J. Phys. Condens. Matter* **22**(8), 084024 (2010).

[10] LOTH, S., BAUMANN, S., LUTZ, C. P., EIGLER, D. M., AND HEINRICH, A. J. "Bistability in Atomic-Scale Antiferromagnets". *Science* **335**(6065), 196–199 (2012).

[11] GOULD, R. G. "The LASER, light amplification by stimulated emission of radiation". In *The Ann Arbor conference on optical pumping, the University of Michigan*, volume 15, 128, (1959).

[12] SCHAWLOW, A. L. AND TOWNES, C. H. "Infrared and Optical Masers". *Phys. Rev.* **112**, 1940–1949 (1958).

[13] HECHT, J. *Laser pioneers.* Academic Press New York, (1992).

[14] MAIMAN, T. H. "Stimulated Optical Radiation in Ruby". *Nature* **187**(4736), 493–494 (1960).

[15] WEIDEMÜLLER, M. AND ZIMMERMANN, C. "Cold atoms and molecules". *Laser* **1**, 5 (2009).

[16] COHEN-TANNOUDJI, C. AND MADISON, K. W. *Annual Review of Cold Atoms and Molecules.* World Scientific, (2013).

[17] ASHKIN, A. "Acceleration and Trapping of Particles by Radiation Pressure". *Phys. Rev. Lett.* **24**, 156–159 (1970).

[18] CHU, S., HOLLBERG, L., BJORKHOLM, J. E., CABLE, A., AND ASHKIN, A. "Three-dimensional viscous confinement and cooling of atoms by resonance radiation pressure". *Phys. Rev. Lett.* **55**, 48–51 (1985).

[19] ASPECT, A., DALIBARD, J., HEIDMANN, A., SALOMON, C., AND COHEN-TANNOUDJI, C. "Cooling atoms with stimulated emission". *Phys. Rev. Lett.* **57**(14), 1688–1691 (1986).

[20] FELDMAN, B. *The Nobel Prize: a history of genius, controversy, and prestige.* Arcade Publishing, (2001).

[21] ANDERSON, M. H., ENSHER, J. R., MATTHEWS, M. R., WIEMAN, C. E., AND CORNELL, E. A. "Observation of Bose-Einstein Condensation in a Dilute Atomic Vapor". *Science* **269**(5221), 198–201 (1995).

[22] DAVIS, K. B., MEWES, M. O., ANDREWS, M. R., VAN DRUTEN, N. J., DURFEE, D. S., KURN, D. M., AND KETTERLE, W. "Bose-Einstein Condensation in a Gas of Sodium Atoms". *Phys. Rev. Lett.* **75**, 3969–3973 (1995).

[23] Jaksch, D., Bruder, C., Cirac, J. I., Gardiner, C. W., and Zoller, P. “Cold Bosonic Atoms in Optical Lattices”. *Phys. Rev. Lett.* **81**, 3108–3111 (1998).

[24] Greiner, M., Mandel, O., Esslinger, T., Hänsch, T. W., and Bloch, I. “Quantum phase transition from a superfluid to a Mott insulator in a gas of ultracold atoms”. *Nature* **415**(6867), 39–44 (2002).

[25] Cornell, E., Ketterle, W., and Wiemann, C. “The Nobel Prizes 2001”. *Nobel Foundation* (2002).

[26] Haroche, S. “Nobel Lecture: Controlling photons in a box and exploring the quantum to classical boundary”. *Rev. Mod. Phys.* **85**, 1083–1102 (2013).

[27] Wineland, D. J. “Nobel Lecture: Superposition, entanglement, and raising Schrödinger’s cat”. *Rev. Mod. Phys.* **85**, 1103–1114 (2013).

[28] Georgescu, I. “Nobel Prize 2012: Haroche & Wineland”. *Nature Physics* **8**(11), 777– (2012).

[29] Feynman, R. P. “Simulating physics with computers”. *Int. J. Theor. Phys.* **21**(6), 467–488 (1982).

[30] DiVincenzo, D. P. “The Physical Implementation of Quantum Computation”. *Fortschr. Phys.* **48**(9-11), 771–783 (2000).

[31] Schmidt-Kaler, F., Haffner, H., Riebe, M., Gulde, S., Lancaster, G. P. T., Deuschle, T., Becher, C., Roos, C. F., Eschner, J., and Blatt, R. “Realization of the Cirac-Zoller controlled-NOT quantum gate”. *Nature* **422**(6930), 408–411 (2003).

[32] Blatt, R. and Wineland, D. “Entangled states of trapped atomic ions”. *Nature* **453**(7198), 1008–1015 (2008).

[33] Blatt, R. and Roos, C. “Quantum simulations with trapped ions”. *Nat. Phys.* **8**(4), 277–284 (2012).

[34] Wallraff, A., Schuster, D. I., Blais, A., Frunzio, L., Huang, R.-S., Majer, J., Kumar, S., Girvin, S. M., and Schoelkopf, R. J. “Strong coupling of a single photon to a superconducting qubit using circuit quantum electrodynamics”. *Nature* **431**(7005), 162–167 (2004).

[35] MAJER, J., CHOW, J. M., GAMBETTA, J. M., KOCH, J., JOHNSON, B. R., SCHREIER, J. A., FRUNZIO, L., SCHUSTER, D. I., HOUCK, A. A., WALLRAFF, A., BLAIS, A., DEVORET, M. H., GIRVIN, S. M., AND SCHOELKOPF, R. J. "Coupling superconducting qubits via a cavity bus". *Nature* **449**(7161), 443–447 (2007).

[36] DICARLO, L., REED, M. D., SUN, L., JOHNSON, B. R., CHOW, J. M., GAMBETTA, J. M., FRUNZIO, L., GIRVIN, S. M., DEVORET, M. H., AND SCHOELKOPF, R. J. "Preparation and measurement of three-qubit entanglement in a superconducting circuit". *Nature* **467**(7315), 574–578 (2010).

[37] DICARLO, L., CHOW, J. M., GAMBETTA, J. M., BISHOP, L. S., JOHNSON, B. R., SCHUSTER, D. I., MAJER, J., BLAIS, A., FRUNZIO, L., GIRVIN, S. M., AND SCHOELKOPF, R. J. "Demonstration of two-qubit algorithms with a superconducting quantum processor". *Nature* **460**(7252), 240–244 (2009).

[38] HATTERMANN, H. *Interfacing cold atoms and superconductors.* PhD thesis, Eberhard Karls Universität Tübingen, (2013).

[39] PAIK, H., SCHUSTER, D. I., BISHOP, L. S., KIRCHMAIR, G., CATELANI, G., SEARS, A. P., JOHNSON, B. R., REAGOR, M. J., FRUNZIO, L., GLAZMAN, L. I., GIRVIN, S. M., DEVORET, M. H., AND SCHOELKOPF, R. J. "Observation of High Coherence in Josephson Junction Qubits Measured in a Three-Dimensional Circuit QED Architecture". *Phys. Rev. Lett.* **107**, 240501 (2011).

[40] DEUTSCH, C., RAMIREZ-MARTINEZ, F., LACROÛTE, C., REINHARD, F., SCHNEIDER, T., FUCHS, J. N., PIÉCHON, F., LALOË, F., REICHEL, J., AND ROSENBUSCH, P. "Spin Self-Rephasing and Very Long Coherence Times in a Trapped Atomic Ensemble". *Phys. Rev. Lett.* **105**, 020401 (2010).

[41] WALLQUIST, M., HAMMERER, K., RABL, P., LUKIN, M., AND ZOLLER, P. "Hybrid quantum devices and quantum engineering". *Physica Scripta* **2009**(T137), 014001 (2009).

[42] HUNGER, D., CAMERER, S., HÄNSCH, T. W., KÖNIG, D., KOTTHAUS, J. P., REICHEL, J., AND TREUTLEIN, P. "Resonant Coupling of a Bose-Einstein Condensate to a Micromechanical Oscillator". *Phys. Rev. Lett.* **104**, 143002 (2010).

[43] Bernon, S., Hattermann, H., Bothner, D., Knufinke, M., Weiss, P., Jessen, F., Cano, D., Kemmler, M., Kleiner, R., Koelle, D., and Fortágh, J. "Manipulation and coherence of ultra-cold atoms on a superconducting atom chip". *Nat. Commun.* **4** (2013).

[44] Xiang, Z.-L., Ashhab, S., You, J. Q., and Nori, F. "Hybrid quantum circuits: Superconducting circuits interacting with other quantum systems". *Rev. Mod. Phys.* **85**, 623–653 (2013).

[45] Wang, Y.-J., Eardley, M., Knappe, S., Moreland, J., Hollberg, L., and Kitching, J. "Magnetic Resonance in an Atomic Vapor Excited by a Mechanical Resonator". *Phys. Rev. Lett.* **97**, 227602 (2006).

[46] Bender, H., Courteille, P. W., Marzok, C., Zimmermann, C., and Slama, S. "Direct Measurement of Intermediate-Range Casimir-Polder Potentials". *Phys. Rev. Lett.* **104**, 083201 (2010).

[47] Schneeweiss, P., Gierling, M., Visanescu, G., Kern, D., Judd, T., Günther, A., and Fortágh, J. "Dispersion forces between ultracold atoms and a carbon nanotube". *Nat. Nanotechnol.* **7**(8), 515–519 (2012).

[48] Onofrio, R. "Casimir forces and non-Newtonian gravitation". *New J. Phys.* **8**(10), 237 (2006).

[49] Marchant, A. L., Händel, S., Wiles, T. P., Hopkins, S. A., and Cornish, S. L. "Guided transport of ultracold gases of rubidium up to a room-temperature dielectric surface". *New J. Phys.* **13**(12), 125003 (2011).

[50] Masuda, M. and Sasaki, M. "Limits on Nonstandard Forces in the Submicrometer Range". *Phys. Rev. Lett.* **102**, 171101 (2009).

[51] Treutlein, P., Hunger, D., Camerer, S., Hänsch, T. W., and Reichel, J. "Bose-Einstein Condensate Coupled to a Nanomechanical Resonator on an Atom Chip". *Phys. Rev. Lett.* **99**, 140403 (2007).

[52] Wheeler, J. A. "How Come the Quantum?". *Ann. N.Y. Acad. Sci.* **480**(1), 304–316 (1986).

[53] Cetina, M., Grier, A., Campbell, J., Chuang, I., and Vuletić, V. "Bright source of cold ions for surface-electrode traps". *Phys. Rev. A* **76**, 041401 (2007).

[54] GRIER, A. T., CETINA, M., ORUČEVIĆ, F., AND VULETIĆ, V. "Observation of Cold Collisions between Trapped Ions and Trapped Atoms". *Phys. Rev. Lett.* **102**, 223201 (2009).

[55] ZIPKES, C., PALZER, S., SIAS, C., AND KÖHL, M. "A trapped single ion inside a Bose-Einstein condensate". *Nature* **464**(7287), 388–391 (2010).

[56] HÄRTER, A. *Two-Body and Three-Body Dynamics in Atom-Ion Experiments.* PhD thesis, Universität Ulm, (2013).

[57] DEVREESE, J. T. AND ALEXANDROV, A. S. "Fröhlich polaron and bipolaron: recent developments". *Rep. Prog. Phys.* **72**(6), 066501 (2009).

[58] FORTÁGH, J., GROSSMANN, A., ZIMMERMANN, C., AND HÄNSCH, T. W. "Miniaturized Wire Trap for Neutral Atoms". *Phys. Rev. Lett.* **81**, 5310–5313 (1998).

[59] FOLMAN, R., KRÜGER, P., CASSETTARI, D., HESSMO, B., MAIER, T., AND SCHMIEDMAYER, J. "Controlling Cold Atoms using Nanofabricated Surfaces: Atom Chips". *Phys. Rev. Lett.* **84**, 4749–4752 (2000).

[60] OTT, H., FORTÁGH, J., SCHLOTTERBECK, G., GROSSMANN, A., AND ZIMMERMANN, C. "Bose-Einstein Condensation in a Surface Microtrap". *Phys. Rev. Lett.* **87**(23), 230401 (2001).

[61] DENSCHLAG, J., CASSETTARI, D., AND SCHMIEDMAYER, J. "Guiding Neutral Atoms with a Wire". *Phys. Rev. Lett.* **82**, 2014–2017 (1999).

[62] HANSEL, W., HOMMELHOFF, P., HÄNSCH, T. W., AND REICHEL, J. "Bose-Einstein condensation on a microelectronic chip". *Nature* **413**(6855), 498–501 (2001).

[63] FORTÁGH, J. AND ZIMMERMANN, C. "Magnetic microtraps for ultracold atoms". *Rev. Mod. Phys.* **79**(1), 235–289 (2007).

[64] PROUKAKIS, N. P. AND JACKSON, B. "Finite-temperature models of Bose–Einstein condensation". *J. Phys. B: At. Mol. Opt. Phys.* **41**(20), 203002 (2008).

[65] DAVIS, M. J., MORGAN, S. A., AND BURNETT, K. "Simulations of Bose Fields at Finite Temperature". *Phys. Rev. Lett.* **87**, 160402 (2001).

[66] Blakie, P. B. and Davis, M. J. “Projected Gross-Pitaevskii equation for harmonically confined Bose gases at finite temperature”. *Phys. Rev. A* **72**(6), 063608– (2005).

[67] Blakie, P., Bradley, A., Davis, M., Ballagh, R., and Gardiner, C. “Dynamics and statistical mechanics of ultra-cold Bose gases using c-field techniques”. *Adv. Phys.* **57**(5), 363–455 (2008).

[68] Blakie, P. B., Bradley, A. S., Davis, M. J., Ballagh, R. J., and Gardiner, C. W. “Dynamics and statistical mechanics of ultra-cold Bose gases using c-field techniques”. *Adv. Phys.* **57**, 363 (2008).

[69] Stoof, H. “Initial Stages of Bose-Einstein Condensation”. *Phys. Rev. Lett.* **78**, 768–771 (1997).

[70] Stoof, H. “Coherent Versus Incoherent Dynamics During Bose-Einstein Condensation in Atomic Gases”. *J. Low Temp. Phys.* **114**(1-2), 11–108 (1999).

[71] Gardiner, C. W. and Davis, M. J. “The stochastic Gross–Pitaevskii equation: II”. *J. Phys. B: At. Mol. Opt. Phys.* **36**(23), 4731 (2003).

[72] Kirkpatrick, T. and Dorfman, J. “Transport in a dilute but condensed nonideal Bose gas: Kinetic equations”. *J. Low Temp. Phys.* **58**(3-4), 301–331 (1985).

[73] Nikuni, T., Zaremba, E., and Griffin, A. “Two-Fluid Dynamics for a Bose-Einstein Condensate out of Local Equilibrium with the Noncondensate”. *Phys. Rev. Lett.* **83**, 10–13 (1999).

[74] Zaremba, E., Nikuni, T., and Griffin, A. “Dynamics of Trapped Bose Gases at Finite Temperatures”. *J. Low Temp. Phys.* **116**(3-4), 277–345 (1999).

[75] Jackson, B. and Zaremba, E. “Modeling Bose-Einstein condensed gases at finite temperatures with N-body simulations”. *Phys. Rev. A* **66**(3), 033606 (2002).

[76] Pitaevskii, L. P. and Stringari, S. *Bose-einstein condensation.* Number 116. Oxford University Press, (2003).

[77] Pethick, C. J. and Smith, H. *Bose-Einstein condensation in dilute gases.* Cambridge university press, (2002).

[78] ANNETT, J. F. *Superconductivity, Superfluids and Condensates.* Oxford University Press, (2004).

[79] ZAREMBA, E., NIKUNI, T., AND GRIFFIN, A. *Bose-Condensed Gases at Finite Temperatures.* Cambridge University Press, (2009).

[80] SCHWABL, F. *Statistische Mechanik*, volume 3. Springer, (2006).

[81] BOGOLIOUBOV, N. N. "On the theory of superfluidity". *J.Phys. USSR* **11**, 23 (1947).

[82] PITAEVSKII, L. P. "Vortex lines in an imperfect Bose Gas". *Soviet Physics JETP-USSR* **13**(2) (1961).

[83] GROSS, E. "Structure of a quantized vortex in boson systems". *Il Nuovo Cimento Series 10* **20**(3), 454–477 (1961).

[84] DALFOVO, F., GIORGINI, S., PITAEVSKII, L. P., AND STRINGARI, S. "Theory of Bose-Einstein condensation in trapped gases". *Rev. Mod. Phys.* **71**, 463–512 (1999).

[85] ANDREWS, M. R., KURN, D. M., MIESNER, H.-J., DURFEE, D. S., TOWNSEND, C. G., INOUYE, S., AND KETTERLE, W. "Propagation of Sound in a Bose-Einstein Condensate". *Phys. Rev. Lett.* **79**, 553–556 (1997).

[86] STRINGARI, S. "Collective Excitations of a Trapped Bose-Condensed Gas". *Phys. Rev. Lett.* **77**, 2360–2363 (1996).

[87] SAPINA, I., DAHM, T., AND SCHOPOHL, N. "Ground-state and collective modes of a spin-polarized dipolar Bose-Einstein condensate in a harmonic trap". *Phys. Rev. A* **82**, 053620 (2010).

[88] EDWARDS, M., RUPRECHT, P. A., BURNETT, K., DODD, R. J., AND CLARK, C. W. "Collective Excitations of Atomic Bose-Einstein Condensates". *Phys. Rev. Lett.* **77**, 1671–1674 (1996).

[89] PROUKAKIS, N. P., BURNETT, K., AND STOOF, H. T. C. "Microscopic treatment of binary interactions in the nonequilibrium dynamics of partially Bose-condensed trapped gases". *Phys. Rev. A* **57**, 1230–1247 (1998).

[90] WALSER, R., WILLIAMS, J., COOPER, J., AND HOLLAND, M. "Quantum kinetic theory for a condensed bosonic gas". *Phys. Rev. A* **59**, 3878–3889 (1999).

[91] Jackson, B. and Zaremba, E. “Finite-Temperature Simulations of the Scissors Mode in Bose-Einstein Condensed Gases”. *Phys. Rev. Lett.* **87**(10), 100404– (2001).

[92] Jackson, B. and Zaremba, E. “Quadrupole Collective Modes in Trapped Finite-Temperature Bose-Einstein Condensates”. *Phys. Rev. Lett.* **88**, 180402 (2002).

[93] Jackson, B. and Zaremba, E. “Accidental Suppression of Landau Damping of the Transverse Breathing Mode in Elongated Bose-Einstein Condensates”. *Phys. Rev. Lett.* **89**, 150402 (2002).

[94] Jackson, B., Barenghi, C., and Proukakis, N. “Matter Wave Solitons at Finite Temperatures”. *J. Low Temp. Phys.* **148**(3-4), 387–391 (2007).

[95] Jackson, B., Proukakis, N. P., and Barenghi, C. F. “Dark-soliton dynamics in Bose-Einstein condensates at finite temperature”. *Phys. Rev. A* **75**, 051601 (2007).

[96] Jackson, B., Proukakis, N. P., Barenghi, C. F., and Zaremba, E. “Finite-temperature vortex dynamics in Bose-Einstein condensates”. *Phys. Rev. A* **79**(5), 053615 (2009).

[97] Allen, A. J., Zaremba, E., Barenghi, C. F., and Proukakis, N. P. “Observable vortex properties in finite-temperature Bose gases”. *Phys. Rev. A* **87**(1), 013630– (2013).

[98] Allen, A. J. *Non-Equilibrium and Finite Temperature Trapped Bose Gases: Interactions and Decay of Macroscopic Excitations*. PhD thesis, Newcastle University, (2011).

[99] Bird, G. A. “Direct Simulation and the Boltzmann Equation”. *Physics of Fluids* **13**(11), 2676–2681 (1970).

[100] Alexander, F. J. and Garcia, A. L. “The direct simulation Monte Carlo method”. *Computers in Physics* **11**(6), 588 (1997).

[101] Gallis, M., Torczynski, J., Rader, D., and Bird, G. “Convergence behavior of a new DSMC algorithm”. *Journal of Computational Physics* **228**(12), 4532 – 4548 (2009).

[102] Bird, G. A., Gallis, M. A., Torczynski, J. R., and Rader, D. J. “Accuracy and efficiency of the sophisticated direct simulation Monte

Carlo algorithm for simulating noncontinuum gas flows". *Physics of Fluids* **21**(1) (2009).

[103] WADE, A. C. J., BAILLIE, D., AND BLAKIE, P. B. "Direct simulation Monte Carlo method for cold-atom dynamics: Classical Boltzmann equation in the quantum collision regime". *Phys. Rev. A* **84**(2), 023612– (2011).

[104] WILLIAMS, J. E. AND GRIFFIN, A. "Damped Bogoliubov excitations of a condensate interacting with a static thermal cloud". *Phys. Rev. A* **64**, 013606 (2001).

[105] QING-XIN, Y. AND GUO-HUI, D. "Computing Ground State Solution of Bose–Einstein Condensates Trapped in One-Dimensional Harmonic Potential". *Commun. Theor. Phys.* **46**(5), 873 (2006).

[106] CHIOFALO, M. L., SUCCI, S., AND TOSI, M. P. "Ground state of trapped interacting Bose-Einstein condensates by an explicit imaginary-time algorithm". *Phys. Rev. E* **62**, 7438–7444 (2000).

[107] JACKSON, B. ZAREMBA, E. "Dynamical simulation of trapped bose gases". *Laser Phys.* **12**, 93–105 (2002).

[108] LUBICH, C. "On splitting methods for Schrödinger-Poisson and cubic nonlinear Schrödinger equations". *Math. Comput.* **77**(264), 2141–2153 (2008).

[109] GAUCKLER, L. "Convergence of a split-step Hermite method for the Gross–Pitaevskii equation". *IMA Journal of Numerical Analysis* (2010).

[110] FETTER, A. L. AND WALECKA, J. D. *Quantum theory of many-particle systems.* Courier Dover Publications, (2003).

[111] JAHNKE, T. AND LUBICH, C. "Error Bounds for Exponential Operator Splittings". *BIT Numerical Mathematics* **40**(4), 735–744 (2000).

[112] BAO, W., JAKSCH, D., AND MARKOWICH, P. A. "Numerical solution of the Gross–Pitaevskii equation for Bose–Einstein condensation". *J. Comput. Phys.* **187**(1), 318 – 342 (2003).

[113] BESSE, C., BIDÉGARAY, B., AND DESCOMBES, S. "Order Estimates in Time of Splitting Methods for the Nonlinear Schrödinger Equation". *SIAM J. Numer. Anal.* **40**(1), 26–40 (2002).

[114] Campbell, J. “On a law of combination of operators bearing on the theory of continuous transformation groups”. *Proceedings of the London Mathematical Society* **1**(1), 381–390 (1896).

[115] Campbell, J. E. “On a law of combination of operators (second paper)”. *Proceedings of the London Mathematical Society* **1**(1), 14–32 (1897).

[116] Frigo, M. and Johnson, S. G. “The Design and Implementation of FFTW3”. *Proceedings of the IEEE* **93**(2), 216–231 (2005). Special issue on “Program Generation, Optimization, and Platform Adaptation”.

[117] Hockney, R. W. and Eastwood, J. W. *Computer simulation using particles*. CRC Press, (2010).

[118] Sanz-Serna, J. M. “Symplectic integrators for Hamiltonian problems: an overview”. *Acta Numerica* **1**, 243–286 1 (1992).

[119] Sanz-Serna, J.-M. and Calvo, M.-P. *Numerical hamiltonian problems*, volume 7. Chapman & Hall London, (1994).

[120] Yoshida, H. “Recent progress in the theory and application of symplectic integrators”. *Celestial Mechanics and Dynamical Astronomy* **56**(1-2), 27–43 (1993).

[121] Devroye, L. *Sample-based non-uniform random variate generation.* (1986).

[122] Knuth, D. E. *The art of Computer Programming, Volume 2: Seminumerical Algorithms*. Addison-Wesley Professional, (2014).

[123] Press, W. H. *Numerical recipes 3rd edition: The art of scientific computing*. Cambridge university press, (2007).

[124] Von Neumann, J. “Various techniques used in connection with random digits”. *Applied Math Series* **12**(36-38), 1 (1951).

[125] Prasanth, P. and Kakkassery, J. K. “Direct simulation Monte Carlo (DSMC): A numerical method for transition-regime flows-A review”. *J. Indian Inst. Sci.* **86**(3), 169 (2013).

[126] Lang, A., Babovsky, H., Cassing, W., Mosel, U., Reusch, H.-G., and Weber, K. “A new treatment of Boltzmann-like collision integrals in nuclear kinetic equations”. *Journal of Computational Physics* **106**(2), 391 – 396 (1993).

[127] GABRIEL, E., FAGG, G. E., BOSILCA, G., ANGSKUN, T., DONGARRA, J. J., SQUYRES, J. M., SAHAY, V., KAMBADUR, P., BARRETT, B., LUMSDAINE, A., CASTAIN, R. H., DANIEL, D. J., GRAHAM, R. L., AND WOODALL, T. S. "Open MPI: Goals, Concept, and Design of a Next Generation MPI Implementation". In *Proceedings, 11th European PVM/MPI Users' Group Meeting*, 97–104 (, Budapest, Hungary, 2004).

[128] KJOLSTAD, F. B. AND SNIR, M. "Ghost Cell Pattern". In *Proceedings of the 2010 Workshop on Parallel Programming Patterns*, ParaPLoP '10, 4:1–4:9 (ACM, New York, NY, USA, 2010).

[129] KETTERLE, W. AND DRUTEN, N. V. "Evaporative Cooling of Trapped Atoms". In *Advances In Atomic, Molecular, and Optical Physics,* Bederson, B. and Walther, H., editors, volume 37, 181 – 236. Academic Press (1996).

[130] FORTÁGH, J., OTT, H., KRAFT, S., GÜNTHER, A., AND ZIMMERMANN, C. "Surface effects in magnetic microtraps". *Phys. Rev. A* **66**, 041604 (2002).

[131] CANO, D., KASCH, B., HATTERMANN, H., KOELLE, D., KLEINER, R., ZIMMERMANN, C., AND FORTÁGH, J. "Impact of the Meissner effect on magnetic microtraps for neutral atoms near superconducting thin films". *Phys. Rev. A* **77**, 063408 (2008).

[132] REICHEL, J., HÄNSEL, W., AND HÄNSCH, T. W. "Atomic Micromanipulation with Magnetic Surface Traps". *Phys. Rev. Lett.* **83**, 3398–3401 (1999).

[133] GIERLING, M., SCHNEEWEISS, P., VISANESCU, G., FEDERSEL, P., HÄFFNER, M., KERN, D. P., JUDD, T. E., GÜNTHER, A., AND FORTÁGH, J. "Cold-atom scanning probe microscopy". *Nat. Nanotechnol.* **6**(7), 446–451 (2011).

[134] HARBER, D., MCGUIRK, J., OBRECHT, J., AND CORNELL, E. "Thermally Induced Losses in Ultra-Cold Atoms Magnetically Trapped Near Room-Temperature Surfaces". *J. Low Temp. Phys.* **133**(3-4), 229–238– (2003).

[135] MIN, K., BO, Y., FENG, C., AND YU-ZHU, W. "Surface-induced evaporative cooling". *Chin. Phys. B* **18**(10), 4274 (2009).

[136] BIJLSMA, M. J., ZAREMBA, E., AND STOOF, H. T. C. "Condensate growth in trapped Bose gases". *Phys. Rev. A* **62**(6), 063609 (2000).

[137] Luiten, O. J., Reynolds, M. W., and Walraven, J. T. M. "Kinetic theory of the evaporative cooling of a trapped gas". *Phys. Rev. A* **53**, 381–389 (1996).

[138] Wu, H. and Foot, C. J. "Direct simulation of evaporative cooling". *J. Phys. B: At. Mol. Opt. Phys.* **29**(8), L321 (1996).

[139] Holland, M., Williams, J., and Cooper, J. "Bose-Einstein condensation: Kinetic evolution obtained from simulated trajectories". *Phys. Rev. A* **55**, 3670–3677 (1997).

[140] Davis, M. J., Gardiner, C. W., and Ballagh, R. J. "Quantum kinetic theory. VII. The influence of vapor dynamics on condensate growth". *Phys. Rev. A* **62**, 063608 (2000).

[141] Davis, M. J. and Gardiner, C. W. "Growth of a Bose–Einstein condensate: A detailed comparison of theory and experiment". *J. Phys. B: At. Mol. Opt.* **35**, 733 (2002).

[142] Hugbart, M., Retter, J. A., Varón, A. F., Bouyer, P., Aspect, A., and Davis, M. J. "Population and phase coherence during the growth of an elongated Bose–Einstein condensate". *Phys. Rev. A* **75**, 011602 (2007).

[143] Stoof, H. T. C. and Bijlsma, M. J. "Dynamics of Fluctuating Bose–Einstein Condensates". *J. Low Temp. Phys.* **124**, 431 (2001).

[144] Duine, R. A. and Stoof, H. T. C. "Stochastic dynamics of a trapped Bose-Einstein condensate". *Phys. Rev. A* **65**, 013603 (2001).

[145] Proukakis, N. P., Schmiedmayer, J., and Stoof, H. T. C. "Quasicondensate growth on an atom chip". *Phys. Rev. A* **73**, 053603 (2006).

[146] Weiler, C. N., Neely, T. W., Scherer, D. R., Bradley, A. S., Davis, M. J., and Anderson, B. P. "Spontaneous vortices in the formation of Bose–Einstein condensates". *Nature* **455**, 948 (2008).

[147] Damski, B. and Zurek, W. H. "Soliton Creation During a Bose–Einstein Condensation". *Phys. Rev. Lett.* **104**, 160404 (2010).

[148] Garrett, M. C., Ratnapala, A., van Ooijen, E. D., Vale, C. J., Weegink, K., Schnelle, S. K., Vainio, O., Heckenberg, N. R., Rubinsztein-Dunlop, H., and Davis, M. J. "Growth dynamics of

a Bose-Einstein condensate in a dimple trap without cooling". *Phys. Rev. A* **83**, 013630 (2011).

[149] MÄRKLE, J., ALLEN, A. J., FEDERSEL, P., JETTER, B., GÜNTHER, A., FORTÁGH, J., PROUKAKIS, N. P., AND JUDD, T. E. "Evaporative cooling of cold atoms at surfaces". *Phys. Rev. A* **90**, 023614 Aug (2014).

[150] CASIMIR, H. B. G. AND POLDER, D. "The Influence of Retardation on the London-van der Waals Forces". *Phys. Rev.* **73**(4), 360–372 (1948).

[151] SHIMIZU, F. "Specular Reflection of Very Slow Metastable Neon Atoms from a Solid Surface". *Phys. Rev. Lett.* **86**, 987–990 (2001).

[152] YAN, Z.-C., DALGARNO, A., AND BABB, J. F. "Long-range interactions of lithium atoms". *Phys. Rev. A* **55**, 2882–2887 (1997).

[153] LIN, Y.-J., TEPER, I., CHIN, C., AND VULETIĆ, V. "Impact of the Casimir-Polder Potential and Johnson Noise on Bose-Einstein Condensate Stability Near Surfaces". *Phys. Rev. Lett.* **92**, 050404 (2004).

[154] PARTRIDGE, G. B., LI, W., LIAO, Y.-A., AND HULET, R. G. "Phases of a fermi gas with unequal spin populations". In *Quantum Electronics and Laser Science Conference, 2007. QELS'07*, 1–2. IEEE, (2007).

[155] BERGQUIST, J. C., WINELAND, D. J., ITANO, W. M., HEMMATI, H., DANIEL, H. U., AND LEUCHS, G. "Energy and Radiative Lifetime of the $5d^9 6s^2\ {}^2D_{\frac{5}{2}}$ State in Hg II by Doppler-Free Two-Photon Laser Spectroscopy". *Phys. Rev. Lett.* **55**, 1567–1570 (1985).

[156] BERGQUIST, J. C., ITANO, W. M., AND WINELAND, D. J. "Recoilless optical absorption and Doppler sidebands of a single trapped ion". *Phys. Rev. A* **36**, 428–430 (1987).

[157] DIEDRICH, F., BERGQUIST, J. C., ITANO, W. M., AND WINELAND, D. J. "Laser Cooling to the Zero-Point Energy of Motion". *Phys. Rev. Lett.* **62**, 403–406 (1989).

[158] CIRAC, J. I. AND ZOLLER, P. "Quantum Computations with Cold Trapped Ions". *Phys. Rev. Lett.* **74**, 4091–4094 (1995).

[159] NIELSEN, M. A. AND CHUANG, I. L. *Quantum computation and quantum information.* Cambridge university press, (2010).

[160] CÔTÉ, R. "From Classical Mobility to Hopping Conductivity: Charge Hopping in an Ultracold Gas". *Phys. Rev. Lett.* **85**, 5316–5319 (2000).

[161] Côté, R., Kharchenko, V., and Lukin, M. D. "Mesoscopic Molecular Ions in Bose-Einstein Condensates". *Phys. Rev. Lett.* **89**, 093001 (2002).

[162] Alexandrov, A. S. and Devreese, J. T. *Advances in Polaron Physics*, volume 159. Springer, (2009).

[163] Cucchietti, F. M. and Timmermans, E. "Strong-Coupling Polarons in Dilute Gas Bose-Einstein Condensates". *Phys. Rev. Lett.* **96**, 210401 (2006).

[164] Casteels, W., Tempere, J., and Devreese, J. T. "Polaronic properties of an impurity in a Bose-Einstein condensate in reduced dimensions". *Phys. Rev. A* **86**, 043614 (2012).

[165] Smith, D. "The ion chemistry of interstellar clouds". *Chem. Rev.* **92**(7), 1473–1485 (1992).

[166] Gerlich, D. and Horning, S. "Experimental investigation of radiative association processes as related to interstellar chemistry". *Chem. Rev.* **92**(7), 1509–1539 (1992).

[167] Jackson, J. D. "Classical Electrodynamics, 3rd Edition". **1** (1998).

[168] Côté, R. and Dalgarno, A. "Ultracold atom-ion collisions". *Phys. Rev. A* **62**, 012709 (2000).

[169] Sakurai, J. J. *Modern Quantum Mechanics (Revised Edition)*. Addison Wesley, 1 edition, September (1993).

[170] Zipkes, C., Ratschbacher, L., Sias, C., and Köhl, M. "Kinetics of a single trapped ion in an ultracold buffer gas". *New J. Phys.* **13**(5), 053020 (2011).

[171] Massey, H. S. W. and Mohr, C. B. O. "Free Paths and Transport Phenomena in Gases and the Quantum Theory of Collisions. II. The Determination of the Laws of Force between Atoms and Molecules". *Proc. R. Soc. London, Ser. A* **144**(851), 188–205 (1934).

[172] McDowell, M. R. C. "Elastic Scattering of Slow Ions in their Parent Gases". *Proc. Phys. Soc. London* **72**(6), 1087 (1958).

[173] Earnshaw, S. "On the nature of the molecular forces which regulate the constitution of the luminiferous ether". *Trans. Camb. Phil. Soc.* **7**, 97–112 (1842).

[174] LEIBFRIED, D., BLATT, R., MONROE, C., AND WINELAND, D. "Quantum dynamics of single trapped ions". *Rev. Mod. Phys.* **75**, 281–324 (2003).

[175] GHOSH, P. K. *Ion traps.* Clarendon press Oxford, (1995).

[176] DEHMELT, H. ET AL. "Radiofrequency spectroscopy of stored ions I: Storage". *Adv. At. Mol. Phys* **3**, 53 (1967).

[177] LANDAU, L. AND LIFSHITZ, E. *Statistical Physics: Course of Theoretical Physics.* Pergamon Press, (1958).

[178] KIPPENBERG, T. J. AND VAHALA, K. J. "Cavity Optomechanics: Back-Action at the Mesoscale". *Science* **321**(5893), 1172–1176 (2008).

[179] ARCIZET, O., COHADON, P.-F., BRIANT, T., PINARD, M., AND HEIDMANN, A. "Radiation-pressure cooling and optomechanical instability of a micromirror". *Nature* **444**(7115), 71–74 (2006).

[180] BARTON, R. A., STORCH, I. R., ADIGA, V. P., SAKAKIBARA, R., CIPRIANY, B. R., ILIC, B., WANG, S. P., ONG, P., MCEUEN, P. L., PARPIA, J. M., AND CRAIGHEAD, H. G. "Photothermal Self-Oscillation and Laser Cooling of Graphene Optomechanical Systems". *Nano Lett.* **12**(9), 4681–4686 (2012).

[181] FAVERO, I. AND KARRAI, K. "Optomechanics of deformable optical cavities". *Nat. Photonics* **3**(4), 201–205 (2009).

[182] CAMERER, S., KORPPI, M., JÖCKEL, A., HUNGER, D., HÄNSCH, T. W., AND TREUTLEIN, P. "Realization of an Optomechanical Interface Between Ultracold Atoms and a Membrane". *Phys. Rev. Lett.* **107**, 223001 (2011).

[183] DARÁZS, Z., KURUCZ, Z., KÁLMÁN, O., KISS, T., FORTÁGH, J., AND DOMOKOS, P. "Parametric Amplification of the Mechanical Vibrations of a Suspended Nanowire by Magnetic Coupling to a Bose-Einstein Condensate". *Phys. Rev. Lett.* **112**, 133603 (2014).

[184] TIAN, L. AND ZOLLER, P. "Coupled Ion-Nanomechanical Systems". *Phys. Rev. Lett.* **93**, 266403 (2004).

[185] WEILER, C. N., NEELY, T. W., SCHERER, D. R., BRADLEY, A. S., DAVIS, M. J., AND ANDERSON, B. P. "Spontaneous vortices in the formation of Bose–Einstein condensates". *Nature* **455**(7215), 948–951 (2008).

[186] Jetter, B., Märkle, J., Schneeweiss, P., Gierling, M., Scheel, S., Günther, A., Fortágh, J., and Judd, T. "Scattering and absorption of ultracold atoms by nanotubes". *New J. Phys.* **15**(7), 073009 (2013).

[187] Penrose, O. and Onsager, L. "Bose-Einstein Condensation and Liquid Helium". *Phys. Rev.* **104**, 576–584 (1956).

[188] Krishnan, A., Dujardin, E., Ebbesen, T. W., Yianilos, P. N., and Treacy, M. M. J. "Young's modulus of single-walled nanotubes". *Phys. Rev. B* **58**, 14013–14019 (1998).

[189] Stuhler, J., Griesmaier, A., Koch, T., Fattori, M., Pfau, T., Giovanazzi, S., Pedri, P., and Santos, L. "Observation of Dipole-Dipole Interaction in a Degenerate Quantum Gas". *Phys. Rev. Lett.* **95**, 150406 (2005).

[190] Kühn, S. and Judd, T. E. "Transport of dipolar Bose-Einstein condensates in a one-dimensional optical lattice". *Phys. Rev. A* **87**, 023608 (2013).

[191] Blakie, P. B., Baillie, D., and Bisset, R. N. "Depletion and fluctuations of a trapped dipolar Bose-Einstein condensate in the roton regime". *Phys. Rev. A* **88**, 013638 (2013).

[192] Lahaye, T., Menotti, C., Santos, L., Lewenstein, M., and Pfau, T. "The physics of dipolar bosonic quantum gases". *Rep. Prog. Phys.* **72**(12), 126401 (2009).

[193] Chen, H., Kandasamy, S., Orszag, S., Shock, R., Succi, S., and Yakhot, V. "Extended Boltzmann Kinetic Equation for Turbulent Flows". *Science* **301**(5633), 633–636 (2003).

[194] Feynman, R. P., Leighton, R. B., and Sands, M. *The Feynman Lectures on Physics, Desktop Edition Volume I*, volume 1. Basic Books, (2013).

[195] Von Neumann, J. and Taub, A. *Collected Works. Vol. 5: Design of Computers, Theory of Automata and Numerical Analysis.* Oxford, (1963).

Acknowledgements

The success of any project depends largely on the encouragement and guidelines of many. I take this opportunity to express my gratitude to the people who have been involved in the successful completion of this project.

First and foremost I would like to gratefully acknowledge the enthusiastic supervision of Prof. Thomas E. Judd. He has been very supportive, patient and motivating especially in hard times during my thesis. He has always been open minded for new ideas and his guidance largely contributed to the success of my work. It has been a great honor to be one of his first PhD students.

I would like to thank the Carl Zeiss Stiftung for granting me a scholarship. Without it my research would not have been possible in the first place and I am very thankful for the given opportunity.

I shared my course of studies, my diploma and the office during my thesis with Benjamin Jetter and I am very grateful that he accompanied me for such a long time. There is no person I have seen more often in the last eight years and I thank him for enduring me in the nerve-wracking times of oral and written exams as well as diploma and thesis writing. His humorous and cheerful manner enlightened my life inside and outside the world of physics.

I am very grateful for the help and support of Joy Allen with the ZNG method. It has been a great relief to talk about details of the method and to share the struggle with collision integrals and unstable simulations. I want to thank her for patiently answering tons of questions via email and discussions. My thanks also goes to her former supervisor Prof. Nikolaos Proukakis, not only for his superb tutorial on finite temperatures, but also for ideas and discussions, which positively affected my work.

Many thanks go to my second supervisor Prof. Claus Zimmermann for fruitful discussions about physics, science and the world in general. These discussions as well as his lectures about the interactions between atoms and light, which introduced me to the field of quantum optics, have been very inspiring.

I also like to thank Prof. József Fortágh who supervises the experimental group for nano atom optics in Tübingen, which provided experimental data for the numerical simulations. He supported my work with innovative ideas in numerous seminars and group meetings. In addition I thank him for his consultation prior to my diploma, in which he motivated me to work in the field of quantum optics.

Special thanks go to Andreas Günther and Peter Federsel who performed surface evaporation measurements, that were presented in this work. With a great effort they helped to analyze and interpret the measured data and were able to give precise information about the experimental details.

Another experimental group, which contributed to the success of this work, is the group of Prof. Johannes Hecker-Denschlag in Ulm. Together with his highly motivated PhD students Arne Härter and Artjom Krükow, he inspired the simulations of the atom-ion system and did not hesitate to help with experimental data and theoretical advice on the hybrid system.

The support, entertainment, understanding and encouragement provided by Marleen Blazer is invaluable. I thank her for always standing by my side, especially during the hard times of my thesis.

As much as I learned about physics during my thesis, I learned about life from my son Finn Willem Blazer, who cheered me up and enriched my after-work life every day.

I am very grateful for the unconditional moral and financial support of Gisela and Christoph Schmid. They not only gave me the opportunity to focus on my studies, but they, both being natural scientists themselves, have also had a strong impact on the way I think about physical problems. They therefore substantially contributed to this work. In addition I would like to thank my brothers Philip and Daniel Märkle, whose company I always enjoyed.

I like to thank the whole 5th floor of the Physikalisches Institut Tübingen for the coffee breaks, lunches, seminars and cakes, which created a very pleasant work atmosphere. It has been a pleasure.

Last but not least there are many people, who I came to know during my studies, my diploma and my thesis, whose company I value and who I will miss: Alexander Rembold, Helge Hattermann, Reinhardt Maier, Alexander Schilke, Katharina Lauber, Michael Jag, Amadeus Belschner, Isabel Gonzalez, Stefan Warnke, Max Kahmann, Igor Sapina, Mario Schröck, Patrizia Weiß, Tina Oexl, Sebastian Schleehauf.

Erklärung

Ich erkläre hiermit, dass ich die zur Promotion eingereichte Arbeit mit dem Titel “Hybrid systems at finite temperatures” selbständig verfasst, nur die angegebenen Quellen und Hilfsmittel benutzt und wörtlich oder inhaltlich übernommene Stellen als solche gekennzeichnet habe. Ich versichere an Eides statt, dass diese Angaben wahr sind und dass ich nichts verschwiegen habe. Mir ist bekannt, dass die falsche Abgabe einer Versicherung an Eides statt mit Freiheitsstrafe bis zu drei Jahren oder mit Geldstrafe bestraft wird

Tübingen, December 17, 2014

Johannes Märkle